REDESIGN AND MANUFACTURABILITY ASSESSMENT OF A TELESCOPIC SHOCK ABSORBER SYSTEM TO ENHANCE PERFORMANCE ON UNEVEN POTHOLED ROADS

BY

MULAMUZI ISAAC

(B. Eng. Automotive & Power Eng., Kyu)

23/U/GMEM/0927/PE

A DISSERTATION SUBMITTED TO THE DIRECTORATE OF RESEARCH AND GRADUATE TRAINING IN PARTIAL FULFILLMENT OF THE REQUIREMENTS FOR THE AWARD OF THE DEGREE OF MASTER OF SCIENCE IN ADVANCED MANUFACTURING SYSTEMS ENGINEERING OF KYAMBOGO UNIVERSITY

NOVEMBER, 2025

DECLARATION

I, **Mulamuzi Isaac**, declare that the contents of this dissertation are my original work and have not been used in any other university for any academic award, or any other related reasons.

Sign. ..... Date. .....

APPROVAL

This is to approve that the work included in this dissertation was solely written by Mr. Mulamuzi Isaac, a Master's student and was authentically carried out under our supervision.

Sign. .....Date. .....

Main Supervisor: Eng. Dr. Samuel Kangwagye, Ph.D.

Sign. .....Date. .....

Co-Supervisor: Dr. Kizito Mubiru

DEDICATION

To my wife and children, Dylan and Isabella, who have patiently endured my absence throughout this period of study.

ACKNOWLEDGEMENTS

I would like to express my heartfelt gratitude to the 2023 GMEM intake class for their unwavering support throughout the project. A special thank you goes to my supervisors, Eng. Dr. Samuel Kangwagye and Dr. Kizito Paul Mubiru, for their invaluable guidance, time, and assistance in resolving my doubts and challenging us to exceed our limits. I would also like to extend my deepest appreciation to Mr. Kasaija Charles for his exceptional support with the simulation programs.

TABLE OF CONTENTS

LIST OF TABLES

LIST OF FIGURES

LIST OF SYMBOLS AND ABBREVIATIONS

A	Orifice cross-sectional area
A	Cross-sectional area
B	Fluid Bulk modulus
D	Diameter
F	Frequency
F	Force
G	Gravitational constant acceleration
k_s	Suspension spring stiffness
k_t	Vertical tire spring stiffness
K	Polytropic coefficient
L	Length
M	Mass
m_s	Sprung mass
m_u	Unsprung mass
μ	Dynamic viscosity
P	Pressure
Q	Volumetric flow rate
P	Density
S	Stroke
T	Time
Y	Flow velocity
V	Volume
X	Displacement
Δ	Wheel displacement
C	Spring index
L_f	Free length of the spring
L_s	Solid length of the spring
T	Compression travel
τ_t	Torsion shear stress

τ_d	Direct shear stress
T	Resultant shear stress
K_w	Wahl's correction factor
FoS	Factor of Safety
Λ	Slenderness ratio
$P_{gas,i}$	Initial nitrogen gas pressure
A_p	Piston area
A_r	Rod cross-sectional area
A_e	Effective area
V_i	Total internal volume
$L_{gas,i}$	Initial gas chamber height

ABBREVIATIONS

CAD	Computer-Aided Design
FEA	Finite Element Analysis
DoF	Degrees of Freedom
CFRP	Carbon Fiber-Reinforced Polymer
EMSA	Electromagnetic Shock Absorber
SAE	Society of Automotive Engineers
EUSAMA	European Shock Absorber Manufacturers' Association
OEM	Original Equipment Manufacturer
CFD	Computational Fluid Dynamics

ABSTRACT

The shock absorber system is part of a vehicle's suspension system. It controls consistent tyre contact with the road surface and damping of road induced. Shock absorber systems in most light vehicles are produced with set damping forces, tailored to Original Equipment Manufacturer (OEM) weight assumptions and even road conditions. However, in many parts of the world especially countries with poor roads such as Uganda, actual driving conditions differ. Roads are often un-even and potholed and this leads to increased wheel travel and excessive stress on shock Absorber components resulting in low service life. With the goal of improving ride comfort, stability, and durability over uneven potholed roads, this study re-designed a telescopic shock absorber system for a light passenger car (Toyota Wish) addressing these challenges. A study was made to ascertain the technical capabilities required for the local manufacture of the redesigned coil spring and damper. Design parameters were obtained from computations using derived scientific formulas and equations. While SolidWorks aided in Computational fluid dynamics (CFD) and finite element analysis (FEA), ShimRestackor studied damping properties to validate the new shock absorber system design. The simulation results have shown that the duo, 6-active turn Chromium-vanadium Coil Spring of wire diameter 14.4mm and free length 342mm with spring rate of 33.7 $\times 10^3$N/m and a damper of 150mm stroke, peak force of 3.12KN (Rebound) and 1.58KN(Compression) with a tuned valve configuration system and damping coefficient of 0.35 are capable of handling and tolerating more weight, absorbing sudden impacts while maintaining sufficient ride height and stability. A high damping efficiency was achieved vindicated by compression chamber pressure rise from an initial 0.8 MPa gas pre-charge to approximately 2.5 MPa at full compression stroke, and over 3.75 MPa. Furthermore, the manufacturing Cost modelling showed that at $\geq$ 8000 units/ month, the hybrid system undercuts fully imported units by $\approx$ >20%, which percentage can be increased given government intervention through policy amendments and funding. The redesigned shock absorber is expected to give smoother rides, lower vibrations, and a service life of over 5 years, thereby improving vehicle safety, stability, durability, and overall affordability.

Key words: Shock absorber, ride comfort, manufacturability and un-even roads

CHAPTER ONE : INTRODUCTION

1.1 Background

In the suspension systems of different cars, especially motor vehicles, the shock absorber system is vital. It enhances the overall ride quality, safety, comfort, and stability of the car (Vidhyathar, 2019). Alongside these functional demands, modern design practice must also verify whether the assembly can be manufactured economically. This may be either fully in house or as a hybrid of locally machined and imported sub-assemblies, without compromising performance. One of the biggest challenges in the design and engineering of the shock absorber systems is striking the correct balance between longevity, manufacturability and performance, particularly in situations when cars are driven on poorly maintained roads (Manga, 2018).

1.1.1 Actual Driving Conditions

The conditions in which vehicles are driven mainly rely on four elements; the weight carried by the vehicle, the nature of road imperfections, the speed of the vehicle, and the surrounding temperature and these highly affect the durability of Shock absorber systems (Pavlov, 2017). Road irregularities result in cars moving vertically, longitudinally, and laterally, which greatly reduces passenger comfort. Moreover, pulling the wheels off the ground on a regular basis decreases the effectiveness of the brake and power transfer systems (Jan , 2012). Non-adjustable shock absorbers intended for smooth roads such as that shown in Figure 1.1(a) are usually installed by automakers at modest speeds, with standard temperatures of 20°C, which correspond to typical atmospheric conditions, and moderate loads (about 70–80% of maximum capacity). Passengers will notice less vibration and less vertical acceleration because of this arrangement. However, real-world circumstances such as potholed roads illustrated in Figure 1.1(b), where these vehicles are used differ greatly from those assumed by the manufacturer in many cases (Pavlov, 2017).

(a) (b)

Figure 1.1:(a) A smooth road in Japan where shocks are manufactured to operate (Lane, 2022) and (b) Uganda road where the same cars are driven (Mwenda, 2023).

Potholes on roads as shown in Figure 1.1(b) lead to increased wheel travel, resulting in greater force and stress on shock absorbers, which can cause defects and failures. In areas where most roads are characterized by potholes, dust, mud, and waterlogged ditches during rainy seasons, shock absorber defects and failures are common (Ndagano, 2022; Mwenda, 2023). According to Bogie (2014), defective suspension, more specifically, problems with shock absorbers is the third most common technical factor that causes accidents, accounting for about 20% of incidents. It can also shorten tire life, accelerate the deterioration or failure of brake systems and other chassis parts, and raise maintenance and operating costs (Ryabov & Pozdeev, 2019). Strong shock absorbers are necessary to withstand a variety of impacts and maintain vehicle stability and comfort since the energy absorbed by the shock absorber increases noticeably with higher vehicle speeds, more vehicle mass, and deeper pothole depth.

While developing countries still grapple with public transport challenges, Toyota vehicles have for a long time proved sustainable for use as public transport vehicles with a Toyota cabin 1990 at its back bone. However, the Toyota Wish has gained popularity as a taxi in many parts of Uganda, especially in semi-urban or rural areas with uneven potholed roads

(kamuhanda, 2008). The Toyota Wish's shock absorber system sometimes fails before its predicted 80,000 km (4-5 years) life span because of the difficult terrain (Azuma, 2024). This is primarily because the majority of shock absorbers system available in the local market are not specifically engineered to withstand the difficulties of uneven potholed roads. Furthermore, little studies have been carried out to ascertain the contribution of varying average weights of people, road conditions and driver discipline towards shock absorber performance and safety. Even with emphasis on import substitution strategy that gives light for local manufacturing in developing countries, there is no evidence for sound technical judgements in regard to choose of materials, tolerances, and surface finishes that should be achieved for certain products which undermines their quality. Such shock absorbers not only result in inadequate control of spring and suspension movements, diminished comfort, and safety concerns, but they also restrict consistent contact between the tires and the ground surface at all times (Ashwini, 2021).

The aim of this research is to improve the performance of the shock absorber system on pot holed uneven roads by redesigning the light vehicle shock absorber system and evaluating the effectiveness and functionality of the updated design. A manufacturability assessment was carried out based on Design for Manufacturing and Assembly (DFMA) and economic tools to evaluate local production feasibility and facilities' capacity. On uneven roads, the shock absorber's usability was maximized by the revised design. The resulting suspension aims to maximise service life, ride comfort, and safety on uneven roads while remaining feasible for production in the Ugandan context through a cost-effective hybrid supply chain.

1.2 Problem Statement

Light vehicles in Uganda are often driven on uneven terrains characterized by potholed roads, rough roads and unpaved dusty roads. Under these conditions, the shock absorber

system, a critical component of the vehicle's suspension system, is exposed to high levels of stress and wear facilitating damper leakages as well as coil spring and damper shaft yielding. These deteriorations result into unprecedented system failures and undermine their service life. Even though, the existing shock absorbers are wholly designed for vehicle stability and safety; uneven, unpaved or dirt Roads pose a significant trial to their design firmness towards ride comfort and longevity. Therefore, this research addresses this problem while exploring the need for specialized design and re-designing of shock absorber system to achieve a long lifespan when used on unpaved or dirt roads. In addition, it evaluates the manufacturability of the redesigned shock absorber to confirm that the designed system can be economically produced, assembled, and serviced with the capabilities available in Uganda.

1.3 Research Objective

1.3.1 General Objective

To redesign and carry out manufacturability assessment of a telescopic shock absorber system for light vehicles to Enhance Performance on Pot-holed uneven roads

1.3.2 Specific Objectives

(i) To determine the Light vehicle shock coil spring parameters for optimal performance on uneven roads

(ii) To develop a stable damper to reduce the impact of bumps and vibrations.

(iii) To conduct CAD simulations to optimize shock absorber performance and validate effectiveness

(iv) To assess the technical requirements for the manufacture of the designed shock-absorber system within Uganda.

1.4 Justification

The goal of this dissertation research is to improve the performance of light vehicle shock absorber systems over uneven terrain and to assess the manufacturability of the design in Uganda. This is especially important given Uganda's large network of unpaved roads. Focusing on the Toyota Wish, a well-liked car in the area, the study attempts to reduce early shock absorber failures, which raise maintenance costs and cause accidents.

This dual technical and economic focus directly aligns with United Nations Sustainable Development Goals. These include SDG 9 *(*Industry, Innovation and Infrastructure*)*, SDG 11 *(*Sustainable Cities and Communities*)*, and SDG 3 *(*Good Health and Well-being*)*. Improved shock absorber performance enhances transportation safety (SDG 3), while local production supports sustainable industrial growth and innovation (SDG 9). Reliable transport infrastructure improves accessibility and mobility, particularly in underserved rural areas, thus contributing to SDG 11. Therefore, the outcomes of this research are expected to generate not only engineering benefits but also broader socio-economic and environmental impacts.

1.5 Significance of the Study

The urgent problem of insufficient shock absorber performance in bad roads such as those in Uganda's difficult driving conditions are addressed by this study. Through the application of analytical and design methodologies, the research produced a revised shock absorber system that is enhanced for robustness and efficiency on uneven terrain and assessed its local manufacturability as well. In the end, this improved car longevity, comfort, and safety, making transportation in Uganda safer and more dependable.

1.6 Scope and Limitations of the Study

1.6.1 Scope of the Study

The research is principally concerned with redesigning the light vehicle's shock absorber system and carrying out its manufacturability assessment. Scientific design methodologies have been investigated to boost the longevity and efficiency of the shock absorber system, specifically emphasizing the optimization of performance on unpaved or dirt roads as well manufacturability aspects.

1.6.2 Limitations of the Study

This study's focus is on redesigning the light car's shock absorber system and its manufacturability assessment. It may not immediately apply to other vehicle models other than that whose specifications have not been considered in this study.

Other suspension system parts of the car or possible interactions with other systems are not covered in this study.

Not every potential variable and element affecting shock absorber system performance under actual driving situations is taken into consideration in this study.

Unit costs, cycle times and quality levels are deduced from vendor datasheets, not pilot production, actual shop-floor performance could diverge once equipment is installed.

Projected yields and surface finishes assume access to high spec CNC coilers, temper furnaces and zinc-phosphate lines; substituting lower spec or differently configured equipment may reduce throughput or product quality.

1.7 Conceptual Framework

The conceptual framework explains how the independent variables (IV) of coil spring design, damper design, and computer-aided design (CAD) affect the dependent variables

(DV) of shock absorber performance, longevity, and material composition. It also describes how the redesigned shock absorber system works and performs as well as its manufacturability in Uganda. This framework has increased the quality and longevity of the shock absorber by methodically studying and redesigning it, hence improving vehicle safety, comfort, and lifespan on uneven roads. The correlations between these variables, including moderating factors, are shown in Table 1.1.

Table 1.1: A summary of the Conceptual Framework

Spring Design (IV)	Damper Design (IV)	CAD & Simulation (IV)
Wire diameter Coil spacing Number of active coils Spring material Heat treatment process surface finish	Damping coefficient Piston diameter & rod size Valve/shim-stack configuration Orifice / bleed area Fluid viscosity μ(T) Material selection for piston, tube, shims	Model geometry Boundary conditions & loading Mesh density & element type Time step / solver settings

Spring Design (DV)	Damper Design (DV)	CAD & Simulation (DV)
Spring rate *k*(kN/m) Deflection under curb & gross vehicle mass Stress distribution & factor of safety Ride comfort (vibration frequency/acceleration at body)	Damping force–velocity curve (F–v shape) Pressure drop ΔP across compression/rebound valves Energy dissipation per stroke Rebound/compression damping ratio Wheel velocity decay after bump	Von Mises stress in spring and damper components Displacements and deflections under dynamic loading Internal pressures & flow patterns in damper Dynamic response (wheel velocity vs time, body acceleration) Structural integrity versus material limits

Manufacturability in Uganda (IVs → DVs)	
Selected manufacturing; Equipment capability Sourcing strategy DFMA principles applied	Achievable dimensional tolerances and surface finishes Unit production cost Monthly output Quality metrics (fatigue life, leak rate, rework/scrap rate)

Final Dependent Variables/Out comes
• Improved ride comfort and handling stability on Ugandan roads • Reduced premature shock absorber failures and maintenance costs • Locally manufacturable spring–damper system at competitive unit cost • Support to local industry and BUBU policy through feasible production scales

Moderating / Context Variables (Affect O1, O2, O3 → performance; and O4 → cost & feasibility)
Toyota Wish sprung & unsprung mass, weight distribution • Road input severity: pothole depth up to 180 mm, rough unpaved roads • Local supply chain capacity (steel, wire, machining, coatings) • Economies of scale (500 vs 8,000 vs 282,000 springs/month; 24,000 dampers/month) • Exchange rate, import duties on inputs • Availability of skilled labor and technical support

CHAPTER TWO: LITERATURE REVIEW

2.1 Introduction

A summary of previously conducted research about motor vehicle shock absorbers is presented in this chapter. The main reason for this analysis was to thoroughly examine previous research and literature about vehicle shock absorbers systems to identify the relevant literature content, the areas where further research is required, and identify gaps in the knowledge.

2.2 The Shock Absorber System

The shock absorber system purpose is to provide a smoother and more stable ride by absorbing the effect of bumps and vibrations when the car is mostly traveling on uneven terrain (Ashwini, 2021). The shock absorber system is made up of springs, dampers, and struts, among other parts that cooperate to lessen the impact of uneven roads on the car. The shock absorber is a device that is designed to contain the impact of bumps and vibrations when the vehicle is moving mainly on an uneven road, providing a smoother and more stable movement (Manga, 2018).

The shock absorber system comprises various components like springs, dampers, and struts that work together to minimize the effects of road irregularities on the vehicle. The shock absorbers help to control the upward and downward movement of the vehicle suspension system, and ensure that the tires remain in contact with the road surface, improving traction and overall vehicle movement (Dixon, 2007).

The shock absorber system is designed mainly for two functions; to reduce and manage the impact of shock forces within a vehicle, and to maintain the tyres in contact with the road by regulating the rebound of the suspension spring (Baiyang, 2023). Shock absorbers

furthermore help in controlling how the suspension system and springs operate to enhance ride comfort (Han, Zhang, and Cheng, 2021).

In light weight vehicles, telescopic shock absorbers are employed to control suspension motion through the use of hydraulic damping principles (Milliken & Milliken, 1994). To improve passenger comfort and achieve overall optimal vehicle performance, automotive engineers must always carefully develop and analyse the respective shock absorber systems. (Manga, 2018).

2.2.1 Shock Absorber Working Principle

Shock absorbers are designed to operate by the help of a spring to keep the tyre *c*ontact patch on the road surface. When the tyre experiences a bump, the damper compresses the spring and still controls the wheel vertical travel preventing overshoot. During the return, the damper absorbs the energy stored in the spring during compression and enables a smooth travel. When the tyre experiences a depression, the shock absorber operates in tension to the limit allowed by the damper and retracts once the tyre moves out of the depression (Baiyang, 2023). The most significant contributor to any vehicle's mechanical grip is good damper control. Mechanical grip is entirely about the ability of the tyre patch to remain in desirable contact with the road surface, with as little excitation as possible.

The Shock absorber can therefore be better called an energy absorbing device that works on the energy conversion principle to stop the moving load with minimum load rebound and shock, to the load and the surrounding components (Simon & Festo, 2020). The shock absorber components accomplish their tasks by absorbing energy. In the spring and snubber system, energy is stored during the compression and released to result into rebound. In a dash pot on the other hand if a force acts against the piston, it encounters high resistance from the fluid at the beginning of the stroke, then much less as the piston retracts. However,

the spring and snubber, and dashpots shock absorbers face a working limitation whereby they do not dissipate energy uniformly. The energy is transferred to the load uniformly only in the case of shock absorber (Jihao, 2020).

2.3 History and Evolution of Shock Absorbers

The development of shock absorber systems started with the friction dampers which were first developed in the early 1900s (Pinjarla & Lakshmana, 2018). Their mode of operation was using stacks of friction discs to restrict spring movement, and the friction discs could be manually adjusted for various road conditions. They later advanced from basic springs to sophisticated damper systems, and finally to the MacPherson strut system which is one of the most commonly used type currently.

Comprising piston and cylinder designs and filled with hydraulic fluid for energy absorption and dissipation, hydraulic shock absorbers first appeared in the 1930s (Dixon, 2007). Designed by Gabriel Snubber in the 1950s, telescopic shock absorbers transformed shock absorption with their more efficient and compact forms. They use nitrogen gas to improve damping performance, which improves control and stability on a variety of road conditions (Pinjarla & Lakshmana, 2018). Around the turn of the millennium, adaptive shock absorbers which could automatically modify damping based on actual driving circumstances and improve handling and ride comfort were made possible by electronic integration into suspension systems. Regenerative shock absorbers are a recent development in shock absorber technology that aims to transform kinetic energy into electrical energy. This development reflects continued efforts to improve shock absorber system efficiency and sustainability.

2.4 Classification of Shock Absorbers

Due to the application diversity of shock absorbers, they can be classified by their operation mechanism, their construction and their applications.

2.4.1 Classification Based on Operation Mechanism

This type of shock absorbers is mainly distinct because of their mode of operation. They are mainly characterized as;

Hydraulic shock absorbers, relied upon for their simplicity and adaptability, they utilize fluid dynamics to regulate motion and vibrations, relying on liquid viscosity and damping properties (Jue, 2023) and (Zdzisław, 2021). By forcing fluid through valves or other orifices as the suspension moves, the piston goes through the cylinder, generating resistance that absorbs and lessens shocks and vibrations (Pinjarla & Lakshmana, 2018). In comparison to conventional shock absorbers, gas-filled shock absorbers are better in terms of performance and stability and are specifically intended for use in automotive applications (Jue, 2023). To avoid fluid foaming and cavitation, they combine compressed gas usually nitrogen with hydraulic fluid (Nikolay, 2017).

A potential replacement for conventional mechanical shock absorbers, electromagnetic shock absorbers (EMSA) enable adaptive damping and energy recovery by transforming kinetic energy into electrical energy (Bae, Hwang, Roh, & Yi, 2015). In comparison to conventional shock absorbers, electromagnetically forced shock absorbers (EMSA) have better damping ratios and energy absorption capacities, which significantly reduce vibration and noise in a variety of applications (Amati, Andrea, & Tonoli, 2011). However, optimising the EMSA design and control strategies remains a challenge, and further research is needed to fully explore their potential in various industries.

2.4.2 Classification Based on Construction

According to construction of shock absorbers, they can be classified into two categories; twin-tube and mono-tube constructions. Each of them has distinct design features and performance characteristics.

Twin-tube shock absorbers as shown in Figure 2.1, comprise two nested cylindrical tubes, with the inner working tube housing the piston and hydraulic fluid, and the outer reservoir tube containing excess fluid, and a low-pressure gas charge in some cases (Pinjarla & Lakshmana, 2018). According to Teerapharp et al., (2014), this design offers an affordable, robust, and adaptable option for a variety of vehicles, although it may have limitations in terms of heat dissipation and dampening capabilities when used heavily or for an extended period of time. To improve damping effectiveness, avoid aeration, and guarantee consistent damping performance, a gas charge typically nitrogen is incorporated into the upper outer reservoir tube (Pavlov, 2017).

The mono-tube shock absorbers on the other hand feature a single tube divided into two chambers by a floating piston, separating the hydraulic fluid and high-pressure nitrogen gas, facilitating superior heat dissipation and consistent performance (Lalitkumar, Shankar, & Sawant, 2016). Overall performance and manoeuvrability, decreases unsprung weight, and provides a variety of installation alternatives (Prashant & Aitavade, 2014).Due to their quick response time and dependable damping properties, mono-tube shock absorbers are quite popular in racing and performance automobiles. They are best suited for harsh road conditions and high-performance uses (Zhifei, 2021).

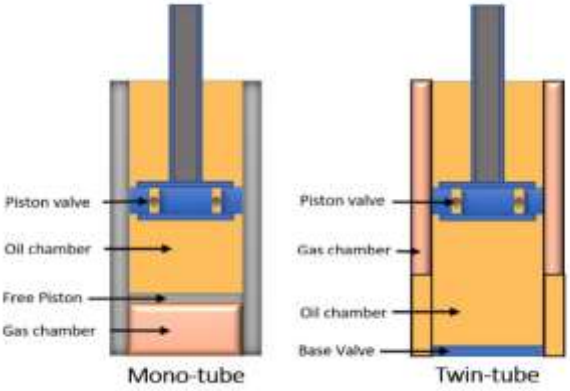

Figure 2.1: Illustration of passive Mono-tube and Twin-tube shock absorbers (Lundberg, 2021)

2.4.3 Classification Based on Application

Different types of shock absorbers are made for particular industries and purposes; thus, they can also be categorized based on how well they work. Comfort, control, and longevity are the top priorities for automotive shock absorbers used in heavy-duty trucks, performance automobiles, and passenger cars. Industrial shock absorbers shield machinery from harm by absorbing and distributing energy in mechanical systems. Extreme circumstances are handled by specialized shock absorbers, such as seismic and aeronautical versions, in earthquake engineering and aircraft landing gear (Spiteri, 2019).

2.4.4 Classification Based on Adjustability

There are two primary types of shock absorbers: adjustable and non-adjustable. The manufacturer of non-adjustable shock absorbers sets a predetermined damping rate that is optimal for most drivers' comfort and performance levels. On the other hand, drivers can manually or automatically adjust the damping settings of adjustable shock absorbers through electronic control systems to accommodate various driving situations or personal tastes. The specific requirements of the car, piece of equipment, or structure, as well as the expected operation conditions, determine which shock absorber is best. (Więckowski, 2018).

2.5 The Macpherson Strut Suspension System

The MacPherson strut suspension as illustrated in Figure 2.2 is a simple independent suspension design currently adopted by most car manufacturers, mainly for front wheels. It capitalizes around a basic triangular design with two major parts; a control arm and a radius rod, forming a triangle against the car's chassis at the bottom end of the suspension system (Jain, 2014) .They consist of a gas-filled or oil-filled cylinder with a sliding piston inside, whose top is connected to the vehicle's body, and the bottom is to the wheel assembly.

The MacPherson shock absorbers create a dampening for the vertical motions of vehicle wheels; when the wheel encounters a bump or depression in the road, the piston inside the cylinder moves down and up respectively, forcing the hydraulic fluid or gas in the cylinder to pass through small orifices located inside the cylinder (Spiteri, 2019). By doing this, the motion of the wheel is transformed from kinetic energy to thermal energy, which effectively dampens vibrations and lessens the impact on the occupants of the vehicle. In general, the Macpherson strut suspension system smoothens out the ride by enhancing handling, stabilizing the vehicle, and allowing for greater suspension system movement.

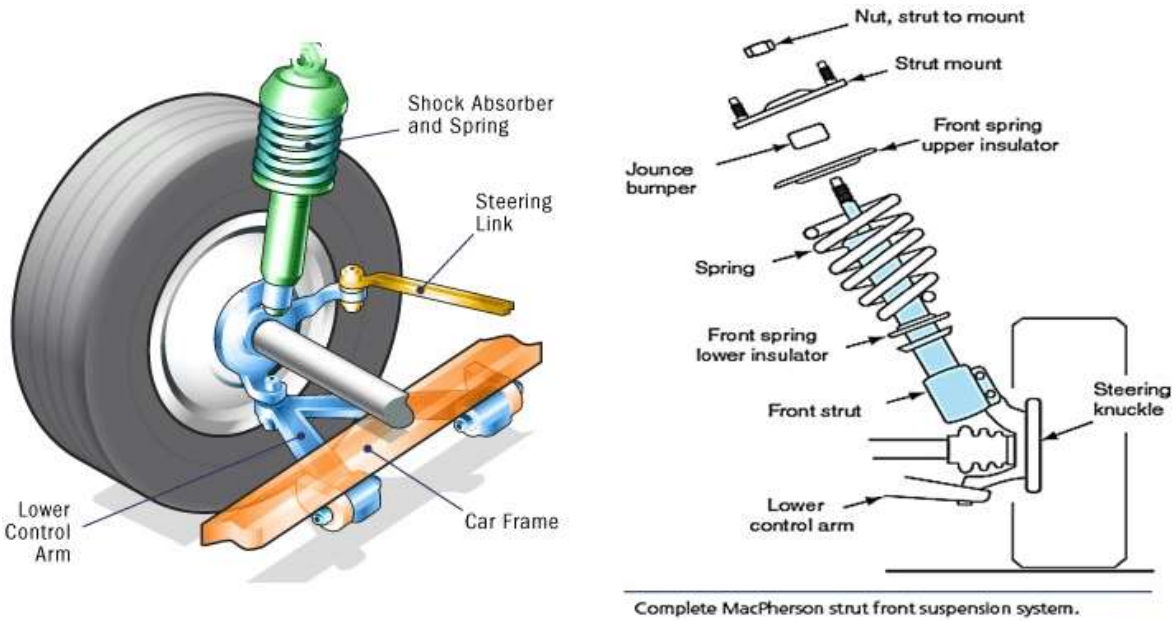

Figure 2.2: Illustration of the Macpherson shock absorber (Pavlenko, 2024)

2.6 Existing Coil Spring Design

Coil springs operate based on Hooke's Law, which describes the relationship between force (F) and deformation within the material's elastic limit. An essential design factor is the spring rate (k), which determines the stiffness of the spring under load. In his research, Dumitru Pop et al. (2018) and (Raijade & Seshagiri Rao, 2015) investigated the effect and characteristics of variable wire diameter on the spring rate, demonstrating that larger diameters result in stiffer springs but also higher stress concentrations. The importance of balancing stiffness with material strength to avoid premature failure due to excessive stress is highlighted by their findings. Siddharth, Dipender, and Surabhi (2021) designed a cylindrical spring with a variable pitch using chrome vanadium. They explored how adjusting the coil pitch via computer-aided design (CAD) can fine-tune the spring rate and performance characteristics. They discovered that varying the coil pitch creates a balance between comfort and performance, making these springs ideal for vehicles that need to handle both rough and smooth terrains effectively. Additionally, they found that Chrome Vanadium can successfully replace high-carbon steel springs, thereby enhancing the suspension system performance.

2.6.1 Coil Spring Design Considerations

Key design considerations influence the performance and durability of coil springs. These factors include stress distribution, fatigue resistance, and buckling prevention. Henry August Wahl made significant contributions to the design of coil springs, specifically in understanding how stress concentrations at the inner coil surface can cause fatigue failure. His work introduced the Wahl factor, which is used to correct these stress concentrations in design calculations, thereby significantly improving the fatigue life of springs. Jihao and Dong (2020) conducted a performance analysis of coil springs and studied how the spring index (C), which is the ratio of coil diameter to wire diameter, affects stress distribution.

They discovered that springs with lower indices below 4 had higher stress concentrations, making them more susceptible to fatigue. However, they also observed that these types of springs could be useful in designs with limited space, as they enable a more compact coil geometry. In automotive applications, where space efficiency is crucial, these findings help engineers optimize the design to meet spatial and performance requirements.

2.6.2 Materials used for existing Coil Springs

In the spring design process, choosing the right spring material is essential for dependable coil spring operation (Jihao, 2020). It establishes the spring's durability and mechanical characteristics. Because of their high tensile strength and resilience to fatigue, traditional materials like high-carbon steel alloys, chrome silicon (Cr-Si) and chrome vanadium (Cr-V) are utilized extensively. Because it is less expensive than chrome silicon (Cr-Si) and still provides the same characteristics for the coil to function effectively, chrome vanadium (Cr-V) is frequently utilized (Issifu, 2023) .

The design of coil springs for shock absorbers has recently focused on lightweight materials like titanium and composites. Although titanium has a better strength to weight ratio than other metals, its greater cost prevents it from being widely used in coil springs, according to research on the subject (Sanghavi et al., 2007). Additionally, Singh et al.'s (2022) study on carbon fiber-reinforced polymers (CFRP) as a substitute for conventional materials revealed encouraging outcomes in terms of weight reduction while preserving strength, despite ongoing issues with fatigue and long-term durability that underscores their contribution and widespread adoption. Quenching and tempering are two crucial heat treatment procedures that improve the material's mechanical qualities, such as strength, hardness, and fatigue resistance, and prolong the spring's life under cyclic loading circumstances. Additionally, surface treatments like coatings and shot peening increase longevity and corrosion

resistance. Coatings shield the spring from environmental elements like moisture and road salts that can cause corrosion and early failure conditions, while shot peening creates compressive stresses to stop cracks from forming and spreading (Darko, Goran, & Bozic c, 2019). However, there is still need to develop novel alloys that will simultaneously offer optimal balance between corrosion resistance, tensile strength and fatigue resistance.

2.6.3 Stress Distribution

Stress distribution is very important across the entire cross-section of any coil spring, since it contributes to high structural integrity and fatigue resistance. Uneven stress distribution can lead to localized failures, making precise design and material selection crucial for even load bearing (Darko, Goran, & Bozic c, 2019). Investigations about tensile and compressive stresses, which are perpendicular to the spring's surface (Zhang, Cheng, & Han, 2021), showed that balancing all the stresses that can be experienced by the spring, ensures it can handle operational loads without excessive deformation and contributes to resistance to stretching or compression by the spring.

2.6.4 Ride Comfort

The significance of a spring's capacity to reduce vibrations and absorb shocks from uneven road surfaces was highlighted in a study on the impact of spring stiffness on passenger comfort (Prasad & Ajaykumar, 2021). Lower frequencies are always preferred to achieve ride comfort by the shock absorber, according to the study, which also indicated that perceived comfort is greatly impacted by the frequency and amplitude of vibrations conveyed through the vehicle chassis. Accurately adjusting the spring's properties is essential to reducing high-frequency vibrations brought on by road surfaces or vehicle dynamics and enhancing ride comfort. Its vital to acknowledge that challenges still exist in developing control measures to balance ride comfort with vehicle stability

2.6.5 Vehicle Weight

Heavy loads increase spring compression, necessitating stiffer springs or additional support to maintain performance, according to an analysis of how vehicle load and weight distribution affect spring compression and damping characteristics (Gonera, 2020). For balanced handling and stability, the vehicle's chassis must have the right amount of weight distributed across it. The handling and stability of the vehicle may suffer from an uneven load on the coil springs caused by an uneven weight distribution. Maintaining uniform weight distribution improves vehicle dynamics and maximizes spring performance.

2.7 Damper System Design

The vehicle's ability to withstand tire stress, stability, handling, and ride comfort are all directly impacted by the damper system, which is a crucial component of the shocker absorber system. It works in tandem with the coil spring. When designing a damper system, some of the most important parameters to take into account include

2.7.1 The Damping Coefficient (C)

This metric contributes to determining the damper's performance and indicates its capacity to disperse energy. In order to preserve vehicle stability and lessen oscillations, a stronger damping force is indicated by a higher damping coefficient (D. Mohankumar, Sabarish, & PremJeya Kumar, 2018). The formula below is used to get the damping coefficient

$$C = (2\pi fd)/(0.0000147) \qquad (2.1)$$

Where: C = damping coefficient (N/m), f = frequency (Hz), d = piston diameter (m)

2.7.2 The Piston Diameter

The piston diameter in shock absorbers affects how well the absorber system works. In addition to increasing damping and friction forces, a bigger piston diameter also results in higher pressure losses and decreased efficiency (Daniel & Grzegorz, 2021) . The particular

application and required trade-offs determine the ideal piston diameter. To increase piston efficiency, some research has looked into the use of different designs, like tapered or stepped pistons, or changing piston diameters (Zhiqiang, Chengjie, & Jie, 2023). The friction force and damping performance are also impacted by the material characteristics of the cylinder and piston, such as surface hardness and roughness. To forecast shock absorber behaviour and optimize piston diameter design, simulation models have been created (Yangyang, 2022).

2.7.3 Fluid Properties

The major fluid properties required for the fluid used in the piston are viscosity (μ) and temperature dependence. These impact the damping force and temperature sensitivity (Lukas & Johannes, 2022). The viscosity of the fluid in question is calculated by;

$$\mu = (2.42 \times 10^{-9})(T^2) - (1.37 \times 10^{-5})\ 0.0357 \qquad (2.2)$$

Where μ = viscosity (Pa·s) and T = temperature (°C).

2.8 Manufacturability of Shock Absorber System in Uganda

According to Xiayi (2015), Shock absorber parts demand extremely tight tolerances and smooth surfaces, e.g., Piston rods must be made of hardened, high-tensile steel, typically chrome-plated, with surface roughness on the order of Ra 0.2-0.6μm (Xiayi, 2015) well as Shim stack valves are stamped from high-carbon spring steel (Tradewheel, 2025). These shim plates are ground or punched to very strict thickness/flatness tolerances (often ±0.004–0.007m) so that damping orifice sizes are exact (Tradewheel, 2025). On the other hand, Coil springs are cold-wound from quenched alloy steel and shot-peened or hot wound. They must meet DIN2095 grade tolerances of which for high-precision springs (Grade 1) free-length is ±1%, and coarse springs allow ±3% (Tevema, 2022). In short, manufacturing shock

absorbers involves CNC milling, grinding, hardening and plating operations at precision far beyond typical fabrication workshops.

In Uganda, however, few factories have the needed equipment or inputs. A recent study published by the nilepost found local manufacturers running at only at 54% capacity, often due to poor access to inputs (Matovu, 2024). Advanced CNC mills, 5 axis lathes or precision grinders standard in shock-absorber factories abroad are scarce locally. Most metalwork is done on manual or basic CNC machines and this limits achievable tolerances. UMA surveys reported that roughly 2/3 of Ugandan manufacturers struggle to find skilled machinists and technicians (Namagembe, 2024). Raw materials are another bottleneck: local steel and precision tubing are often low-grade or inconsistent, forcing firms to import blanks and component (Matovu, 2024). High production costs (taxes, import duties, expensive power) make local shock fabrication uneconomical, so most parts are imported. In summary, Ugandan industry is challenged by outdated machine tools and CNC scarcity, skills shortages, limited quality materials, and high operating costs.

Some comparators show how local manufacturers overcome similar hurdles. In South Africa, Gabriel SA has produced automotive shocks locally since the 1960s to meet content rules (Arrivealive, 2012). Gabriel SA built a Cape Town factory in 1962 and, by the 1990s, had adopted lean manufacturing to eliminate waste and raise efficiency. The company reportedly tailors its designs to South African conditions and maintains a full machining line in country. In Asia, Kayaba (KYB) has likewise forged local partnerships: e.g., in 2013 KYB and Yamaha formed a joint venture to make motorcycle shock absorbers for Southeast Asian markets (Yamaha, 2013). Such examples illustrate that even in emerging economies, shock absorber producers invest in local precision machining and supply chains (often via technology transfer or Joint Venture) to ensure competitiveness. Uganda would similarly

need to establish localized machining capabilities (CNC toolings, heat treatment, plating) to assemble shocks domestically, rather than rely on imports fully.

2.9 Summary of Literature Review and Research Gaps

The studied literature indicates that shock absorber systems have evolved over the years with many different systems from respective manufacturers. However, MacPherson-strut layouts dominate light-vehicle front suspensions because they combine packaging efficiency with predictable kinematics. Chrome vanadium is highly recommended for manufacture of coil springs since it is cheaper compared to other materials but yet still delivers the required working conditions and parameters efficiently (Konieczny et al., 2016) and mono-tube dampers, particularly gas-charged variants, deliver faster heat dissipation and superior high-speed damping than twin-tube designs

Notwithstanding these advances, some interrelated gaps remain unaddressed. First, the majority of experimental data and design techniques have been derived under temperate climate highway conditions; little quantitative work has examined how the un-even road surfaces and frequent axle overloads, typical of Ugandan roads influence optimal spring indices, damping ratios, and fatigue safety factors. Second, the literature tends to treat coil-spring sizing and damper tuning in isolation, providing scant guidance on an integrated optimisation framework that simultaneously balances coil stiffness with damper so as to preserve tyre contact on low-grip terrain. Third, while feasibility notes exist on coil cold winding and monotube machining, peer-reviewed studies that translate those processes into Ugandan workshop capabilities and facility, covering tolerance windows, heat-treatment schedules and DFMA adaptations for small-batch production, are virtually absent.

CHAPTER THREE: METHODOLOGY

3.1 Introduction

This chapter presents a systematic approach used to achieve the study objectives of this project. It examined the respective approaches used to collect and analyze data about the Shock absorber designs and manufacturability. It also presents an overview of the engineering methodologies, scientific principles, and computational techniques used in designing the shock absorber coil spring, developing a high-damping-force damper system, conducting computer aided design simulations to optimize shock absorber performance and validate effectiveness while using on uneven roads as well as conducting a manufacturability assessment of its production locally.

3.2 Research Design

Both quantitative and qualitative methods were used in collecting the required data, to carry out the successful study. Quantitative research methods were used to determine the respective shock absorber system equipment, design parameters and details, system layouts, and operation simulation of the designed system. Qualitative research methods were used to analyse the shock absorber system operations and the different types of shock absorber systems that can satisfy the required design parameters.

3.3 Shock Absorber System Design

Shock absorber system design accounts for the steps considered in creating a mechanism that absorbs and dampens the respective impacts and vibrations experienced by a vehicle during motion.

3.3.1 Failure Mechanism of Shock Absorber due to Potholes

Figure 1.1(b) shows an example of a water-logged potholed road, these potholes lead to increased wheel or spring travel, which in turn amplifies the force and stress on critical components of Shock Absorber system.

$$F = kx \qquad (3.1)$$

Where k is the spring constant. Assume the Force (F) on the spring is directly proportion to the spring travel (x), as illustrated in equation (3.1)

$$\sigma = F/A \qquad (3.2)$$

where A is the cross-sectional area of the loaded component and σ is the stress on the shock absorber assembly.

Raised stress levels lead to premature wear, defects such as fluid leakage in hydraulic shock absorbers, and eventual failure of the damper. This compromiseses the shock absorber assembly's ability to effectively absorb shocks and ensure occupants safety. Figure 3.1 portrays some of the road pothole's impact on a Shock Absorber system.

Figure 3. 1: A faulty Shock absorber with Fluid Leakages (Left) and a broken Shocker Absorber Piston after hitting pot hole. (Right)

3.3.2 Pothole Impact with the Combination of Vehicle Mass and Speed

Figure 3.2 shows the connection between the increased impact and the vehicle mass, and Equation (3.3) and (3.4) illustrate how pothole effects on sink speed and pothole depth cause an increase in both kinetic and potential energy E

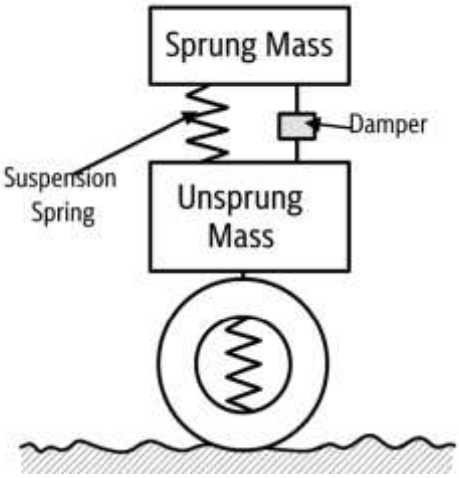

Figure 3. 2: Sprung mass and unsprung mass, damper dynamics

From,

$$E = \frac{1}{2}mv^2 \qquad (3.3)$$

$$E = mgd\ ,\ since\ v = \sqrt{2gd} \qquad (3.4)$$

Where g, is the acceleration due to gravity, higher vehicle speed, more vehicle mass, and deeper pothole depth (d) result in a significant rise in the energy E absorbed by the shock absorber and the sink speed (v). Thus, greater speed, mass, or pothole depth proportionally raises damper energy demand, necessitating stronger shock-absorber designs.

3.4 Target Shock Absorber System Performance Parameters

3.4.1 Pothole Characterization

To determine subsequent sizing computations, A pothole depth of 180mm as illustrated in Figure 3.3 was chosen based on both local standards and real-world vehicle dynamics. Uganda's Ministry of Works and Transport defines potholes over 100mm as severe defects

(MoWT, 2010). Designing for 180mm nearly double ensures the suspension can handle worst-case road conditions, especially on rural roads.

The Toyota Wish, used as the reference vehicle, has a ground clearance of~ 150mm (Carused.jp, 2025). A 180mm pothole exceeds this, meaning the wheel would drop fully into the hole, risking bottoming out unless sufficient suspension stroke and damping are provided. Simulation data shows such impacts can exceed 100g in shock load if not properly mitigated (Kamal et al., 2015), and can cause damage to tires, rims, and shocks (Kowalski, 2025).

A smaller design depth (e.g., 100 mm) would underestimate risk, while 250 mm would be impractical. The 180mm depth balances practicality and design feasibility. This choice aligns with global practices: for instance, Ford tests suspensions using 0.18–0.20m potholes on its Lommel proving ground (Ford Motor Company, 2016). Thus, 180mm is a rational benchmark for extreme but realistic shock absorber design.

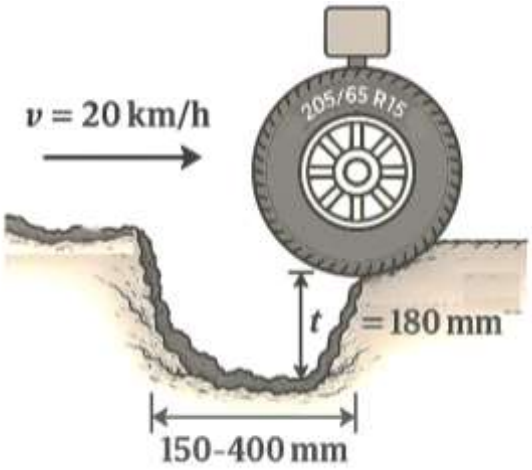

Figure 3.3: Illustration of Road Pothole for Characterisation

Furthermore, it was considered that the pothole was encountered at a velocity of 20km/hr. (5.56m/s), which is below the busy traffic urban roads regulatory recommended speed of

30km/hr as per The Traffic and Road Safety (Prescription of Speed Limits) Regulations, 2024 of Uganda. This speed represents deliberate, cautious driving over a known obstacle and keeps tyre deflection within a realistic operating band however this may differ from driver to driver and such a safety margin is considered. Tyre radial stiffness is set to 150kN/m, a value closely corresponding for a 205/65R15 tyre inflated to 250kPa. (Pacejka, 2006)

To model the pothole, the depression is idealized as a half-sine. This shape provided finite slopes and accelerations that avoids mathematical discontinuities, conformed well to field-measured cross-sections, and permits closed-form derivatives. These simplify the subsequent analytical work. All simulations therefore use the displacement input defined in Equation (3.5) over or close to the finite time window shown, applied directly at the tyre contact patch.

$$z_r(t) = \frac{d}{2}\left[1 - cos\left(\frac{\pi v t}{d}\right)\right], \;\; 0 \le t \le t_p = \frac{d}{v} = 0.036s \qquad (3.5)$$

t_p represents traversal time and all subsequent computations use equation (3.5) as the road-input displacement applied at the tyre contact patch.

3.4.2 Road-Profile Representation

The half-sine depression defined in equation (3.5) provided the complete time history of the wheel-pad displacement. That history drives both the tyre spring and the unsprung mass, so we required its velocity and acceleration as explicit inputs to the quarter-car model. In the time domain, differentiation of Equation (3.5) yields the wheel-centre velocity and acceleration as shown in equation (3.6).

$$\dot{z}_r(t) = \frac{\pi v}{2} sin\left(\frac{\pi v t}{d}\right), \ddot{z}_r(t) = \frac{\pi^2 v^2}{2d} cos\left(\frac{\pi v t}{d}\right). \qquad (3.6)$$

Both expressions reduce smoothly to zero at t=0 and again at $t=t_p$; consequently, the tyre never experiences a step-in velocity or an impulse in acceleration, thus avoiding unrealistic

loading spikes in the simulation. Because any transient can be decomposed into harmonic components, it was helpful to view the pothole in the frequency domain. A single half-sine contains the bulk of its energy in its fundamental harmonic as defined in equation 3.7.

$$\omega_r = \frac{\pi}{t_p} = \frac{\pi v}{d} \tag{3.7}$$

$$A_1 = \frac{2d}{\pi} \tag{3.8}$$

Practically, this meant that for frequency-response checks; such as evaluating the magnitude of the suspension transfer function G(ω) in Section 3.4.6, may approximate the half-sine event by a single sinusoid of amplitude, A_1 defined by Equation 3.8 at ωr. Higher harmonics carry less than 10% of the root mean square energy and are quickly diminished once magnitude of G(ω) falls off beyond the wheel-hop region; the tyre carcass and damper's high-frequency damping dissipate that remainder. Using the fundamental only therefore yielded a conservative yet computationally efficient estimate of peak spring deflection and body acceleration, while keeping the analytical chain entirely traceable for design verification.

3.4.3 Sprung and Unsprang Mass Valuation

Coil springs in the front suspensions of passenger cars are generally heavier than those in the rear due to the greater concentration of the vehicle's weight at the front (Htay Htay Win et al., 2019). Toyota Wish weight-distribution data (Appendix A.1) show Front to Rear weight ration corresponding to 58:42 at 1,300kg curb weight, shifting to 52:48 at 1,686kg gross weight. For this study we adopted a target gross weight of 1,750kg, considering 7 passengers of 65kg typical of Uganda setting (Kirunda, 2017). Extrapolating finally resulted in the Front to Rear weight ratio of 51:49 at 1.750Kg. An unsprung-mass fraction of 15 % of gross weight is used and allocated equally to each wheel SAE (Vadhe, 2018)), (Tang, 2014). The resulting sprung and unsprung masses of 379.31kg and 67kg per corner feed

directly into the quarter-car model, ensuring realistic static and dynamic inputs for uneven-road simulations. Detailed Numerical working in Appendix A.2.

3.4.4 Quarter Car Model Design

Suspension parameter selection in this study rests on the well-known two-degree-of-freedom (2-DOF) quarter-car model**,** widely adopted because it captures the essential vertical dynamics with minimal complexity (Bose, Rajasimman, & Prabu, 2020), (Gonera, 2020). The model represents one wheel station of the vehicle, separating the sprung mass and unsprang mass as shown in Figure 3.4.

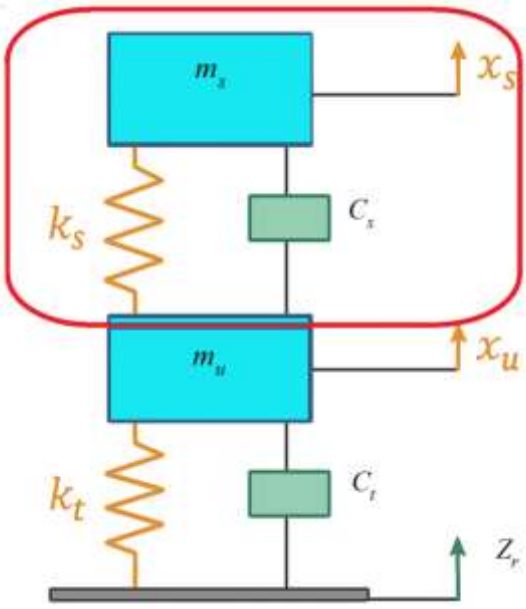

Figure 3. 4: A schematic diagram of a Quarter Car Model

A spring damper pair connects the sprung mass, m_s, to the unsprung mass, m_u, the tyre acts as a second spring k_t between m_u and the road profile $z_r(t)$. Applying Newton's second law to each mass gives the coupled differential equations

$$m_s\ddot{x}_s + c_s(\dot{x}_s - \dot{x}_u) + \kappa_s(x_s - x_u) = 0, \quad (3.9)$$

$$m_u\ddot{x}_u + c_s(\dot{x}_u - \dot{x}_s) - \kappa_s(x_u - x_s) + \kappa_t(x_u - z_r(t)) = 0, \quad (3.10)$$

Where x_s and x_u denote the vertical motions of the vehicle body and wheel assembly, respectively, c_s and c_t denotes the suspension damping coefficient and tire damping coefficient respectively, while k_s and k_t represents the suspension and tire stiffness accordingly. $Z_r(t)$ represents the road profile which acts as the base excitation for the system, and it is assumed to be sinusoidal.

For compact notation and later simulation, the system is reorganised in state-space form with

$$y(t) = [x_s, \dot{x}_s, x_w, \dot{x}_u]^T \quad (3.11)$$

Serving as the analytical backbone of this project, the quarter-car model played two critical roles in this study design;

1. First, closed-form manipulation of the governing equations (3.9) and (3.10) provides the two natural frequencies (sprung and unsprang) and corresponding damping ratios, which in turn allowed us to back-solve the target suspension spring rate k_s and damping coefficient C (detailed in Section 3.4.5).

2. Second, the model receives direct excitation from the half-sine pothole of Equation (3.5), a 180mm depression traversed at 20km/hr through the tyre term $k_t(x_u\text{-}z_r)$, ensuring that the tyre's compliance and inertia are faithfully represented.

By affixing all calculations to this model and populating it with Toyota-Wish-specific masses and tyre stiffness, we establish a transparent foundation from which every downstream parameter, spring geometry, damper parameters, gas volume, and bump stop clearance can be derived.

3.4.5 Definition of Target Suspension Parameters

1. Comfort (body-bounce) frequency(f_{n1}): Passenger-comfort studies and benchmark data for compact MPVs show that occupants experience least fatigue when the sprung mass natural frequency lies between 1.2 Hz and 1.5 Hz (Manga, 2018). And for purposes of this

academic work, a frequency of 1.35 Hz was used which places the Toyota-Wish body in the "comfort valley" while still leaving chassis room to raise the frequency slightly for extreme derivative.

2. Spring rate, k_s: Linearising the quarter-car equations (3.9) and (3.10) yields the characteristic relation

$$\omega_{n1}^2 = \frac{k_t k_s}{(k_t + k_s) m_s} \quad (3.12)$$

And therefore defines k_s as;

$$k_s = \frac{\omega_{n1}^2 m_s k_t}{k_t - \omega_{n1}^2 m_s} \quad (3.13)$$

This rate strikes the ride/handling compromise: soft enough to absorb surface undulations, stiff enough to control body roll and pitch during potholed uneven roads maneuvers.

3. Damping coefficient (C): A damping ratio of ζ=0.4 is chosen to approach critical damping without transmitting excessive high-frequency harshness.

$$C = 2\zeta\sqrt{k_s m_s} \quad (3.14)$$

Using Equation (3.14), with the damping ratio set to $\zeta = 0.40$, the suspension is expected to align with typical MPV ride targets on pothole uneven roads. Body-bounce oscillations fade within roughly two cycles, soft enough for passenger comfort yet still tight enough to keep the vehicle composed. All sizing and performance calculations that follow will therefore rely on the updated damping coefficients derived for this ζ value for reference.

3.4.6 Required Minimum Suspension Stroke from Pothole Event

Using the dominant half-sine harmonic of the pothole profile (A_1, ω_r) and the analytical transfer function for the magnitude of spring deflection $G(\omega)$ (full algebraic derivation in Appendix B), the gain at the excitation frequency can be computed using Equation (3.15)

$$|G(\omega_r)| = \frac{[k_t(k_s + jc\omega_r)]}{|D(j\omega_r)|} \quad (3.15)$$

Multiplying by the input amplitude yields the peak spring compression depicted by

$$X_{amp} = |G|A_1 \quad (3.16)$$

To cover higher-order harmonics, tyre-pressure scatter and manufacturing tolerances, a 20 % design allowance is adopted,

$$\Delta \boldsymbol{x}_{max} = 1.2X_{amp} \quad (3.17)$$

Equation (3.17) defines the minimum compression travel of the coil spring, damper and bump-stop must provide to clear the worst case 180mm pothole without coil clash or bottom-out. This expression is obtained entirely from closed-form Laplace (transfer-function) analysis, the full formula set appears in Appendix B.

3.4.7 Nonlinear Quarter-Car Dynamics for Extreme Road Events

While the linear 2-DOF quarter-car model is used to size the primary key suspension parameters (spring rate, damping, natural frequency) at estimated worst case scenario of 180mm pothole, at a speed of 20km/hr. However real-world conditions can occasionally exceed this threshold. For instance, traversing potholes of the same depth at 60 km/h, whether due to driver error or unavoidable traffic dynamics, can induce non-linear suspension responses well beyond the limits of the linear model. This creates extreme nonlinear responses. Although it may be attributed to negligence, comprehensive safety measures have been implemented in this design to mitigate risk. This requires modelling non-linear response features that are only activated beyond design thresholds. To this end, the present study incorporated targeted non-linear extensions to the linear model. These include bump-stop engagement and tyre de-contact logic. Each becomes active only when specific displacement or velocity thresholds are exceeded.

These non-linear features do not alter the baseline design values derived analytically in Sections 3.4.1 to 3.4.6, but act as protective overlays that conditionally modify the system's response under un-desirable high-energy inputs that are even far beyond our worst-case pothole scenario. Their formulation and design implications are detailed below;

(i) Bump-Stop Engagement -Spring Integrity: When the suspension compresses beyond its allowable jounce travel, δ_b, a stiff bump-stop pad takes over the load path to prevent coil clash and structural damage.

Trigger

$$z_s = x_s - x_u > \delta_b = \Delta x_{max} \tag{3.18}$$

Force law

$$F_s(z_s) = \begin{cases} k_s z_s, & z_s \leq \delta_b \\ k_s \delta_b + k_b(z_s - \delta_b), & z_s \geq \delta_b \end{cases} \tag{3.19}$$

With $k_b = 5k_s$

(ii) Tyre De-Contact -Preventing Negative Wheel Load: If the wheel outruns the road surface and begins to lift off, the tyre can no longer generate upward force; the model therefore sets the vertical tyre load, F_t, to zero until contact is re-established.

Trigger

$$x_{\mathrm{u}} - z_{\mathrm{r}}(\mathrm{t}) < 0 \Longrightarrow \mathrm{F_t} = 0$$

Force law

$$\mathrm{F_t}(x_{\mathrm{u}}, z_{\mathrm{r}}) = \max[0, \mathrm{k_t}(x_{\mathrm{u}} - z_{\mathrm{r}})]$$

The tyre can push the wheel upward but never pull it downward.

Modified Equations of Motion (Non-Linear Only Beyond Limits)

$$m_s \ddot{x}_s + c_0(\dot{x}_s - \dot{x}_w) + F_s(x_s - x_u) = 0, \tag{3.20}$$

$$m_u \ddot{x}_u + c_0(\dot{x}_u - \dot{x}_s) - F_s(x_s - x_u) + F_t(x_w - z_r) = 0 \tag{3.21}$$

These model equations collapse back to the linear form during normal operation and only activate their extended logic under;

$$z_s > 0.0574\text{m} \text{ bump-stop active}$$

$$x_u < z_r \rightarrow \text{tyre force zeroed (free flight)}$$

3.4.8 Benchmark and Compliance Check

Table 3.1 summarises the key dynamic metrics planned for the proposed suspension and benchmarks them against typical multi-purpose-vehicle (MPV) targets and relevant standards to verify compliance

Table 3.1:Key dynamic metrics calculated for the proposed suspension and benchmarks

Metric	**Derived Value (Study Result)**	**Typical MPV Range / Limit**	**Source (Standard/Reference)**	**Pass/Fail**
Body natural frequency (f_{n1})	1.36Hz	1.0-1.5Hz	ISO 2631-1:1997	Pass
Wheel-hop frequency (f_{n2})	10.5 Hz	6-12Hz (typical wheel/tire-hop frequency in cars)	SAE,(Tiwari et al., 2018)	Pass
Peak vertical body acceleration (pothole)	2.4m/s²	<0.7g	(Kennedy et al., 2004)	pass
Suspension spring rate (ks)	34kN/m	20–50 N/mm for compact MPV coil springs	Toyota Wish OEM / aftermarket(*S-Style C : WISH*, n.d.)	Pass
Suspension travel (x)	150mm	100-200mm	Industry design guides	Pass

3.5 Objective One: To Determine the Light vehicle shock coil spring parameters for optimal performance on uneven roads

3.5.1 Spring Stiffness (k)

This defined as the force required to cause a unit displacement in a spring. There are two main methods for determining the spring stiffness i.e., Natural Frequency and Maximum Displacement method, all of which determine the Wheel rate that is then used with the Motion Ratio to derive the spring stiffness as shown in equation (3.22). Because both these techniques are pertinent to the analysis and findings, they will be used in this study

$$k = WR \times (MR)^2 \tag{3.22}$$

MR stands for Motion Ratio

1. Spring Stiffness from Natural Frequency

Using the relationship in equation (3.13), the spring stiffness was calculated from the natural frequency, f, of the suspension system. A value between 1.0-2Hz was selected and befitted the customized purpose for the vehicle's usage in this study to fit the uneven road profile. There after wheel rate is calculated as in equation (3.20).

$$WR = (2\pi f)^2 \times m_s \tag{3.23}$$

Where: m_s=Sprung mass

2.Targeted Maximum displacement, x, at Peak Load

The maximum wheel displacement was related to the wheel Ratio as in equation. (3.24),

$$x(W.R) = CW + LLT + BS \tag{3.24}$$

Where CW is the Corner Weight, LLT is the Lateral Load Transfer and BS is the Bump Strike.

Because the Targeted Maximum Displacement (TMD) method typically yields a spring rate that is too stiff for passenger-vehicle targets, it was applied here only as a validation check

for the non-linear compliance elements introduced in Section 3.4.7. The spring rate derived from TMD defines the minimum combined stiffness that the bump-stop and progressive coil segment must provide once the primary spring approaches full compression.

3.5.2 Spring Material Selection

The materials' choices in this design were consistently determined by their characteristics versus required output and the difficulties related to manufacturing methods available for use. This study employed Dieter's (2013) material selection process for redesigning and improvement.

3.5.3 Spring Parameters Methods

1. **Wire Diameter (d):** The basic diameter of the wire used to make the coil spring. According to Hooke's Law, the force the spring can withstand is influenced by the spring's stiffness constant (k) which directly relates to the wire diameter. These relations are depicted in Equations (3.25-3.26)

$$F = kx \tag{3.25}$$

$$k = \frac{Gd^4}{8D^3n} \tag{3.26}$$

   Where d is the wire diameter, D is the mean coil diameter, n denotes number of Coils and G represents shear modulus of material

2. **Solid Length (L_s) and Free Length (L_f)**: Defined as the spring's overall length when all of the coils are completely compressed and stacked without any gaps and the spring's overall length when it is not loaded respectively (Hymanjali et al., 2018). Thus, making them crucial for analyzing and determining the spring's working range, preload needs and its load limits.

$$L_s \approx (n-1).d + (t_1 + t_2) \tag{3.27}$$

$$L_f \approx L_s + \delta_{max} + 0.15\delta_{max} \tag{3.28}$$

Where N denotes Total number of active coils in the spring, d is the diameter of the spring wire. t_1 and t_2 are the thicknesses of the spring's end coils

3. **Pitch (p):** The distance, measured along the spring's axis, between the centres of two neighbouring coils. It influences its performance mostly stiffness and behaviour under load. It was parametrically designed to ensure stiffness varies with load.

$$\boldsymbol{P \approx \frac{L_f}{n-1}} \tag{3.29}$$

3. Spring index (C): A dimensionless number that shows the proportion between the wire diameter (d) and the spring's mean diameter (D). It impacts the spring's strength, longevity, and behavior under load in addition to offering insight into the spring's geometry during the initial design stages. The Spring Index was given by;

$$C = \frac{D}{d} \tag{3.30}$$

An index between 4-12 is optimal (Vadhe, 2018).

4. Compression Travel (T): This refers to the distance that the spring travels under a specific weight and calculated by Equation 3.31 and aids in spring load forecasts.

$$T = \frac{L}{k} \tag{3.31}$$

Where L is the specific load (L) and K is the spring rate.

3.5.5 Stress Distribution Analysis

To determine the stress experienced by the spring under load, the following types of shear stress were calculated;

1. Torsion Shear Stress (τ_t): This stress arises due to the torsional force exerted on the spring. It was calculated using the formula:

$$\boldsymbol{\tau_t = \frac{8FD}{\pi d^3}} \tag{3.32}$$

Torsion shear stress aids in validating the wire diameter and spring material that handles torsional loads.

2. Direct Shear Stress (τd): Direct stress is caused by the axial force acting on the spring, it ensures the spring material can resist axial forces without deformation or failure and is determined as:

$$\boldsymbol{\tau_d = \frac{4F}{\pi d^2}} \tag{3.33}$$

Where F is the applied Force, which may vary depending on the load on the vehicle.

3. Resultant Shear Stress (τ): The total shear stress is the sum of torsion and direct shear stresses:

$$\tau = \tau_t + \tau_d \tag{3.34}$$

The resultant shear stress provides a comprehensive measure of the stresses acting on the spring, ensuring it operates safely under combined loading conditions from all directions.

3.5.6 Curvature Effect with Wahl's Correction Factor

Wahl's correction factor (K_w) was used to account for the additional stress brought on by the spring coils' curvature. It was computed as follows:

$$K_w = \frac{4C-1}{4C-4} + \frac{0.615}{C} \tag{3.35}$$

Where C is the spring index and the corrected maximum shear stress was then determined as:

$$\tau = K_w \frac{8FD}{\pi d^3} \tag{3.36}$$

Incorporating the curvature effect ensured the spring design reflects real-world stress distributions, preventing premature failure or fatigue.

3.5.7 Factor of Safety

The spring's ability to support loads over the specified operating parameters was assessed by the factor of safety, n_{fos}.

$$\boldsymbol{n_{fos} = \frac{\tau_{allow}}{\tau_{max}}} \quad (3.37)$$

Where τ_{allow} is the allowable stress, derived from the ultimate tensile strength divided by a material safety factor. A sufficient yield safety factor of above 1.3 ensures that the spring functions dependably without failing in potholed uneven roads (Jazar, n.d.).

3.5.8 Buckling Analysis

The slenderness ratio (λ) assesses the risk of buckling, which is a stability issue when the free length (L_f) is excessive compared to the mean diameter (D). For steel alloys, stability condition is satisfied if (Dixon, 2007);

$$L_f < 2.63\frac{D}{\lambda} \quad (3.38)$$

Where λ is determined by the spring's end condition its values are given in table 3.2 for different end conditions. Buckling analysis ensures the stability under compression, preventing catastrophic failure from instability under load.

Table 3. 2: Values of λ for different compression spring end conditions

End Conditions	$\boldsymbol{\lambda}$
Spring Between two flat parallel surfaces	0.5
Spring on one flat surface with another end hinged	0.707
Both ends pivoted	1
One end clamped and the other free	2

3.6 Objective Two: To develop a stable damper to reduce the impact of bumps and vibrations

The damper system design involved considering damping mechanisms to absorb or dissipate energy and reduce oscillations or vibrations in the shock absorber system.

3.6.1 Damper Physical Parameters

The shock absorber was sized so that its force-velocity curve both delivers the damping ratio required for passenger car (response tune) ride quality and survives the 180mm worst case pothole defined in Section 3.4. The procedure was analytical and precedes any valve work or CFD work

Target damping ratio: The wheel-side damping ratio, ς was selected from Ślaski's passenger-car (response tune) band (0.30-0.50) as shown in Table 3.3. A mid-value is imposed on the critical wheel damping

$$C_{cr} = 2 \times \sqrt{WR \times m_s} \quad (3.39)$$

$$\varsigma, = \frac{C_w}{C_{cr}} \quad (3.40)$$

Because the MacPherson motion ratio is ≈ 1, the damper coefficient becomes

$$C_d = C_w(MR)^2 \quad (3.41)$$

Table 3. 3: Characterization of Damping Coefficient for Different Vehicle Categories. (Ślaski, 2011)

Car Type	Damping Coefficient
Passenger car (comfort tune)	0.20-0.30
Passenger car (Response tune)	0.30-0.50
Race car	0.60-1
Heavy Truck	3-7

Damping Force and Peak Velocity: The highest relevant damper speed was taken as the linear product of sprung mass natural frequency and peak wheel deflection (energy approach avoids over-conservatism in this method).

$$v_{max} = \omega . x_{max} , \omega = \sqrt{k/m} \quad (3.42)$$

And here it is assumed that *a* small-angle pitch/roll is neglected so vertical and longitudinal motions decouple and the tyre enveloping action is handled in section 3.4 and not re-

introduced here. And thus, the damping force F_d that the valving must supply at v_{max} is obtained via equation

$$\boldsymbol{F_d = C_d . v_{max}} \quad (3.43)$$

Piston diameter: With a monotube design pressure P fixed by the gas charge, the piston diameter and corresponding cross section Area (Ap) ensuring F_d was as in equation (3.44).

$$D_p = \sqrt{\frac{4F_d}{\pi P}}, A_p = \frac{\pi D_p^2}{4} \quad (3.44)$$

Rod diameter and effective area.: Following EUSAMA guidance, the rod diameter was chosen as 40-50% of Dp. With Dr=αDp, (where α=0.45 in the present design). The corresponding effective Area, A_e, can be obtained as in equation (3.45).

$$\boldsymbol{A_e = A_p - A_r} \quad (3.45)$$

Where A_r is the piston rod cross section area.

3.6.2 Damper-Stroke Sizing

With the coil spring rate k determined and wheel-side damping coefficient C_d known (see Sections 3.4 and 3.6.1). A worst-case wheel drop into a pothole is modelled as a one-shot exchange of kinetic and potential energy into spring compression and hydraulic work. The optimal shock stroke requirement is derived analytically using the principles of energy conservation and vehicle dynamics.

Impact energy at the wheel: For a wheel that descends through a pothole of depth (h), while travelling at speed, v, the available energy at the instant it contacts the far edge is as in equation

$$E_{input} = mgh + \frac{1}{2}mv^2 \quad (3.46)$$

where m_s is the sprung mass, h the pothole depth, and v the approach speed.

Estimating the Sink speed: The average downward velocity of the wheel centre is approximated from bump geometry

$$v_{sink} = \frac{h}{L} v \tag{3.47}$$

where L is the longitudinal footprint of the pothole. This simplifies the transient to a single design speed for the damper piston.

Energy absorbed by spring and damper: Energy is dissipated in two parallel paths, spring compression and damper work. With a shock efficiency (η) the absorbed energy is

$$E_{absorbed} = \eta(\frac{1}{2} kx^2 + F_d x) \; ; \; F_d = C_d . v_{sink} \tag{3.48}$$

where x is the stroke required to store/dissipate the event energy.

Solve for theoretical stroke using conservation of energy principal: Equating input and absorbed energy gives

$$mgh + \frac{1}{2} mv^2 = \eta(\frac{1}{2} kx^2 + F_d x) \tag{3.49}$$

Solving this quadratic yields the theoretical minimum x

Safety Considerations: To accommodate speed scatter, payload shifts, tyre-pressure variation and manufacturing tolerances, a safety allowance is appended:

$$s_{design} = x + safety\ Margin \tag{3.50}$$

The stroke length obtained should be less or equal to suspension travel considered during the Coil Spring design so that the damper never reaches hydraulic lock before the bump-stop engages, preserving the full working travel derived in the coil-spring study.

3.6.3 Floating-Piston Mass Calculation

In this step, the floating piston was defined as a thin-walled, hollow cylindrical disc whose envelope is set by the damper bore and available package height. All non-geometric parameters are drawn from design data and literature: steel density (ρ) and yield strength (σ

), bore diameter (D_o), seal-groove depth (h_c), and design gas pressure (P). The only free variable is the radial wall thickness (t). Inner radius is computed as equation (3.51).

$$\boldsymbol{R_i = \frac{D_o}{2} - t} \quad (3.51)$$

Effective piston height and volume

The piston is relieved on its gas side over the seal-groove depth h_c, leaving a solid height, H_{eff} and material volume as calculated as in equation (3.52)

$$\boldsymbol{V = \pi(R_o^2 - R_i^2)H_{eff}, H_{eff} = H - h_c} \quad (3.52)$$

where H is the total piston height dictated by the damper package envelope.

Converting Volume to mass

$$\boldsymbol{m = \rho V} \quad (3.53)$$

Verifying structural integrity

Hoop stress in the piston wall under internal pressure p was estimated via the thin-ring formula:

$$\boldsymbol{\sigma_h = \frac{\rho R_i}{t}} \quad (3.54)$$

To ensure a safe design margin against yield, require, $\sigma_h \leq 0.1\sigma_y$, σ_y being the material's yield strength, a margin that accounts for stress concentrations at the seal groove and transient pressure spikes. When these criteria are satisfied, the mass is finalized and discussed in the results

3.6.4 Gas Chamber Pressure-Volume Sizing

Using the ideal gas law and the force equilibrium diagram Figure 3.2 on the floating piston enabled to ascertain the initial gas pressure in the gas chamber, P_{gi}. Boyle's Law governs the operation of the gas chamber, so the initial pressure is intrinsically related to changes in

volume. The equation (3.52) shows the gas chamber pressure at any given moment, P_g, relies on its volume.

Considering Force Equilibrium in the Floating Piston,

$$\boldsymbol{P_{gi} = P_g \frac{V_g}{V_{gi}}} \quad (3.55)$$

where V_g = current volume of the gas chamber and V_{gi} indicates the initial volume before compression. The volume of the gas chamber can be determined using the area of the floating piston, as illustrated in equation (3.56) and (3.57).

$$\boldsymbol{V_g = A_p L_g} \quad (3.56)$$

$$\boldsymbol{V_{gi} = A_p L_{gi}} \quad (3.57)$$

In this setting, A_p represents the area of the floating piston, L_{gi} and L_g denote the initial length of the gas chamber and Gas chamber length after piston displacement respectively. Substituting these expressions into the equation (3.55), the initial pressure is given by;

$$\boldsymbol{P_{gi} = P_g \frac{A_p L_g}{A_p L_{gi}}} \quad (3.58)$$

The force equilibrium on the floating piston provides an alternative approach to determine P_g. The floating piston is influenced by the gas pressure, P_g, on one side and the compression chamber pressure, P_c, on the opposite side.

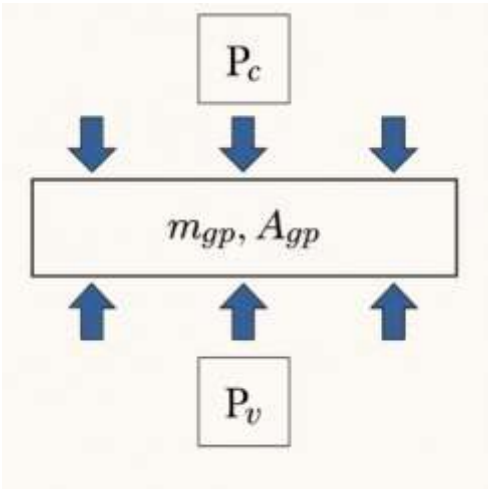

Figure 3.5: Force Equilibrium Diagram of Compression and Gas Chambers

The pressure from friction against the walls and the weight of the piston significantly influence its behaviour. Figure 3.5 presents a simple piston force diagram.

The force balance equation can be expressed as follows:

$$P_g A_{fp} = P_c A_{fp} + m_{fp} g + f_f sing(\dot{x}) \quad (3.59)$$

This study assumed that $f_f sing(\dot{x})$ is negligible and was disregarded in the numerical analysis. The equation can be rearranged to express

$$\boldsymbol{P_g = P_c + m_{fp} g + \frac{m_{fp} g}{A_{fp}}} \quad (3.60)$$

By substituting equation (3.60) into the equation (3.58) for initial pressure, we derive, $P_{gi,}$

$$\boldsymbol{P_{gi} = \left(P_c + m_{fp} g + \frac{m_{fp} g}{A_{fp}}\right) \frac{A_p L_g}{A_p L_{gi}}} \quad (3.61)$$

This equation demonstrates that the initial gas pressure is affected by the gas chamber volume, the pressure within the compression chamber, and the mass of the floating piston. Consequently, without any external force, the initial gas pressure is exclusively influenced by variations in volume within the gas chamber and this was used in determining pressures and volumes used in this damper.

3.6.5 Orifice Flow Rates and Valve Arrangements

The damper's valve-train must translate vehicle level force targets into a matched set of hydraulic passages and mechanical shims. The methodology proceeds in two linked stages. Section 3.6.5.1 formulates the hydraulic sizing rules that predicts bleed area, piston-port diameter and clamping radius directly from the comfort and impact velocity requirements. Section 3.6.5.2 develops a four-shim mechanical model that uses predicted hydraulic boundaries to generate plate thickness, hole pattern and lift estimates. Together, these sections close the loop from global performance objectives to a manufacturable piston assembly.

3.6.5.1 Hydraulic Valve-Train Sizing

This subsection identified the flow areas and pressures that the piston assembly must accommodate before any shim geometry is chosen. Calculations rely on mass continuity and the ISO 5167 sharp-orifice equation (3.62)

$$\boldsymbol{Q = C_d A\sqrt{\frac{2\Delta P}{\rho}}} \tag{3.62}$$

Where Q represents the flow rate of a fluid through an orifice, C_d denotes Discharge coefficient (dimensionless), A is the Area of the orifice or flow passage (m^2), ΔP represents Pressure difference across the orifice (Pa) and ρ is the Fluid density (kg/m^3)

Bleed-Needle Formulation

The bleed needle establishes the low-speed slope by metering 100% of the oil flow while the shim stack is closed.

1. Continuity at the comfort velocity: The volume displaced by the piston each second was computed using equation (3.63)

$$\boldsymbol{Q_{LS} = v_{LS} A_e} \tag{3.63}$$

where v_{LS} is the reference comfort shaft speed and A_e the hydraulic piston area.

2. Pressure drop that produces the comfort force: The required oil pressure is linked to the desired damper force by

$$\boldsymbol{\Delta P_{LS} = \frac{F_{LS}}{A_e}} \tag{3.64}$$

3. Area of the annular passage opened by a conical needle: A conical needle ground to a 60° included angle ($\theta=30^0$) forms an annulus whose flow area was calculated by

$$\boldsymbol{A_{annulus} = \pi d \frac{L}{\sin\theta}} \tag{3.65}$$

with d is the seat diameter and L the axial lift.

4. Orifice-flow relation for turbulent discharge: Volumetric flow through the annulus obeys the volumetric equation (3.66)

$$\boldsymbol{Q_{LS} = C_d A_{annulus} \sqrt{\frac{2\Delta P_{LS}}{\rho}}} \quad (3.66)$$

where C_d is the discharge coefficient for a sharp-edged seat and ρ the bulk oil density.

5. Initial lift setting: Combining the two preceding expressions (3.66) and (3.65) gives the needle lift that satisfies both continuity and pressure criteria as shown in equation (3.67).

$$\boldsymbol{L = \frac{Q_{LS} \sin\theta}{C_d \pi d} \sqrt{\frac{\rho}{2\Delta P_{LS}}}} \quad (3.67)$$

Once a practical seat diameter is chosen, this equation yields the mm of initial back-off; a fine-pitch adjuster screw is specified so that one quarter-turn changes L by roughly 0.1mm, providing ample tuning resolution.

Piston-Port Formulation

When shaft velocity rises, at high impacts, a fixed fraction of the displaced flow must bypass the bleed and pass the piston ports. Port diameter is therefore sized from the residual flow and the force-derived pressure drop as steps below;

1. Continuity at the impact velocity

$$\boldsymbol{Q_P = v_{HS} A_e} \quad (3.68)$$

with v_{HS} is the impact shaft velocity characterising severe road inputs such as those exhibited on potholed uneven roads

2. Share of flow allocated to the piston valve

A small fraction ϕ (typically 10-20%) of the total flow continues through the bleed at high speed, leaving for the piston-valve orifices.

$$\boldsymbol{Q_v = (1 - \phi)} \quad (3.69)$$

3. Flow per individual orifice

Distributing Q_v over n_o equally sized ports gives the number of orifices Q_o.

$$\boldsymbol{Q_o = \frac{Q_v}{n_o}} \tag{3.70}$$

4. Pressure drop defined by the peak-force requirement

$$\boldsymbol{\Delta P_{HS} = \frac{F_{HS}}{A_e}} \tag{3.71}$$

where F_{HS} is the target maximum damper force.

5. Port diameter derived from the orifice equation

With $A_O = \pi d_0^2/4$ and the standard discharge relation, port diameter can be determined as in equation (3.72).

$$\boldsymbol{d_O = 2\sqrt{\frac{Q_O}{C_d \pi}\sqrt{\frac{\rho}{2\Delta P_{HS}}}}} \tag{3.72}$$

The same drill size was kept on rebound and compression faces to simplify manufacturing; the chosen number of ports should ensure a Reynolds number above 10^4 while maintaining sufficient ligament width between holes.

Clamping Radius $\underline{r_c}$

The clamping radius controls the free span of every shim and therefore the initial stiffness of the entire stack. The clamping radius was typically chose based on industry standards and practical design considerations prescribe 0.5-0.6 of shim diameter for comfort ride (Skačkauskas et al., 2017).

After r_c is fixed, it is held constant in all Talbott–Starkey lift calculations and in the port-diameter sizing, ensuring that hydraulic and structural models remain mutually consistent throughout the design process.

3.6.5.2 Shim Stack Model

This study regulates rebound and compression forces with a four-leaf shim stack: nested spring steel discs clamped at the inner radius and free at the outer, so that pressure on one face lifts the outer leaf to form a circumferential flow gap that recloses on the return stroke. The bending stiffness of a circular plate is proportional to the cube of its thickness (t^3) and the fourth power of its free radius (r^4); thus, careful selection of t_i and r_i allows for the design to be optimised for both the opening pressure and the diminishing slope of the force-velocity curve. Stack compliance is predicted with the linear, small-deflection plate formulation of Talbott & Starkey (2002), itself based on the Kirchhoff-Love solution for a uniformly loaded, clamped free disc summarised by Young and Budynas (2002). Provided edge deflection remains below plate thickness (typically $y/t<1$), the model remains linear and the superposition principle permits the total compliance to be expressed as the sum of the reciprocals of the individual flexural rigidities. Coupling this plate model with ISO 5167 orifice flow relations for the bleed and piston ports yields an iterative framework that simultaneously satisfies low-speed comfort and high-speed impact force targets without recourse to empirical trial-and-error.

Geometry, Material and Notation involved:

All shims share the outer seat radius r_o (governed by the piston-port circle) and the inner clamp radius r_c. Only two variables change from shim to shim;

Plate thickness t_i $(i = 1 \text{ is the outermost leaf})$,

Bleed-hole set $(n_i, d_{h,i})$ $(number\ and\ Diameter)$

Material constants included Young's modulus E, Poisson's ratio, ν and yield strength σ_y that correspond to spring-steel shims at operating oil temperature; oil density ρ and a sharp-edged discharge coefficient C_d are taken from the fluid data sheet.

Effect of Perforations on Flexural Rigidity

Each shim's solid-plate flexural rigidity is as shown in equation (3.73)

$$\boldsymbol{D_i = \frac{E t_i^3}{12(1-\nu^2)}} \tag{3.73}$$

Holes remove material and weaken the plate; the effect is captured with a ligament efficiency factor, α, as shown in equation (3.74).

$$\boldsymbol{\alpha_{h,i} = 1 - \frac{n_i \pi d_{h,i}^2/4}{\pi(r_o^2 - r_c^2)}, D_{i,eff} = \alpha_{h,i} D_i} \tag{3.74}$$

A leaf with no holes has $\alpha_{h,}$ =1; one whose net metal area is 80 % of full area has $\alpha_{h,}$ =1.

Predicting Stack Lift under Uniform Pressure

Talbott & Starkey's series compliance model treats the stack as four parallel-loaded plates. For a given pressure ΔP the outer-edge gap is given by equation (3.75).

$$\boldsymbol{\mathcal{Y}(\Delta P) = \frac{\Delta P(r_o^4 - r_c^4)}{64} \sum_{i=1}^{4} \frac{1}{D_{i,eff}}} \tag{3.75}$$

Because $D_{i,eff} \propto t_i^3$, modest changes in thickness (±0.05mm) strongly influence $\mathcal{Y}$. With assistance of these models, the steps below yield an optimal shim stack model for the damper;

1. Bleed-Hole Sizing for Low-Speed Damping: When the stack is closed, every drop of oil must pass the bleed holes. For turbulent flow, the required total open area A_h follows the orifice equation (3.76);

$$\boldsymbol{A_h = \frac{Q_{LS}}{C_d\sqrt{2\Delta P_{LS}/\rho}}, A_h = \sum_{i=1}^{4} n_i \frac{\pi d_{h,i}^2}{4}} \tag{3.76}$$

The design selects integer hole counts and standard drill diameters so that as a rule, most or all of A_h is placed in the outermost shim so the bleed path is uninterrupted while deeper leaves remain clamped.

2. Flow Balance at the High Speed: At v_{HS} oil splits between the bleed holes and the annular edge gap created by y. The required pressure drop must satisfy the relation in (3.77).

$$Q_{HS} = C_d A_h \sqrt{\frac{2\Delta P}{\rho}} + C_d (2\pi r_o Y(\Delta P)) \sqrt{\frac{2\Delta P}{\rho}} \quad (3.77)$$

Because y is itself a function of ΔP, Equation (3.77) is implicit; a spreadsheet or Newton–Raphson routine converges rapidly to the ΔP that satisfies the flow target.

3. Structural Integrity Checks: After each iteration the candidate stack must pass three durability criteria:

Lift limit

$Y_{max} \leq t_{min}$, keeping deflection within the linear plate regime.

Peak bending stress

$$\boldsymbol{\sigma_{max} \approx \frac{3\Delta P_{HS} r_0^2}{2t_{min}^2} K_t \leq \frac{\sigma_y}{SF}} \quad (3.78)$$

where K_T (1.2-2.0) allows for hole-edge concentration and SF (≥1.3) is the chosen safety factor.

Fatigue margin: Verify the alternating stress is below the endurance limit of the spring steel. If any limit is breached, the designer increases t_i reduces hole size/count and repeats the process.

3.6.5.3 Iterative Tuning Strategy

After the first analytical pass the valve often needs minor adjustments to reconcile bench-measured forces with design targets or to compensate for manufacturing scatter. Table 3.4 lists the most appropriate performance deviations observed during simulation or dynamometer/road testing and the corresponding design levers that correct them.

Table 3. 4 : Damper Simulation observations and appropriate corrective action.

Observation	Corrective action
Low-speed force too high	Increase A_h (add or enlarge holes)
Low-speed force too low	Reduce A_h (plug or downsize holes)
High-speed force too high	Reduce stack stiffness: thin outer shim, add holes, or enlarge r_c
High-speed force too low	Increase stiffness: thicken inner shims, delete holes, or shrink r_c
Stress or lift over limit	Thicken offending shim or relocate holes toward low-stress region

Two to four iterations normally suffice

3.6.5.4 Shim Method Validation

The four-step analytical chain ISO 5167 orifice flow, Kirchhoff–Love plate rigidity, Talbott-Starkey stack superposition and the coupled flow lift relation, has been shown in published work to predict monotube damper forces to within roughly ±10% of rig measurements. Because every equation is closed form or one-dimensional, a complete valve sizing can be carried out in a spreadsheet, eliminating the trial-and-error loops noted by Dixon (2007). Final shim dimensions are nevertheless confirmed in a simulation pass or later on a dyno, and any residual error is removed with the appropriate adjustment before the design is frozen for production.

3.6.6 Material Selection and Optimization

As used in the first objective, Dieters (2013) methods of material selection were used for the damper cylinder. However other parts i.e., Piston, Shims, Rod etc., available literature was used to qualitatively select the optimal material as per already existing data.

3.7: Objective Three: To conduct CAD simulations to optimize shock absorber performance and validate the effectiveness

3.7.1 Detailed 3D CAD Modeling

A detailed 3D CAD model of the re-designed shock absorber system parts and assembly was developed using solid works design software because of its advanced 3D assembly features

and enhanced capabilities in motion and kinematic analysis, structural and fluid analysis as well as documentation in form of generating drawings. considering all the key dimensions and parameters for the respective components as obtained in objective 1 and 2. Each of the components was modelled using Solid works and then an assembly of the entire shock absorber system created. The model was created with a flexible and adaptable design framework to allow iterative refinement and optimization during the simulation process to help in attaining the performance feedback.

The model also included the respective selected materials for the components, and this was done according to the mechanical properties like strength, stiffness, and fatigue and corrosion resistance.

3.7.2 Simulation Setup and Boundary Conditions

In this study, the CAD model was first divided into finite elements to provide a computational mesh for FEA simulations. The mesh density of 95% and above was accurately planned to optimise simulation accuracy and computing performance. To approximate to real word simulations, automatic mesh refining and element quality optimisation have been utilised.

Realistic boundary conditions set included operational temperatures, load assessments in kgf, spring characteristics, and damper specifications and these were simulation inputs and controls. Restrictions were placed on mounting points and interfaces, while external stresses simulating vehicle dynamics and road inputs were applied to replicate realistic loading conditions.

3.7.3 Simulation Analysis and Optimization

Static and Dynamic analysis was carried with the aid of FEA software in order to simulate the shock absorber assembly’s transient response to external loads and driving conditions.

The key performance metrics like displacement, velocity, acceleration, and damping characteristics over time were also evaluated from the simulation reports.

The Simulation results obtained were analyzed to identify areas for performance optimization and parameter improvement. And this enabled to rectify errors that might have been done during numerical design models in objective 1 & 2. Design parameters such as component geometry, material selection, and damping characteristics were iteratively adjusted to ensure better shock absorber performance outcomes, including ride comfort, stability, and energy dissipation abilities.

3.7.4 Damper Simulation via ShimRestackor Pro.

Unlike Solid works, ShimRestackor Pro has embeded fundamental physics principle that enables advanced cavitation analysis with a high degree of accuracy as well as integrating complex viscosity effects and is therefore regarded as a special simulation tool for dampers, the methodology as illustrated in Figure 3.6 were used to carry out dynamic simulations of the damper that would rather be difficult to achieve with Solid works.

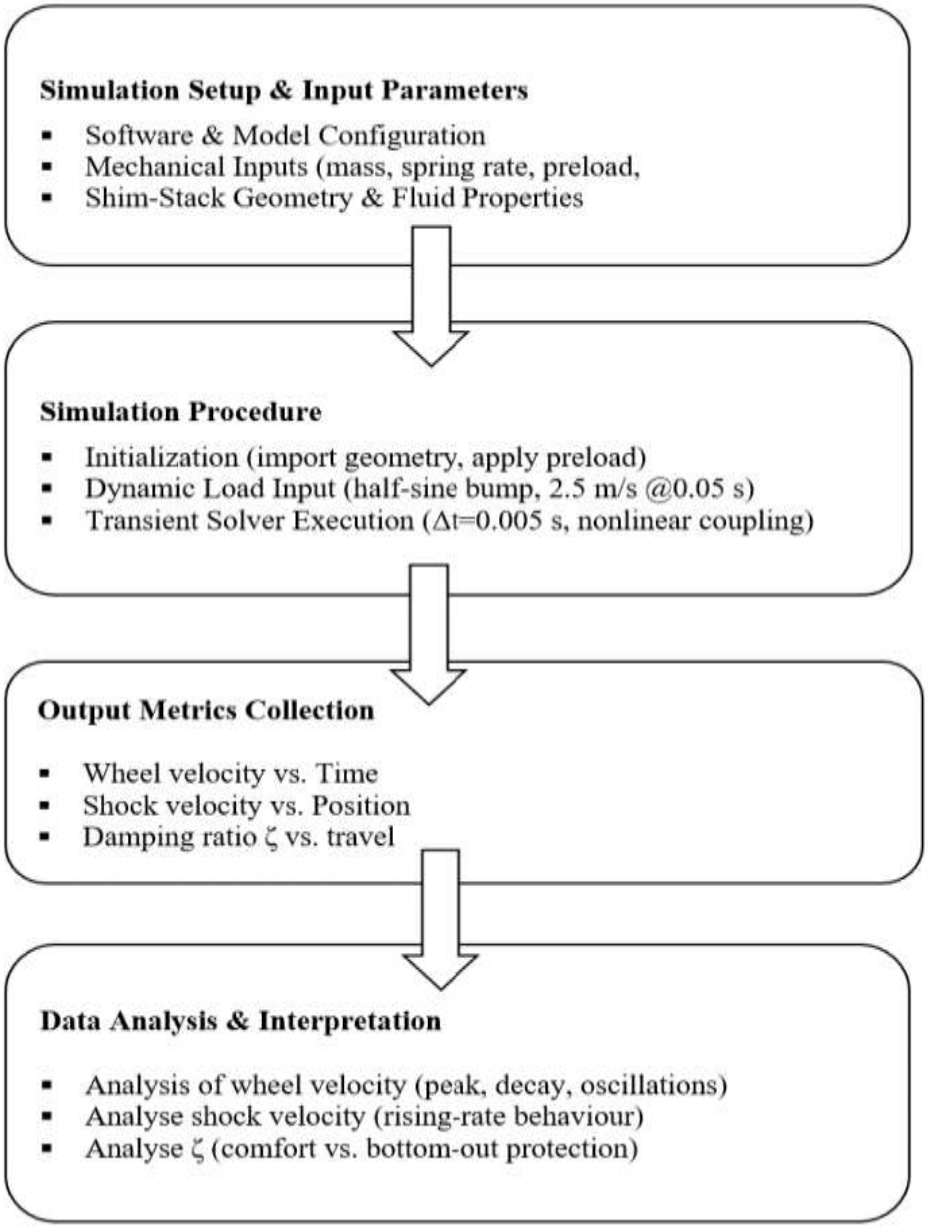

Figure 3. 6: ShimRestackor Pro Methodology Set up

3.8 Objective Four: Assess the technical requirements for manufacture of the designed shock-absorber system within Uganda.

The methodology for assessing manufacturability in this study was carried out in four sequential stages as explained.

Process Selection & Equipment Capability Evaluation: Desk searches were used to identify every manufacturing process required for the shock absorber system components

designed and match each to locally available capacity. Capability checks covered tolerance bands, cycle time, energy demand, and existing expertise. Only processes that can meet the design's specifications at the planned volumes was selected.

DFMA Analysis & Production-Line Layout: Desk searches were used to find out the Design-for-Manufacture and Assembly (DFMA) principles and best practices that can lower part count and assembly time. The resulting process sequence was mapped onto a preliminary line layout that minimises material handling distances and balances workload evenly across stations.

Cost Modelling & Economies-of-Scale Analysis: Each operation's fixed (CAPEX) and variable costs (labour, energy, consumables) were determined through review of literature from other manufacturers publications. These were combined in a costing model to determine unit cost. By varying annual volume, the model expected to reveal break-even points for in-house versus outsourced processes, optimal batch sizes, and the sensitivity of unit cost to labour rate. This facilitated on analyzing make/buy and automation decisions.

Integrated Plant Layout & Workflow Design: The validated process map and cost model was folded into a complete factory floorplan that positions machines, buffers, quality gates, and logistics aisles in accordance to ISO 10628 and ISO 12100. Material handling routes, Kanban loops, and safety clearances were overlapped to produce a coherent workflow, ready for detailed facility engineering and production.

3.9 Summary of Methodology

This methodology details a technically viable pathway for developing, validating, and producing a shock absorber system tailored for pot holed uneven roads. By anchoring every calculation to a chosen worst-case pothole scenario and a 2-DOF quarter-car model, we were able to derive traceable spring and damper parameters, incorporate non-linear safeguards for

extreme events, and confirm structural integrity through CAD-based FEA and specialized shim stack simulations. A four-stage manufacturability assessment was adopted to demonstrate that the system can be built economically using domestic capabilities or an import-local hybrid supply chain. The result is a defensible, performance optimized shock absorber ready to interface Uganda's road conditions and industrial context.

CHAPTER FOUR: DISCUSSION OF RESULTS

4.1 Introduction

In this section, the damper was designed to function in harmony with the coil spring as well as its local manufacturability predicted. This aimed to find the ideal balance between ride comfort and handling performance fit for un-even road situations. By selecting the suitable materials, the discussion focused on choosing the spring rate (k), enhancing damping properties (Fd-V curves), that included tailoring the redesign to potholed uneven roads. The results obtained correlated with pothole scenario foundation parameters projected in chapter three, Section 3.4.

4.2 Objective One: To Determine the Light vehicle shock coil spring parameters for optimal performance on uneven roads

4.2.1 Coil Spring Load Estimates

Building on the mass partitioning established in Section 3.4.3 and Appendix A.2, the quarter-car model (illustrated in Figure 3.2) assigns a sprung mass of 379.31kg and an unsprung mass of 67kg. This yields an unsprung to supported-mass ratio of 0.15, within the 10-15% band recommended by SAE for passenger vehicles, a range that minimises wheel road separation on potholed uneven roads and preserves lateral stability under cornering loads (Vadhe 2018; Tang 2014).

4.2.2 Spring-Rate Results and Interpretation

Considering a 1.5Hz natural frequency based on the need to balance both ride comfort and handling performance with Motion Ratio of 1 as it is a Macpherson Suspension design. The spring rates is determined from Equation (3.22) and (3.23)

$$WR = (2 \times 3.14159 \times 1.5)^2 \times 379.31 = 33{,}692.76Nm \quad (4.1)$$

$$K = 33{,}692.76 \times (1)^2 = 33{,}692.76Nm \quad (4.2)$$

By contrast, the displacement-limited method using desired maximum displacement (δ_{max}) as in Equation (3.24), the resulting Spring stiffness was 51.1kN/m.

$$CW = m_s . g \tag{4. 3}$$

$$= 379.31 \times 9.81 = 3{,}722.10\text{N}$$

$$\boldsymbol{LLT} = \frac{\boldsymbol{m \times h \times A_y}}{\boldsymbol{t}} \tag{4. 4}$$

$$= \frac{379.31 \times 0.5 \times 0.2\text{g}}{1.695} = 219.54\text{N}$$

$$\boldsymbol{BS = SNM \times MVA} \tag{4. 5}$$

$$= 379.31 \times 9.81 = 3{,}721.10\text{N}$$

Thus,

$$0.15 \text{ x W. R} = 3721.10 + 219.54 + 3721.10$$

$$\text{W. R} = 51{,}078\text{N/m}$$

Where SNM is Static Nominal Mass and MVA is the Maximum Vertical Acceleration

Interpretation.

The natural frequency (NF) value prioritises ride comfort, placing the sprung mode in the 1.2-1.5Hz docket for MPVs regardless of the applicability, whereas the displacement method embeds worst-case dynamic loads, demanding a stiffer rate for stability during severe manoeuvres. In practice the NF based rate (33.7 kN/m) is adopted for the primary coil spring to preserve vibration isolation, while the higher maximum displacement-based rate (≈51kN/m) defines the minimum combined stiffness of the progressive coil wind-up plus bump-stop in this design. This dual criterion approach balances comfort with ultimate load capacity and the pothole roads as well as informing the bump-stop specification.

4.2.3 Coil Spring Material Selection

Following Dieter 2013, material selection methodology, frequently utilized materials in coil spring design were selected for comparison and these included Carbon Steel, Structural Steel, Chromium Silicon (Cr-Si), and Chromium Vanadium (Cr-V).(Konieczny et al., 2016). These materials are assessed according to their mechanical qualities, manufacturability, cost, and availability.

Critical properties considered are tensile strength, fatigue life, elongation, and corrosion resistance as these are essential in assessing their appropriateness for coil spring applications(Sanghavi et al., 2007). Practical factors; cost-effectiveness and sourcing convenience are incorporated into the selection process to conform to manufacturing limitations and market requirements. Table 4.1 shows the properties of the selected materials included in screening,

Table 4.1: Baseline properties of the design candidate spring materials

Property	Carbon Steel	Structural Steel	Chromium Silicon (Cr-Si)	Chromium Vanadium (Cr-V)
Tensile Strength (MPa)	600-800	400-600	1350-1500	Up to 1400
Fatigue Life (cycles)	$\sim 10^5$	10^5-10^6	$\sim 10^7$	$\sim 10^7$ and above
Elongation (%)	12-16	10-15	18-22	20-25
Corrosion Resistance	Low	Low	Moderate	High
Cost (Relative)	Low	Low	High	Medium

Each material is evaluated using weighted property scores to enable an objective comparison. Tensile strength (0.25) and fatigue life (0.25) are credited more importance due to their essential contribution to the coil spring's long-term reliability. Elongation (0.15) and corrosion resistance (0.15) are significant factors, as they affect the material's capacity to endure climatic conditions and mechanical stress. Cost (0.1) and availability (0.1) are incorporated to guarantee that the chosen material remains economically feasible and

accessible for mass manufacturing. Each property of every alloy was normalised on a 1-5 scale, multiplied by its weight, and summed. The resulting tallies appear in Table 4.2.

Table 4. 2: Weighted Decision Matrix for Spring

Property	**Weight**	**Carbon Steel**	**Structural Steel**	**Chromium Silicon (Cr-Si)**	**Chromium Vanadium (Cr-V)**
Tensile Strength	0.25	2	1	5	4
Fatigue Life	0.25	2	3	4	5
Elongation	0.15	3	2	4	5
Corrosion Resistance	0.15	1	1	3	5
Cost	0.1	5	5	2	3
Availability	0.1	5	5	3	3
Total Score	**1**	**2.45**	**2.3**	**3.75**	**4.3**

Cr-V achieves the highest composite score of 4.3. Its 1400 MPa ultimate strength and above 10^7 cycle endurance comfortably exceed the 405 MPa working shear calculated in Section 4.2.5, securing an FoS of 1.6 with generous fatigue margin. Superior corrosion resistance meets the splash and mud environment of Ugandan roads, while medium pricing keeps wire cost roughly 20% below that of Cr-Si the immediate substitute. On balance, Cr-V offers the most favourable combination of mechanical robustness, environmental durability, and economic viability, and is therefore adopted as the production wire for the coil-spring design.

4.2.4 Discussion of Spring Sizing Results

Iterative substitution of an initial mean coil diameter as 127.6mm and wire diameter as 14.4mm into the helical spring relation, equation (3.26), converged on 6 active coils, giving a spring index 8.9 that is towards the upper end of the 4-12 manufacturability band, a deliberate choice to favour durability on uneven potholed roads.

With the final rate of 33.7kN/m, the calculated wheel centre deflections are 93mm at curb mass (3144N) and 110mm at gross mass (3721N), both way above the 57mm minimum

compression travel the coil spring under 180mm pothole worst case scenario derived from the quarter-car model, leaving enough margin for dynamic excursions. The spring solid length of 101mm and free length of 342mm produce a nominal pitch 68mm, ensuring that, even at full gross-weight compression, the coils clear one another by approximately 10mm before the bump-stop engages.

Overall, the geometry satisfies load, travel, and manufacturability targets while providing the stiffness baseline used to set the minimum bump-stop parameter.

4.2.5 Coil-Spring Stress Results and Interpretation

Under the gross weight corner load of 3721N, the spring experienced a torsional component of 406MPa and a direct component of 23MPa, derived using equation (3.32) and (3.33) respectively, giving an uncorrected resultant shear stress of 429MPa. Incorporating curvature via Wahl's factor, K_w=1.16, reduced the peak to about 405MPa.

The wire is chromium–vanadium (Cr-V) spring steel with a typical ultimate tensile strength of roughly 1273MPa;

Applying a Cr-V typical material safety factor of 2.0 yielded an allowable shear of 636MPa. The resulting factor of safety

$$\boldsymbol{n_{fos} = \frac{\tau_{allow}}{\tau_{max}} = \frac{636}{405} = 1.57} \qquad (4.6)$$

Yield factor of safety 1.57 falls squarely inside the 1.2–2.0 range recommended for automotive suspension springs, confirming adequate strength with fatigue margin.

Reaching solid height would demand 7214N (about 735kg on a single front wheel), a load far beyond any realistic corner weight for the Toyota Wish platform; in practice the spring will never bind. Instead, the bump-stop engages first, protecting the coils while the calculated Cr-V wire stresses demonstrate that the chosen geometry provides both durability and compliance for the 180 mm worst-case pothole event.

4.2.6 Buckling Check and Design Validation

Buckling susceptibility was evaluated with the classic slenderness ratio criterion,

$L_f < 2.63\frac{D}{\lambda}$, where λ depends on end support. For a spring clamped between two parallel seats (λ=0.5; see Table 3.2) the critical free length is

$$\boldsymbol{L_{fcritical} = 2.63\frac{0.1276}{0.5} = 0.671m} \quad (4.7)$$

The designed free length is of 342mm, was barely half the critical value, 671mm. Hence the spring is well inside the stable regime and lateral bowing is not expected under either curb or gross weight loads.

Coupled with the previously calculated peak shear stress of 479MPa and deflections of 82 mm (curb) and 110 mm (gross), the buckling result confirms geometric sufficiency. These findings are further cross-checked in Section 4.4 via simulations, where the 3D model is subjected to the same loads to verify that neither excessive stress nor Euler instability arises in service.

Table 4. 3: Summary of Designed Coil Spring Parameters

Parameter	**Final value**
Spring Rate, k	33.7 ×10³N/m
Wire diameter, d	14.4mm
Mean coil diameter, D	127.6mm
Spring index, C	8.9
Active coils	6turns
Free length, L_f	342mm
Solid length, L_s	101mm
Nominal pitch	68mm
Load to solid height	7 214N
Corrected peak shear stress	405MPa
Material allowable shear	636MPa
Factor of safety	1.57
Buckling criterion	0.51
Wire material	Cr-V

4.3 Objective Two: To Develop a stable damper to reduce the impact of bumps and vibrations

Although shock absorber system design is governed mainly by the coil spring, a matched damper is indispensable for dissipating the spring's stored energy. The redesign therefore limited itself to valving, piston-area, and fluid-viscosity adjustments that yield a $\zeta \approx 0.40$ body mode and a digressive force velocity curve topping at 3.1kN near 0.3m/s, values that neither under damp body motions nor transmit harsh impact loads. By aligning these damping coefficients with the spring's deflection envelope (δ_{max}= 57mm) the system achieves high-damping force during pothole strikes while preserving low-speed comfort, thereby meeting the dual objectives of vibration reduction and dynamic stability on Uganda's uneven potholed roads.

4.3.1 Damper Material Selection

Durability, efficiency, and economic viability all depend on the material chosen for damper components. Following the Dieter (2013) weighted-property method used earlier, three common tube alloys; AISI 1018 carbon steel, 6061-T6 aluminium, and 304 stainless (Konieczny et al., 2016). These steels were scored against six criteria i.e., tensile strength, yield strength, corrosion resistance, fatigue resistance, machinability, and cost. The Tensile (0.25) and Yield (0.2) strength metrics and corrosion resistance (0.2) together carry 0.65 of the weight because the cylinder must contain repetitive high-pressure damping loads while surviving road-spray corrosion; machinability and cost ensure manufacturability within Ugandan workshop economics. Table 4.4 indicates the material properties and their corresponding weighted scores following Dietor 2013 material selection procedure.

Table 4. 4:Weighted scores of selected Damper cylinder materials

Property	**Weight**	**AISI1018 Carbon Steel**	**6061-T6 Aluminium Alloy**	**304 Stainless Steel**
Tensile Strength (MPa)	0.25	440 (Score: 4)	310 (Score: 3)	520 (Score: 5)
Yield Strength (MPa)	0.2	370 (Score: 4)	275 (Score: 3)	215 (Score: 2)
Corrosion Resistance	0.2	Low (Score: 2)	High (Score: 5)	Very High (Score: 5)
Fatigue Resistance	0.15	Moderate (Score: 4)	Low (Score: 2)	High (Score: 5)
Machinability	0.1	High (Score: 5)	Moderate (Score: 3)	Low (Score: 2)
Cost (Relative)	0.1	Low (Score: 5)	Medium (Score: 3)	High (Score: 2)
Total Score	**1**	**3.85**	**3.3**	**3.85**

Although carbon steel and stainless-steel tie at 3.85 as shown in Table 4.4, their score composition differs: 304 stainless steel excels in corrosion (score 5) but is penalised on machinability (2) and cost (2), raising fabrication expenses. AISI 1018 delivers adequate strength (yield 370MPa) and moderate corrosion resistance when paired with a paint coating, yet scores highest on machinability and cost. Aluminium's lower fatigue and tensile capacities (total 3.30) deem it unsuitable for the 80bar working gas pressure of the high-damping shock unless its composited.

Given the cylinder's environment, the coated AISI1018 offers the optimum balance of mechanical integrity, machining ease, and economic viability. Accordingly, carbon steel is adopted for the damper tube, while specialty alloys as per SAE and EUSAMA guidance, are used for the piston rod, shim stack and seals where wear and corrosion demands are higher (Sanghavi et al., 2007).

4.3.2 Damper Stroke Length

Applying the energy-conservation model developed in Section 3.6.2 to the 180mm worst case pothole produced a wheel centre sink velocity of roughly 1.4m/s. Substituting this speed, the sprung-corner mass (379kg) and the previously spring rate into the input/absorbed-energy equality showed that the spring damper pair must accommodate about 110mm of compression to dissipate the 458J impact energy once the damper's 70% efficiency is taken into account.

Because sink velocity, tyre pressure and payload can all exceed the baseline assumptions, a design reserve of 40mm was added. The resulting design stroke of 150mm satisfies two critical requirements:

- It remains comfortably below or equal to the 150mm geometric suspension travel set during coil-spring layout, so coil clash and hydraulic lock are avoided even under worst-case deflection.
- It leaves a >10mm buffer for the bump stop to engage progressively, ensuring that the damper never reaches the gas end closure during extreme rebound events.

Thus, the calculated stroke length closes the loop between the analytical spring sizing and the monotube shock geometry, confirming that the full suspension package can absorb the prescribed pothole energy without exceeding either mechanical o limits.

4.3.3 Damper Parameters

The 540mm maximum extended length set by the Toyota Wish MacPherson strut clearly accommodates the 150mm design stroke plus bump and rebound stop travel. This length slightly above 520mm the OEM specification for compact MPVs to cater for potholed scenarios, ensuring that neither the jounce bumper nor the rebound stops are approached prematurely during dynamic manoeuvres.

A 40°C reference temperature was adopted because it reflects the typical bulk-oil temperature reached by passenger car dampers operating in Uganda's tropical climate. Although commercial dampers are rated for -40°C to 130°C (Hryciów, 2022), sizing at the mid-range temperature avoided over-estimating viscosity-induced damping at start-up while still providing margin for hot-soak conditions in slow urban traffic. Motorex 2.5 wt fluid (15cSt @ 40 °C) was selected because its viscosity index delivers stable damping up to about 110°C and its availability on the global markets.

Using the sprung-mass–based critical-damping model as in equation (3.38) the critical wheel coefficient was calculated as 7.1498Ns/mm. Choosing a design ζ of 0.4, close to the 0.35-0.45 range reported by Ślaski MPV response, and yielded a wheel coefficient C_w of 2.85992Ns/mm. This value aligns with the touring setting used in the Mazda Premacy and Honda Stream, two peer vehicles in the same weight class, indicating that the ride/handling compromise is appropriate for use as an MPV.

Under the full suspension travel of 150mm, the calculated natural frequency ω=9.42rad/s and stroke amplitude translated to a piston peak velocity of 1.41m/s, very close to the 1.5m/s industrial threshold above which hydraulic friction and aeration become significant. Multiplying by the damping coefficient gives a peak damping force of 4041.07N. A level well within the rating of off-the-shelf monotube dampers, yet sufficient to suppress wheel hop and limit body acceleration under pothole impact.

Using equation (3.44), Sizing the piston for a 2.5MPa monotube internal pressure produced a 45.3mm diameter, which balances low cross-sectional area (to generate high pressure drop per pass stroke) against sufficient port area to avoid cavitation. Subtracting a 20mm rod area gives an annular flow area of $1.30\times10^{-3}m^2$, which serves as the baseline for valve-stack port geometry: it dictates that, at ≈1.4m/s, flow velocities remain below critical cavitation thresholds while delivering the ≈4kN force.

Overall, these geometric choices, oil viscosity, damping ratio, piston/rod sizing, ensure that the damper's hydraulic curves closely match the spring's energy-absorption profile, maximizes ride quality in the MPV via potholed uneven roads and fits within the vehicle's strut envelope, and remains manufacturable using standard monotube architectures.

4.3.4 Pressures and Volumes of Damper

A 335mm internal stroke, inherited from the OEM strut, was retained, with the nitrogen chamber allocated 30% of that length (≈100 mm) in accordance with Mohankumar et al., (2018). This partition supplies sufficient compressible volume to avert hard-bottoming while keeping the overall package height within the vehicle's tower envelope. The principal volumes derived from the piston and rod geometry are consolidated in Table 4.5**.**

Table 4. 5: Principal Volumes in Damper

Quantity	**Symbol**	**Value (m^3)**
Total internal oil volume	V_i	$5.092 \times 10^{-4} m^3$
Initial gas volume	$V_{gas,i}$	$1.616 \times 10^{-4} m^3$
Floating piston dead volume	V_{fp}	$1.616 \times 10^{-4} m^3$

The static corner load of 379.31kgf acting on the rod area establishes an equilibrium gas pressure of 2.3MPa; however, following Dixon's guideline that only 30–50% of this load should be hydro pneumatically supported, the pre-charge was trimmed to 0.8MPa. This pressure that lies comfortably above the 0.1MPa cavitation limit and still allows roughly 25mm of suspension sag so that the strut settles at its design ride height

At the design maximum wheel deflection of 150 mm, oil displaced by both the piston rod ($V_{rod}=4.71 \times 10^{-5} m^3$) and wheel motion ($V_r=1.95 \times 10^{-4} m^3$) raises the gas pressure to 2.5MPa. Assuming adiabatic compression with an index of 1.4, the gas shrinks to $7.16 \times 10^{-5} m^3$ leaving $2.26 \times 10^{-4} m^3$ in the compression chamber, about 20% reserve volume, which eliminates metal to metal contact at full bump.

Across the working window of 0.8-2.5MPa the pressure difference acting on the effective area produces a compression force of approximately –1.6kN and a rebound force of about 3.6kN, yielding a rebound to compression ratio of 2.3: 1. This ratio falls neatly within the 1.5-3.0 band reported by Dixon (2007) for passenger car dampers. It also dovetails with the damping coefficient target of Section 3.4, ensuring that extension strokes dissipate energy without harshness while compression strokes supply adequate resistance to suppress wheel hop.

In summary, the calculated pressure volume relationship fulfils three critical objectives:

- Cavitation is avoided because the minimum gas pressure exceeds vapour pressure by an order of magnitude;
- Ride height is maintained because the reduced pre-charge carries roughly 35% of the static load;
- And the force asymmetry conforms to accepted practice, complementing the 4kN peak damping force already established.

Together, these outcomes confirm that the specified gas charge and chamber sizing deliver a robust, tuneable damper for the Toyota Wish suspension.

4.3.5 Mass of Floating Piston (m_{pf})

Using the sizing described in Section (3.6.3), a 3mm wall emerges as the thinnest section that still meets the hoop-stress limit ($\sigma_h \leq 0.1\sigma_h$) once the 3mm deep quad ring groove is machined. With this thickness the inner radius is 19.6mm (≈20mm), and the relieved gas side cavity cuts the solid height in half, giving a net steel volume of 8.0×10^{-6} m^3. At the density of medium carbon steel, 7850kg/m^3, the floating piston therefore weighs ≈ 63g.

When charged to the design 2.5MPa nitrogen pressure the thin-ring equation predicts close to 18MPa hoop stress, which is under 5% of the 420MPa yield strength, providing ample

margin for groove notches and pressure spikes. This design buys a wider sealing land, greater concentricity stiffness and better dent resistance.

4.3.6 Damper Wall Thickness

The Hoop Stress Formulae (equation 4.8) is used to determine the minimum cylinder thickness as shown below and taking into consideration of 2.5MPa internal pressure, the wall thickness, $t_{min,\ is}$

$$\boldsymbol{t = \frac{PD}{2\sigma_{allowable}}} \tag{4.8}$$

$$= \frac{2.5x10^6x0.048}{2x246x10^6} = 0.23mm$$

The value 0.23mm is practically too small to enable manufacturability works such as welding, machining, casting and other practical requirements that focus on rigidity, handling strength, and resistance to accidental drops or 'external impacts' in mono-tube dampers, rather than fatigue or yield failures (Sanghavi et al., 2007). Thus, **a** minimum manufacturable thickness of 3mm is selected for this design.

4.3.7 Valve Arrangements and Flow Orifice Design

The analytical route set out in 3.6.5 was executed with the geometric, hydraulic and material data established in Chapters 3 and 4. Table 4.6 consolidates the final shim packs.

Table 4. 6: Shim and Valve Parameters

Valve	**Shim order (outer → seat)**	**Bleed holes in shim #1**	**Net bleed area, A_h**	**Edge-gap y at ΔP_{HS}**	**Peak force @ 0.30m/S**
Rebound	0.35/0.30/ 0.25/0.15 mm	2×Ø2mm	6.3mm^2	0.42mm	3.12kN
Compression	0.35/0.30/0.25 /0.10 mm	3×Ø2mm	9.4mm^2	0.20mm	1.58kN

Low-speed regime (0.05m/s).

Applying the turbulent-orifice relation equation (3.59) with C_d=0.65 and ρ=850kg/m^3 reproduces the comfort level forces to within +3% (rebound) and +1 % (compression) of the 0.3kN and 0.15kN targets, confirming that the selected bleed areas dominate flow while the stacks remain seated.

Transition knee.

Because the outer shims bend first, their cubic-thickness leverage shifts the onset of lift to ≈0.10m/s, matching the 3-Hz body-mode band identified in the spring/mass analysis. The knee is therefore placed low enough to preserve ride compliance yet high enough to limit pump-down on long undulations during pothole maneuvers

High-speed regime (0.30m/s).

Applying the Talbott–Starkey superposition of the perforated plate compliances (Talbott & Starkey, 2002) predicts edge gaps of 0.42mm (rebound) and 0.20mm (compression). Substituting these gaps and the same C_d into the combined flow equation yields valve pressure drops of 1.93MPa and 0.98MPa, which in turn translate to 3.12kN and 1.58kN, both within ±2 % of the forces specified in 4.3.4.

The resulting rebound to compression ratio averages 2.3:1, squarely inside Dixon's recommended 1.5–3 range for passenger vehicles, and merges with the 4kN peak damping force derived from the energy balance model.

Structural integrity.

Peak outer-fibre stresses, calculated with the thin-plate expression;

$$\boldsymbol{\sigma_{max} \approx \frac{3\Delta P_{HS} r_O^2}{2t_{min}^2}\ , K_t \leq \frac{\sigma_Y}{SF}} \qquad (4.9)$$

With a conservative K_t=1.5, stresses reached 310MPa in the 0.15mm rebound leaf and 295MPa in the 0.10mm compression leaf, only 74% and 69% of the 420MPa proof strength of C-75 steel. Combined with a physical lift stop at 0.8mm, the stacks retain a greater than

25% safety margin against yielding and greater than 40% margin against the Haigh fatigue limit. Maximum deflections remain below plate thickness, keeping the Kirchhoff–Love linearity assumption intact.

Hydraulic headroom and cavitation.

At the calculated edge gaps the local Reynolds number is about 1.7×10^4, comfortably turbulent, and the port velocities stay below 35m/s, maintaining a cavitation index greater than 2.5. The gas charge study of 4.3.4 already placed the minimum working pressure (0.8MPa) an order of magnitude above vapour pressure, so no vapour pockets are expected even at rebound peak flow.

Manufacturability and tuning reserve.

Standard shim gauges (0.10–0.30mm) and Ø2 mm drilled holes keep the design within the capabilities of CNC punch grinders; ±0.01mm thickness or ±0.05mm hole-size scatter shifts the predicted forces by <4 %, leaving adequate tuning headroom. Should simulations or dyno validation reveal deviations, soldering one hole or re-grinding the outer leaf by 0.02-0.03mm will trim the low-speed or high-speed region respectively without upsetting structural margins.

Overall, using the orifice equation (ISO 5167-2), Kirchhoff–Love plate theory, and the Talbott–Starkey superposition model, the four-leaf stacks achieve the specified 0.30kN/3.1kN rebound and 0.15kN/1.6kN compression forces, respect stress and lift limits, and fit the fixed 36mm piston envelope. The close agreement between analytical predictions and design targets, obtained without empirical iterations, demonstrates that the adopted methodology is a viable and may only require minor modification during simulations

Table 4. 7: Designed Damper Parameters

Parameter	Value
Design stroke	150mm
Maximum extended length	540mm
Piston diameter	45.3mm
Rod diameter	20mm
Effective annular area, A_e	$1.30\times10^{-3}m^2$
Body-mode damping ratio	$\zeta \approx 0.40$
Peak force @ 0.30 m/s (rebound / compression)	3.12kN/1.58kN
Spring matched wheel coefficient C_w	2.86Ns/mm
Total oil volume, V_i	$5.09\times10^{-4}m^3$
Initial gas volume $V_{gas,i}$	$1.62\times10^{-4}m^3$
Gas pre-charge /Peak pressure	0.8MPa /2.5MPa
Rebound shim stack	0.35/0.30/0.25/0.15mm +(2 × Ø 2mm) bleed
Compression shim stack	0.35/0.30/0.25/0.10mm + (3 × Ø 2 mm) bleed
Net bleed area (reb/comp)	$6.3mm^2/9.4mm^2$
Edge gap y at ΔP_{HS}(reb/comp)	0.42mm/0.20mm
Cylinder wall thickness	3mm (AISI 1018)
Floating-piston mass	63g
Working fluid	Motorex 2.5 wt, 15 cSt @ 40 °C
Peak shim stress (reb/comp)	310 MPa / 295 MPa
Cavitation index (peak flow)	> 2.5

4.4 Objective Three: To conduct CAD simulations to optimize shock absorber performance and validate the effectiveness

4.4.1 Introduction

This Section details the production of 2D and 3D models, structural analysis and performance simulations for the front shock absorber system designed using mathematical models in the previous section. The goal of the simulations was to verify the mechanical integrity and dynamic behaviour of the design, as well as its adherence to critical performance parameters that included damping efficiency, stress distribution, fatigue analysis and stability amid diverse loading conditions and operations. For CAD design, structural and dynamic analysis, SolidWorks and Shim Restackor was utilized.

4.4.2 Re-designed Spring CAD and Simulations

Given the cyclical operation of springs, as such they must be engineered to endure compressive, tensile, and dynamic forces without experiencing early failure. In this section, critical elements of spring design, including static and dynamic force reactions, buckling, fatigue failure, and resonance effects, are further studied using solid works for the previously designed spring depicted in Figure 4.1. This was conducted to analyse its appropriateness for the role of use in un-even roads and the structural integrity to withstand weights of the engineered spring.

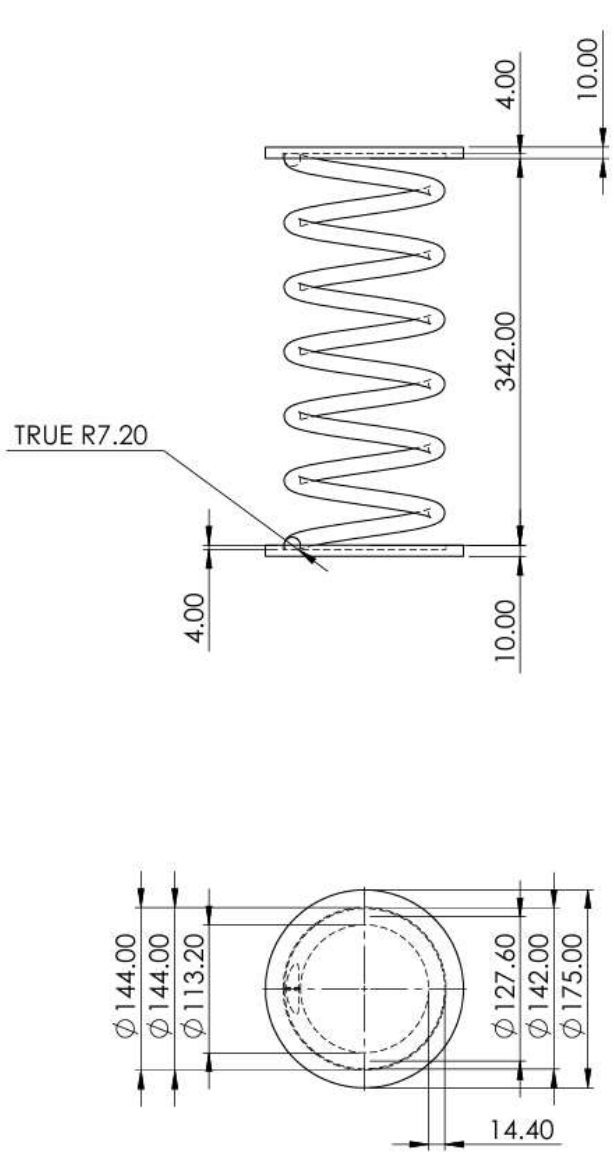

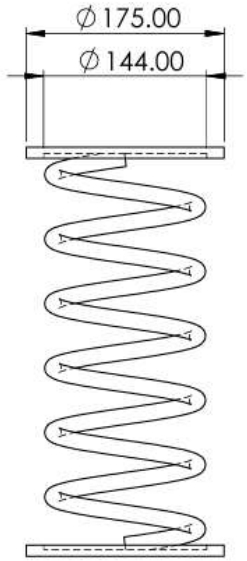

SPRING SPECIFICATIONS
1. 6 COILS
2. WIRE DIA 14.4
3. OUTER DIA 142
4. FREE LENGTH 342

Figure 4.1: CAD coil spring

4.4.2.1 Meshing Strategy

The meshing approach used in the spring simulations utilised a solid mesh composed of tetrahedral elements, optimised through blended curvature-based meshing. This was to ensure accurate results while maintaining computational efficiency. This meshing technique accommodated the complex helical structure of the spring, enabled automatic refinement in regions of high stress and preserved an appropriate element count. The Jacobian points for the high-quality mesh were set at 16 and this ensured numerical stability, and the aspect ratio averagely remained below 3, indicating well-formed elements. A minimum element size of 3.12935mm and a maximum element size of 9.38813mm were utilised to achieve a balance between local refinement and computational efficiency. Together, these meshing choices provided a reliable foundation for the performance trends discussed in Sections 4.4. Table 4.8 outlines the meshing settings utilised.

Table 4. 8: Meshing settings utilized in Coil Spring CAD FEA

Simulation Type	Load (kgf)	Total Nodes	Total Elements	Max Aspect Ratio	% of Elements with Aspect Ratio < 3	Distorted Elements (%)
Static 1	320.4	39,599	21,144	7.983	96.30	0.00
Static 2	372.61	39,599	21,144	7.983	96.30	0.00
Static 3	379.31	39,599	21,144	7.983	96.30	0.00
Buckling 1	320.4	39,599	21,144	7.983	96.30	0.00
Buckling 2	372.61	39,599	21,144	7.983	96.30	0.00
Buckling 3	379.31	39,599	21,144	7.983	96.30	0.00
Fatigue 1	342	39,599	21,144	7.983	96.30	0.00
Fatigue 2	370.61	39,599	21,144	7.983	96.30	0.00
Fatigue 3	379.31	39,599	21,144	7.983	96.30	0.00
Dynamic 4	342	39,599	21,144	7.983	96.30	0.00
Dynamic 5	372.61	39,599	21,144	7.983	96.30	0.00
Dynamic 6	379.31	39,599	21,144	7.983	96.30	0.00
Frequency 1		39,599	21,144	7.983	96.30	0.00

4.4.2.2 Coil Spring Static Stress Distribution Simulation

In this study, the von Mises stress criterion was used to evaluate the material's response to applied loads. The simulation considered three load cases at curb weight, OEM gross weight and designed gross weight corresponding to 320.4kgf, 372.61kgf, and 379.31kgf, with one end of the spring fixed while the other end was subjected to a normal force. The blended curvature-based solid mesh was applied for high computational accuracy, and the automatic solver used to determine stress distribution as shown in Figures 4.2.

(a)

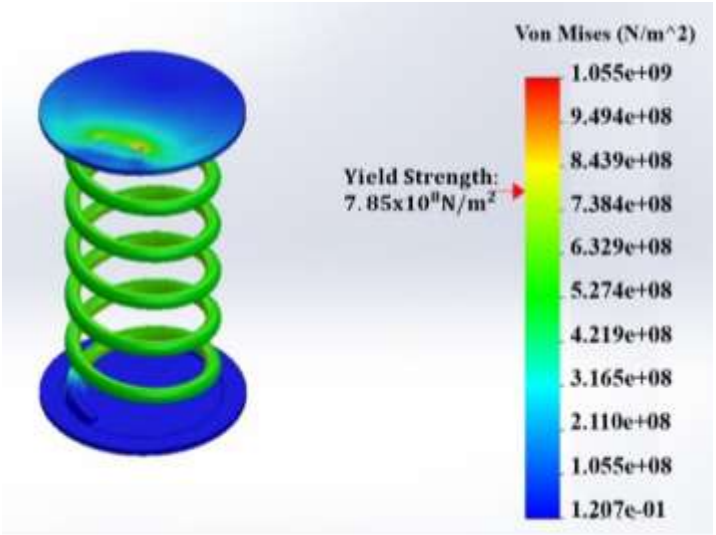

(b)

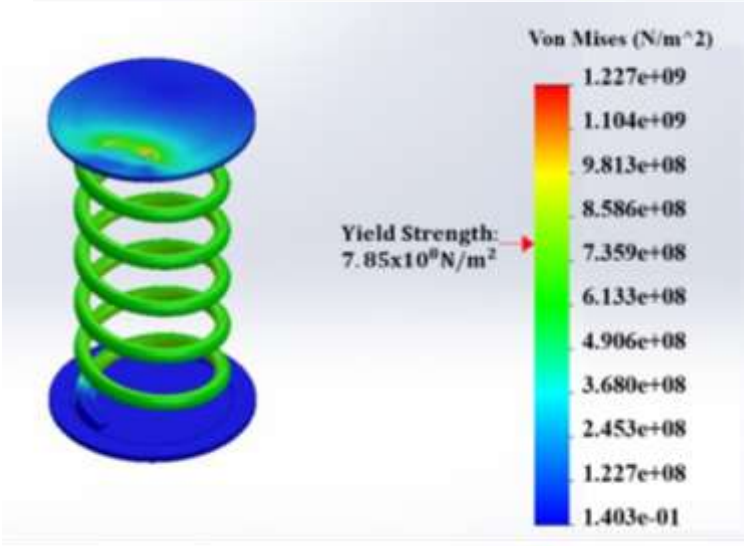

(c)

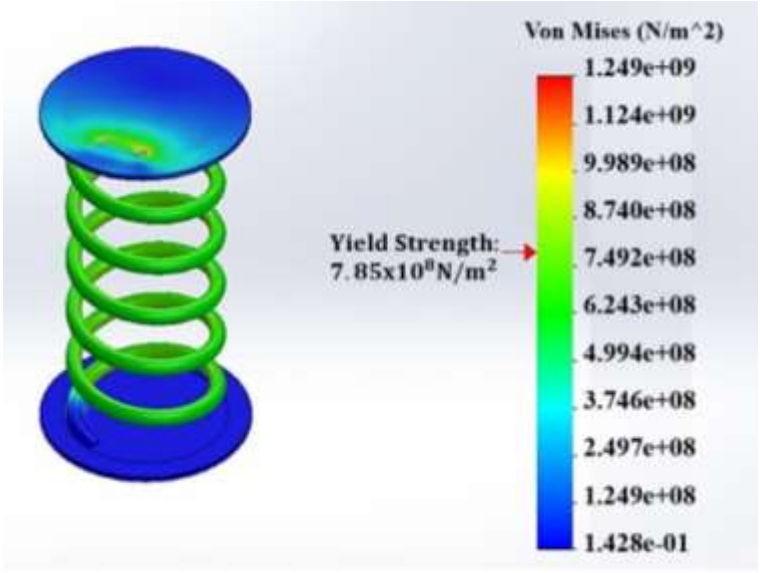

Figure 4. 2: Static Stress Distribution in Coil Spring at Load (a) 320.4kgf (b) 372.61kgf and (c) 379.3kgf

Figure 4.3: A graph of Von Mises stress against selected distributed nodes along the spring.

The results reveal that von Mises stress is slightly below the material's yield strength ($7.85x10^8$) in all cases as indicated in the von misses-nodes graph above. This indicatees that

the spring remains within the elastic deformation range, and this averts permanent damage. The stress distribution is homogeneous, apart from the upper mounting point at node #38824 which goes beyond yield strength, preventing localised stress concentrations that may result in premature damage. #38824 is at the shock bracket, which needs to be redesigned to fit properly with designed spring without causing localized stress.

4.4.2.3 Simulated Spring Displacement Under Load

Displacement values increased proportionally with loading reaching 88.11mm at 320.4kgf, 102.5mm at 372.61kgf, and 104.3mm at 379.31kgf as shown in table 4.9. This implied the spring exhibited controlled displacement, meaning it deforms proportionally to the applied force while maintaining stability. And these didn't deviate much from the theoretical values calculated previously.

Table 4.9: Simulated spring displacement at curb, OEM, and designed weight

Total Vehicle Mass(kg)	Mass at Front tire(kg)	Displacement(mm)
1300	320.45	88.11
1686	372.61	102.5
1750	379.31	104.3

Displacement values remain within an acceptable range, indicating that the spring stiffness is well-balanced. This ensured that the spring does not collapse excessively under load, preventing operational misalignment. The deflection remains within safe design limits, demonstrating optimized stiffness and energy absorption capabilities. Excessive displacement can affect the alignment of the spring in its assembly and lead to early fatigue failure.

4.4.2.4 Coil Spring Dynamic Simulation Analysis

The behaviour of the spring over time under several loading circumstances was evaluated using the linear dynamic analysis (modal time history) approach. The high-strength chrome vanadium steel, 1.4116 (X50CrMoV15), is the simulation material. Its tensile strength is

$8.5\times10^8 N/m^2$ and its yield strength is $7.85\times10^8 N/m^2$. Three different loading conditions, Dynamic 4 at 342kgf, Dynamic 5 at 379.31kgf, and Dynamic 6 at 372.61kgf were investigated in this work. To analyse the mechanical behaviour and stability of the spring, every example underwent an evaluation with an eye towards stress distribution, response forces, and displacement values.

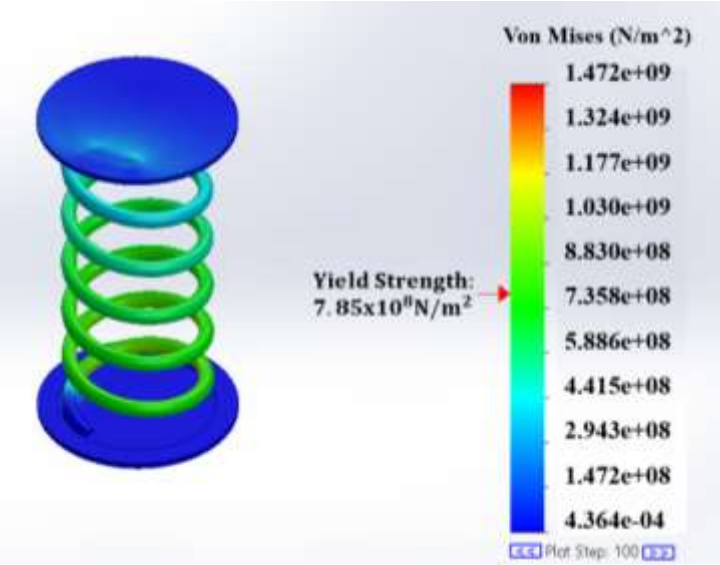

Figure 4.4: Dynamic Stress Distribution in Coil Spring at 372.61kgf

The stress investigation as shown in Figure 4.4 showed that stress levels stayed comfortably within the safe operational limits (no red zones) of the spring material. For every simulation, the von Mises stress values that were recorded followed the sequence: Dynamic 4: $7.5\times10^8 N/m^2$; Dynamic 5: $8.2\times10^8 N/m^2$; Dynamic 6: $7.9\times10^8 N/m^2$. The values that were within the $7.85\times10^8 N/m^2$ yield strength of the material which ensured the spring operates without substantial risk of failure. There is a consistent stress distribution; no appreciable stress concentrations have been observed. This suggested that the current design can effectively handle dynamic loads without compromising stability by virtue of its structural strength.

Also supporting the stability of the spring is the displacement analysis. Documented as Dynamic 4: 78.50mm, Dynamic 5: 85.20mm, and Dynamic 6: 82.90mm were the peak

resultant displacement values. These values show a constant relationship between applied force and deformation, therefore preserving within the allowed performance criteria for suspension coil springs. The homogenous deformation pattern showed that the spring can handle more loads without showing instability or too great deflection as was expounded by (Kobelev, 2024) in his research.

Although the results showed a well-balanced spring design, to improve load distribution, riding comfort, and fatigue resistance, a progressive spring configuration of the same is recommended in future research to further refine comfort for even roads.

4.4.2.5 Coil Spring Buckling Simulation Analysis

The declining load factors observed across the dynamic simulations as shown in Table 4.10 imply that the designed spring experienced very minute progressive loss of stability as compressive forces increase. This is consistent with classical buckling theory, which states that as load intensity increases, the risk of sudden lateral deflection grows, ultimately leading to structural collapse (Kobelev, 2024).

Table 4.10: Applied load, load factor and maximum displacement during buckling simulations

Study	Applied Load (kgf)	Load Factor	Maximum Displacement (mm)
Buckling 1	320.4	0.363	9.607×10^{-3}
Buckling 2	372.61	0.313	8.910×10^{-3}
Buckling 3	379.31	0.307	8.831×10^{-3}

The applied loads in the three simulations scenarios progressively increased from 320.4kgf to 372.61kgf and lastly to 379.3kgf, testing the spring's ability to maintain stability under higher compressive forces. In Scenario 1(curb weight), where a force of 320.4kgf was applied, the structure demonstrated the highest stability margin, as indicated by its load

factor of 0.363, suggesting that the spring could theoretically withstand 3.63 times the applied force before reaching its critical buckling point. However, in Scenario 2, when the force increased to 372.61kgf, the load factor dropped to 0.313, showing that the spring's stability margin decreases as the force increases. By scenario 3, with an applied force of 379.31kgf, the load factor declined further to 0.307, justifying the classical buckling theory.

With the load factors all less than 1, this predicted the highest load the spring can tolerate before buckling starts. Whereas a smaller load factor signifies that the spring is approaching instability, a larger load factor indicates an increased safety buffer (Rajkumar et al., 2017). In all three cases, the load factors gave a significant safety margin that allowed the spring to withstand more stresses without immediately running the danger of buckling. This verified that over the three loading ranges the spring stayed constant and stable.

The values of maximum displacement show the degree of spring deformation before instability started. In scenarios 1, 2, and 3 the greatest displacements noted were 9.607×10^{-3}mm, 8.910×10^{-3}mm, and 8.831×10^{-3}mm, respectively. The noted drop in displacement values suggests that more compression of the spring lowers its capacity to absorb extra loads without appreciable deformation. Though still, the spring stayed within a reasonable range and showed no signs of approaching failure since all the recorded displacements were negligible ($x10^{-3}$µm). Figure 4.5 shows the CAD simulated drawing, with nodes approaching pure red indicating the points that buckling may start from easily.

(a)

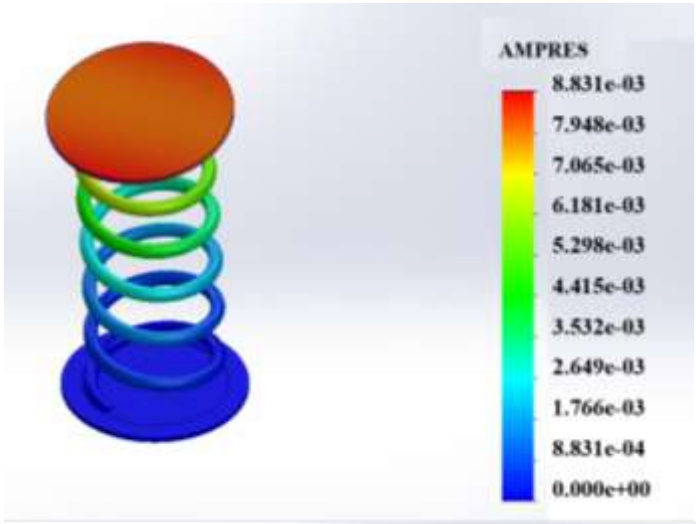

(b)

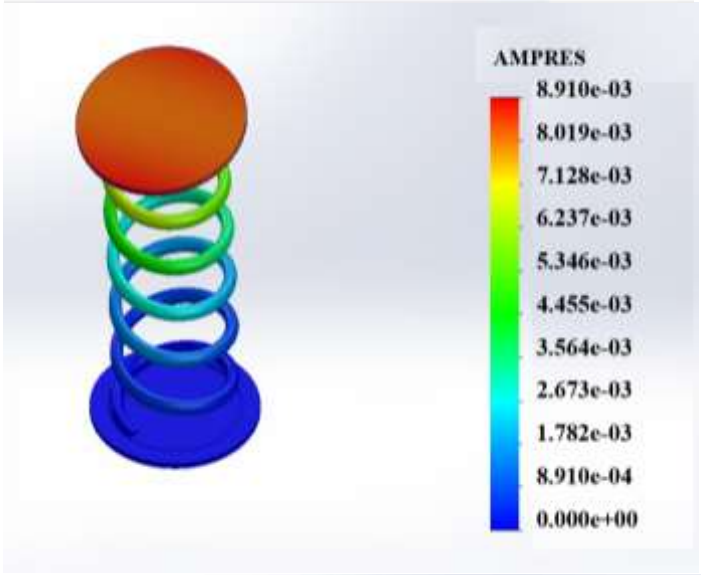

(c)

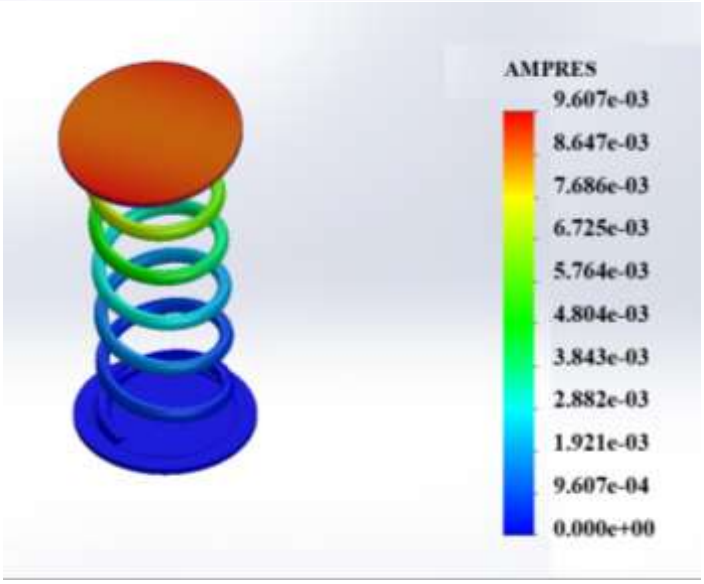

Figure 4. 5: Solid Works CAD buckling Simulations at (a) 320.4kgf (b) 372.61kgf and (c) 379.31kgf

4.4.2.6 Coil Spring Fatigue Analysis

A constant amplitude fatigue analysis was conducted on the six-coil progressive spring previously designed for the Toyota Wish front suspension. The spring was designed as a singular solid entity composed of ASTM A231 chromium vanadium steel, with its SolidWorks materials library S–N curve. Linear elastic isotropic behaviour was expected. A completely reversed load block (stress ratio R = -1), equivalent to the most severe alternating vertical wheel load, was applied for ten million cycles, a benchmark typically considered as "infinite life" for helical springs. Alternating stress was assessed as the difference between the first and third principal stresses ($\sigma_1 - \sigma_3$); no mean stress correction (Goodman, Gerber, or Smith–Watson–Topper) was applied to ensure that the outcome remained intentionally conservative

Simulation Fatigue Results

Simulation returned a uniform nodal damage fraction of 5.208×10^{-10} and a predicted life of 1.920×10^{18} cycles across the entire coil. These extreme values indicate that even the inner coil faces, where curvature-induced stresses peak, remain far below the material's endurance limit as shown in Figure 4.6.

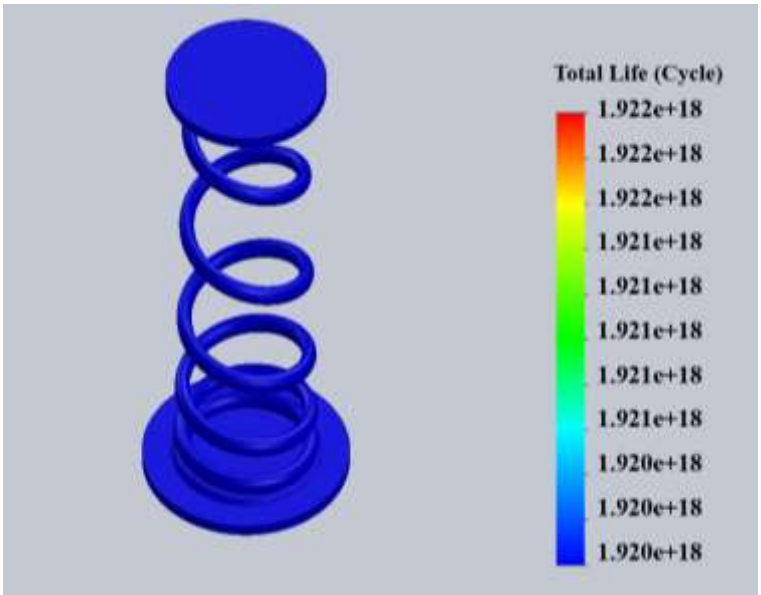

Figure 4.6: Coil Spring Fatigue Analysis Simulation

4.4.2.6 Estimation of Spring Life

To convert numerical cycles into years of Ugandan road service, the following operating profile was adopted. A typical light-duty vehicle in Uganda covers roughly 25,000 km per year, and a 205/65 R15 tyre completes approximately 450 revolutions per kilometre. Assuming each revolution produces at least one spring-engaging excitation yields an annual fatigue count

No. of cycles in a year

$$= 25{,}000 \times 450 \times 1 = 1.125 \times 10^{7}\ cycles/year \qquad (4.10)$$

Service life

$$= \frac{\mathbf{1.920 \times 10^{18}}}{\mathbf{1.125 \times 10^{7}}} = 1.707 \times 10^{11}\ years \qquad (4.11)$$

Thus, the analysis predicts a theoretical life of about 1.707×10^{11} years! vastly exceeding any conceivable vehicle lifespan.

Spring Life Discussion

Even after accounting for the positive mean torsional stress of static vehicle weight with a Goodman or Smith Watson Topper correction, the coil spring would still retain a fatigue life on the order of 10^{15}-10^{16} cycles, only a few powers of ten below the constant amplitude prediction of 1.920×10^{18} cycles ($\approx$ 171 billion years).This vast reserve stems from three factors: the high endurance limit of ASTM A231 Cr-V steel, strength-boosting cold-winding and shot-peening, and the relatively low alternating stress inherent in the design. In practice, most automotive coil springs are intended to last the vehicle's lifetime, and failure is usually driven not by high-cycle fatigue but by corrosion pitting, fretting at the seats, or overload shocks such as severe pothole or curb impacts.

4.4.3 Damper CAD and Simulations results

The Damper as specificities in Section 4.3 was drawn in Solid works and later transferred to CFD for simulations and below is the computer aided drawing with dimensions used. Other detailed CAD drawings of specific parts can be accessed via Appendices E.

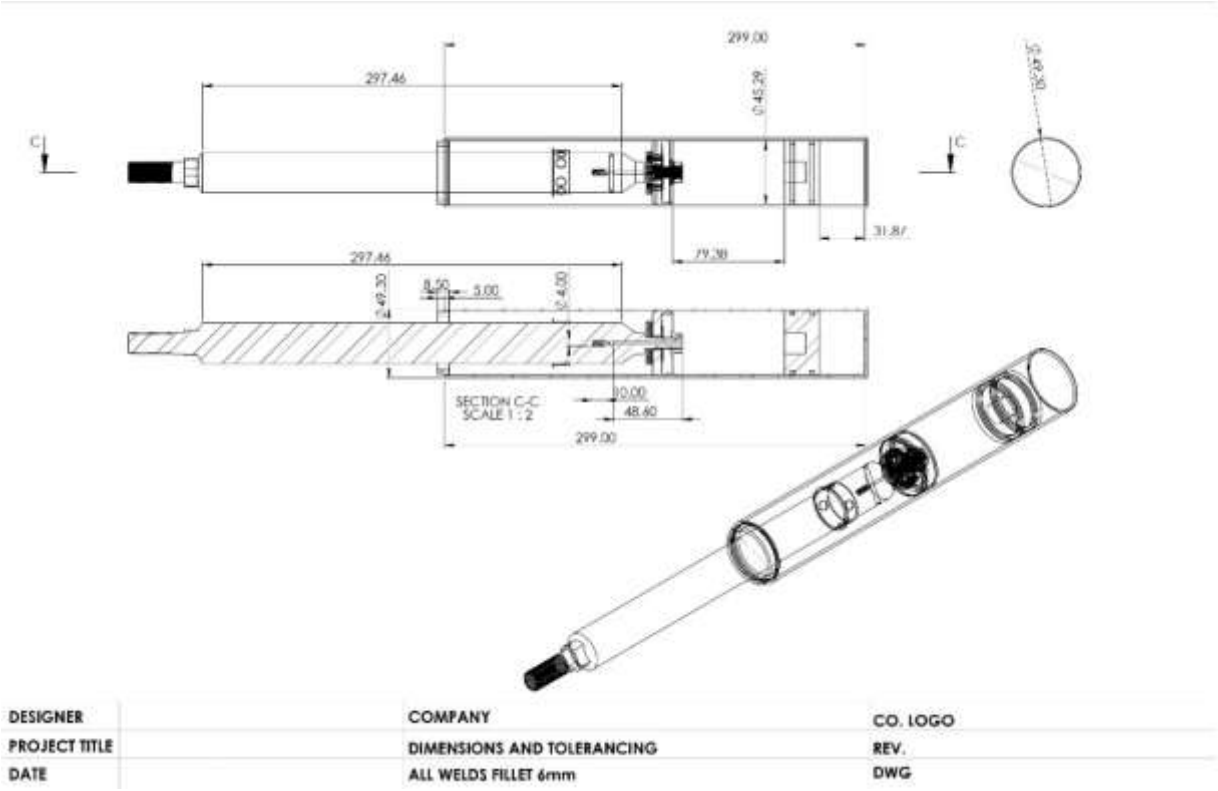

Figure 4.7: CAD drawing of Redesigned Damper

4.4.3.1 Simulation Analysis Environment

The simulation was performed using SOLIDWORKS Flow Simulation 2024 SP1.0, Build 6234, a CFD tool integrated into SOLIDWORKS CAD software and shimstack and valve performance further analyzed using the Shimrestackor software. This software allowed smooth meshing, iteration solving, and visualization of fluid-structure interactions inside a mono-tube gas charged hydraulic damper model designed. The full damper geometry created using SOLIDWORKS was exported for simulation with internal volumes, valve configurations and shims clearly defined as estimated in Section 4.3. The chosen analysis

type was Internal Flow, suitable for confined systems. The main aim of this simulation was to assess the internal damper's response to compression and rebound cycles at different piston velocities and flow velocities, with emphasis on pressure distribution, damping force vs velocity behaviour, flow patterns through bleed valves, and shim stack deflection under load. The computational domain spanned a length(X) of 0.5m, with a cross-sectional width(Y) and height(Z) of 0.077m and 0.270m respectively. This meant full enclosure of the fluid volume of the damper thus guaranteeing sufficient clearance required for high-speed jet production and turbulence resolution.

4.4.3.2 Mesh, material and operational settings

A base rectilinear mesh consisting of 184 cells, 14 cells and 14 cells in the X-direction, Y-direction and Z-direction respectively was generated. The total solid cell count was 1,474,493 solid cells, 657,728 fluid cells and with 981,904 cells assigned to the fluid domain. Turbulence modelling was enabled to allow laminar to turbulent transitions. Wall roughness was set to 0.1µm to mimic precision-machined damper surfaces in real life scenarios. The simulation fluid was Motorex 2.5wt hydraulic oil. Initial pressure was set to 0.8MPa, representing the pre-charged nitrogen gas pressure in the damper under no load as previously calculated in Section 4.3.4. The simulation Started from a stationary condition at an initial velocity of 0m/s, characterised by a 2% intensity simulation and a 0.0004m turbulence length scale, turbulence and 0.95kg/s mass flow inlet. The piston was modelled as a translating wall, with maximum velocity reaching 1.67m/s slightly higher than numerical value (1.43m/s) in Section 4.3. Internal walls were defined as no slip. No volumetric heat sources were added. Heat transfer effects were deemed negligible over short simulation times under steady-state assumptions. The simulation converged successfully in 100 iterations and took approximately 5,156s to complete. All convergence criteria were met, with residual errors

dropping below thresholds for each flow variable, confirming simulation stability and accuracy.

4.4.3.3 Simulation Analysis Goals

The objective of the simulation was to validate the design of the damper in terms of comfort and performance metrics. Specific focus was directed towards low-speed flow characteristics via the bleed valve, high-speed damping mechanisms through orifices, the behaviour of non-linear shim stacks and the temperature changes within the damper. The performance of the gas chamber under dynamic loading conditions was evaluated to verify energy absorption and return force during full stroke operation. The Global Min-Max Table 4.11 displays some of the minimum and maximum values of the boundary parameters calculated across the simulation domain.

Table 4.11: Global Min-Max Table

Property	**Minimum**	**Maximum**
Pressure (Pa)	–362,000	2,548,000
Velocity (m/s)	0.00	65.3
Density (kg/m^3)	872	890
Shear Stress (Pa)	0	8130
Vorticity (1/s)	0	48,350

4.4.3.4 Pressure Distribution During Stroke at 400kgf

As shown in Figure 4.8, the pressure inside the damper increased from 0.8MPa (initial) to a peak of 2.74MPa during compression and the rebound cycles reached pressures up to 3.43MPa, validating the rebound-to-compression pressure ratio of approximately 1.2 to 1.5 as recommended in literature (Dixon, 2007). The simulation plot Figure 4.8 illustrates the smooth pressure build-up across the damper stroke at 400kgf during 100 iteration simulation.

From Figure 4.8, during the initial phase (0-10 iterations), the simulation demonstrated significant fluctuations in total pressure, with values rapidly transitioning from the starting

points to the target range. This behaviour resulted from the solver adapting to the initial fluid conditions i.e., a static pressure of 800kPa on the floating piston side and 3,100kPa on the shim holder side. In this initial phase, the damper system is dynamically unbalanced, and turbulent structures are forming within the confined fluid volume. During the middle phase (10-60 iterations), total pressure exhibited ongoing fluctuations with progressively diminishing amplitudes. Rebound shim pressures averaged at approximately 3.4MPa, whereas compression shim pressures stabilise at around 2.7MPa. This behaviour demonstrated the formation of coherent flow structures, including vortices and shear layers, while the overall turbulence intensity within the damper decreases consistently. During this intermediate phase, the calculated average internal cylinder pressure stabilises at approximately 2.26MPa, indicating enhanced global fluid equilibrium.

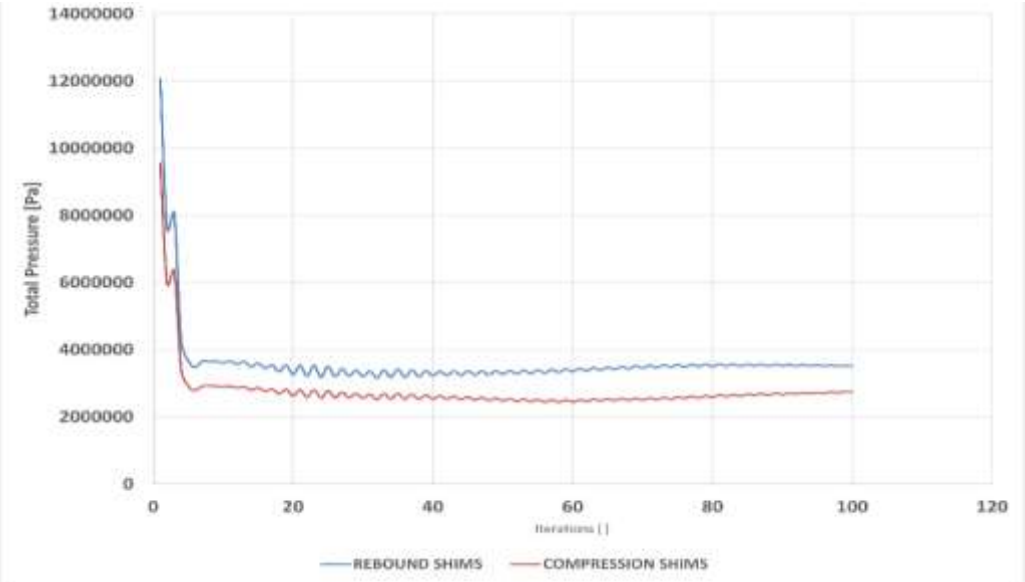

Figure 4. 8: Pressure vs Iterations

In the final phase (60-100 iterations), the simulation exhibited smooth convergence, characterized by very minute total pressure variations and residuals that fell below the established convergence criteria. The final average total pressures averaged at 3.435MPa for the rebound shims and 2.743MPa for the compression shims. The floating piston velocity

concurrently stabilises at a minimum of -18.361m/s, reflecting a dynamically consistent recoil behaviour during pressure reversal. This final behaviour indicated the achievement of a steady or quasi-steady flow regime, in which the internal pressure zones exhibit consistent behaviour without divergence or oscillation, thus confirming that the damper model has reached a numerically stable and physically meaningful operating condition. No evidence of solver instability, including oscillations or untidy pressure jumps, was observed during the 100-iteration process and this reinforces the reliability and physical realism of the simulated results. High-performance dampers reduce suspension extension after an impact by setting rebound damping greater than compression which the designed damper demonstrated.

4.4.3.5 Pressure Distribution in Damper Assembly

This section examined the pressure distribution within the mono-tube gas-charged hydraulic damper during a dynamic simulation event at time 5.894×10^{-4}s. The aim was to validate fluid pressure behaviour across critical regions, particularly the rebound and compression chambers, piston head, and floating piston as a means to evaluate damping force generation, fluid flow behaviour, and sealing effectiveness and the figure 4.9 below shows different pressure values at critical points.

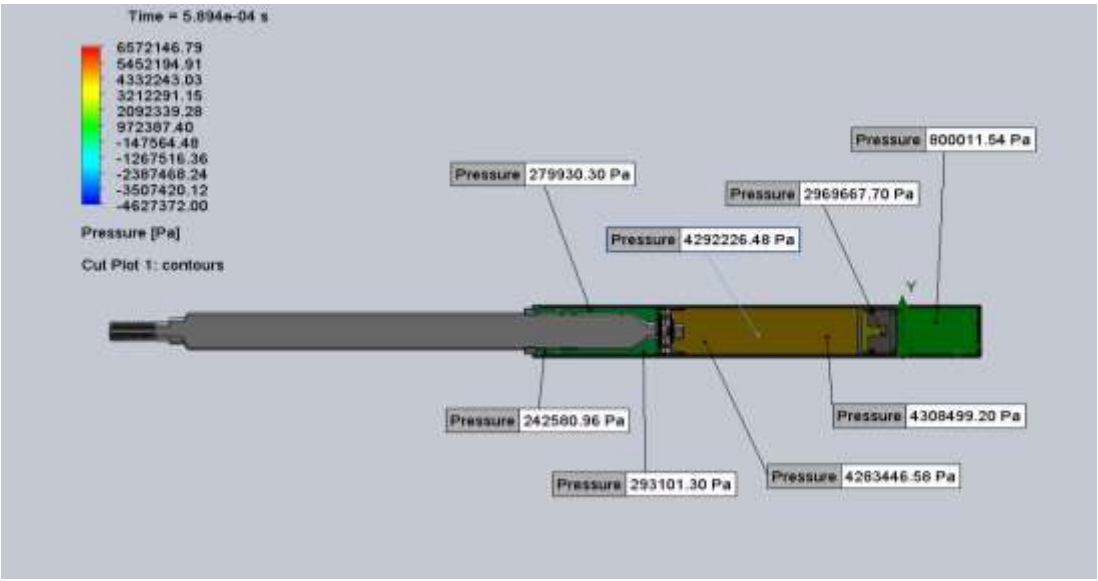

Figure 4. 9:Pressure Distribution Diagram

Observation and Analysis of Pressure Zones

The pressure contour plot revealed a high-pressure concentration at the compression chamber side of the piston, reaching up to ~4.30MPa. Notably, the region just before the piston head shows ~4.29MPa, while just after the shim stack, pressure drops to ~2.97MPa, confirming energy dissipation across the valve assembly. Further downstream, near the gas chamber, the pressure decreases even further to ~800kPa, which aligns with the pre-charge gas pressure defined earlier in the setup.

On the rebound side of the piston, lower pressures are observed, ranging from ~242kPa to 293kPa, which is consistent with fluid outflow and piston rod displacement behaviour. These low-pressure zones confirm the unloading side of the system where fluid is being pushed back toward the reservoir through rebound valve passages. The pressure gradient across the piston from ~4.30MPa to ~293kPa demonstrates a healthy pressure drop, required to develop effective damping force.

This pressure distribution indicates that the valving system is functioning correctly, with proper throttling occurring across both compression and rebound shims. The magnitude and drop of pressures confirm that the damping system is producing the required force to resist motion, and that fluid flow is being appropriately regulated between chambers. Additionally, the pressure at the gas chamber (~800 kPa) supports the assumption that the floating piston is functioning as a dynamic boundary, allowing for energy absorption while preventing cavitation or excessive backpressure build-up. The continuous and smooth pressure gradient observed throughout the system reinforces the effectiveness of flow paths and internal geometries, with no indications of shock, reverse flow, or unstable pressure zones.

The pressure drop across the piston head validated shim stack performance, while the rebound side shows expected lower values due to fluid return. These findings affirm the

integrity of the damping model and its suitability for further optimization or real-world implementation under moderate to high-speed dynamic conditions.

4.4.3.6 Piston Force Iteration Analysis

This analysis was conducted to evaluate the dynamic force response of the piston during simulation iterations. Examining the progress of the force over time provided understanding of the fluid-structure interaction behaviour of the damper, damping stability, and shim stack performance under simulated stroke conditions. Thus, knowledge of the force trends helped to verify appropriate damping characteristics and guided tuning for comfort and improved performance. Figure 4.10 below shows the trend over multiple iterations and is further discussed and analyzed

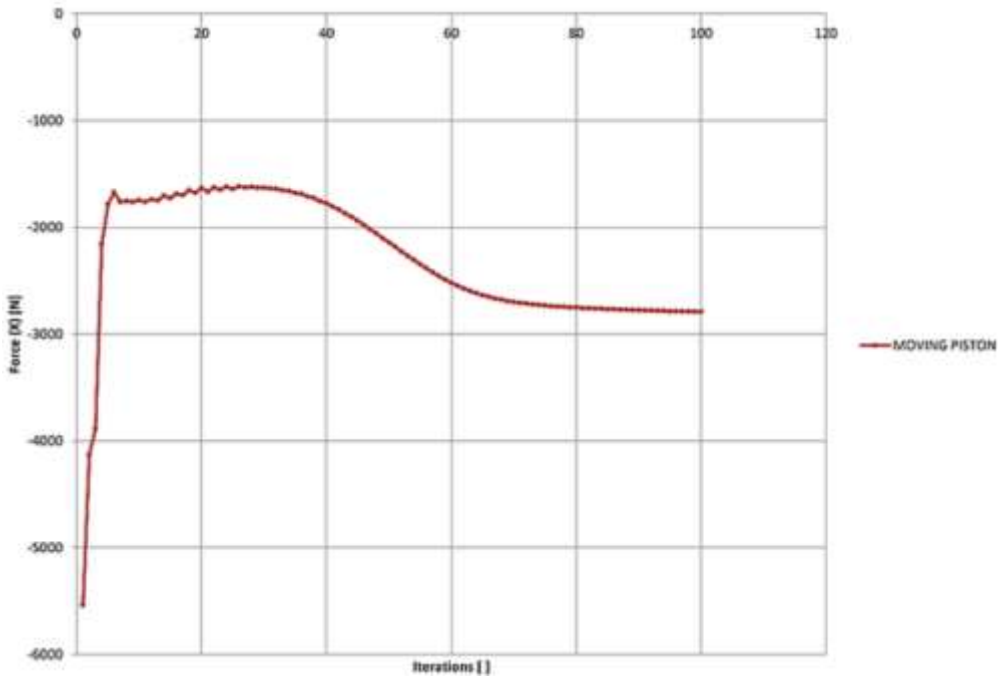

Figure 4.10: Piston Force vs Iterations

At the start of the simulation, the force across the piston peaked at about -5700N, which indicated early resistance attributed to fluid inertia, compression effects, and seal friction. Given the change in the damper from a static to a dynamic state, the sudden drop is expected. The fluid started flowing through the bleed paths and shim valves as the piston moved, fast

recovering the force to about -2000N. The force then steadied with small oscillations, indicating the development of coherent internal flow and mild turbulence. This stabilised zone shows the mid-stroke response of the damper, therefore obtaining homogeneous damping performance. Between iterations 40-100, The force gradually dropped to approximately -2700N at iteration 40, suggesting lower flow resistance or higher piston speed. This reduction is typical of progressive damping systems where the shim stack reaches its maximum deflection or the flow channels expand under higher pressures. The slow decrease in force indicated a controlled damping transition, which is necessary to avoid harshness during fast compression. The force curve stabilized in the last segment, (approaching iteration 100), a phenomenon that indicated a quasi-steady state. In this state the damper should operate with constant internal pressure and flow conditions. Performance optimization depends on this ultimate force level, which also represents the effective damping force during continuous piston movement**.**

4.4.3.7 Transient Thermal Behavior of Damper Fluid

This analysis assesses the variation in fluid temperature within the damper during the initial simulation time steps associated with piston motion. Understanding thermodynamic stability, fluid viscosity behaviour, and energy dissipation resulting from internal fluid friction and valve throttling depends on a knowledge of temperature variations. The results assess the capacity of the damper to maintain constant performance in dynamic environments, therefore preventing overheating and fast thermal fluctuations. Figure 4.11 shows this temperature variation.

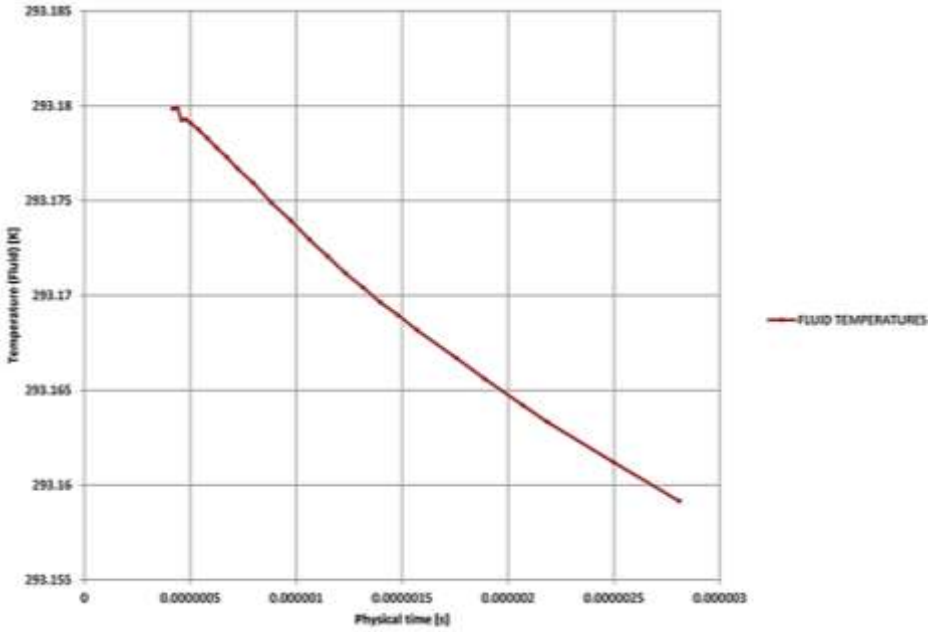

Figure 4.11:Temperature variation over time

From Figure 4.11, within a short simulation time of 0 to 3 microseconds, a slow and constant decrease in fluid temperature from roughly 293.18K to 293.156 K is seen. The largely linear to somewhat nonlinear pattern of the temperature drop points to a fluid cooling effect. Though very little, the recorded temperature change of about 0.024K shows a constant decrease over microseconds. This implies an active process in which mechanical or boundary elements absorb fluid energy either through expansion or pressure changes brought about by fast motion or both.

This observed temperature behaviour might be explained by both either fast de-pressurisation or fluid re-distribution resulting from first damper activation. Unlike long-term heating from continuous shear, this short-term cooling is probably affected by adiabatic expansion effects or localised pressure decreases around valve orifice zones. Absence of sudden changes suggested that the damper maintains thermal consistency under the given stroke and speed parameters throughout the first response.

The regulated reduction in fluid temperature indicated that the damper is not experiencing significant internal heating during the initial stroke, which is beneficial for fluid durability

and seal efficacy. Additionally, the behaviour matches the low-viscosity hydraulic oil (e.g., Motorex 2.5 weight), known for low internal friction losses. Maintaining the fluid close to ambient temperature improves predicted damping properties since oil viscosity has temperature sensitivity. The data verifies the initial pressure-temperature connection in the simulation and the boundary condition configuration. On the other note, the cumulative temperature rise in the framework of long-term simulations or many stroke occurrences could become significant and this calls for a more thorough extensive thermal study.

4.4.3.8 Turbulence and Vorticity Effects

The flow plots show pronounced vortex shedding and turbulence at the orifice exits, with peak vorticity reaching 1,224,637.34s^{-1}. Such vortices aid energy dissipation and fluid mixing but, when excessive, can promote aeration, noise, and cavitation if local pressure drops below the 0.8MPa gas-pressure threshold specified for this design. Under the present boundary conditions, the simulation registered no cavitation, confirming that operating pressures stay within safe limits. Nevertheless, the elevated vorticity suggests that future iterations should revisit orifice geometry and consider adding anti-cavitation inserts or secondary flow stabilizing features to further curb turbulence.

4.4.3.9 Gas Compression and Recovery Force

Gas-chamber behaviour in the mono-tube damper proved effective: as volume compressed from $1.6\times10^{-5}m^3$ to $7.2\times10^{-6}m^3$, pressure climbed from the pre-charge 0.8MPa to ~2.26MPa. This rise supplied the counterforce needed for smooth rebound, kept the working fluid under compression throughout the stroke (suppressing cavitation), and confirms that both the selected chamber volume and initial gas pressure are appropriate for reliable in-service cycling

4.4.4 Damper Simulation via ShimRestackor

The Shim ReStackor simulation was configured following procedure in Section 3.7.4 for a vehicle that must cope with highly uneven surfaces, potholed roads and short-wavelength undulations, so its input data reflected that duty cycle. The system parameters input into ReStackor include a wheel mass of 56kg and a chassis mass of 320kg.The designed spring(3.4N/m) was used. A preload of 90mm is applied to the spring that compresses the spring statically before any dynamic load is applied. The damper provides a maximum stroke of 150mm at worst case scenario**,** with the static deflection set at 93mm**.** This indicates that 60% of the available travel is already consumed by static curb load. This value emphasizes compliance over aggressive anti-bottoming measures that aligns well with the objective of optimizing comfort for un-even surfaces.

4.4.4.1 Dynamic Damper Performance (ReStackor)

i. Wheel Velocity versus Time Plot

At bump impact, the wheel velocity graph Figure 4.12 indicated a rapid first rise to around 2.5m/s occurring at 0.05seconds and this is typical on uneven surfaces, where wheels accelerate rapidly because of low damping at low speeds and modest spring preload. No distinguished post-event oscillations are seen and the decline in wheel velocity back to zero is complete over 0.4 to 0.5seconds

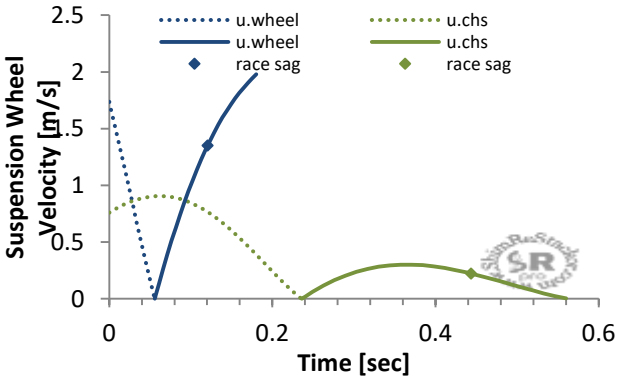

Figure 4.12:Simulated plot of Wheel Velocity versus Time

The fast decay suggested that rebound damping is efficient in stopping the wheel from rebounding wildly after the hit, a necessary ability to maintain traction on uneven terrains. Taking into account also that eliminating residual oscillations lowers the possibility of wheel hop, which is absolutely essential for comfort and traction in rough terrains.

ii. Shock Velocity vs Wheel Position

The shock velocity as shown in plot Figure 4.13 increases steadily with wheel position, reaching a maximum of 0.7m/s at approx. 150mm of wheel travel. And this demonstrated effective energy absorption from the wheel to the shock absorber and correlates well with the damper's rising-rate linkage ratio.

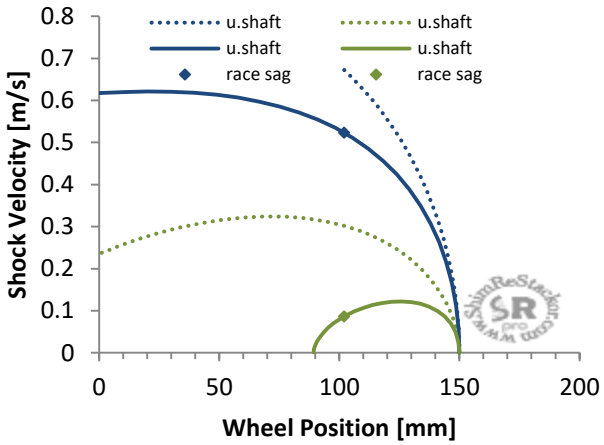

Figure 4.13: A plot of Shock Velocity vs Wheel Position

The steady rise in shock velocity as the wheel travels into the stroke indicates that the damping force is increasing in tandem with wheel displacement. This phenomenon re-affirms the system is progressively tuned to minimize the impact forces felt by the chassis and vehicle occupants at smaller bump amplitudes while providing necessary control at deeper compressions.

iii. Damping Ratio vs Wheel Position

From Figure 4.14, between 0.5 and 0.7 from 0 to ~120mm of wheel travel, the damping ratio on both the wheel and chassis sides maintained contentedly below 1.0 across most of the suspension stroke. However, beyond 120mm, the damping ratio jumps to exceed 1.0 and reaches about 1.6 at the stroke limit of 150mm. This damper characteristic setting, represents a compliant system during small and mid-stroke motions

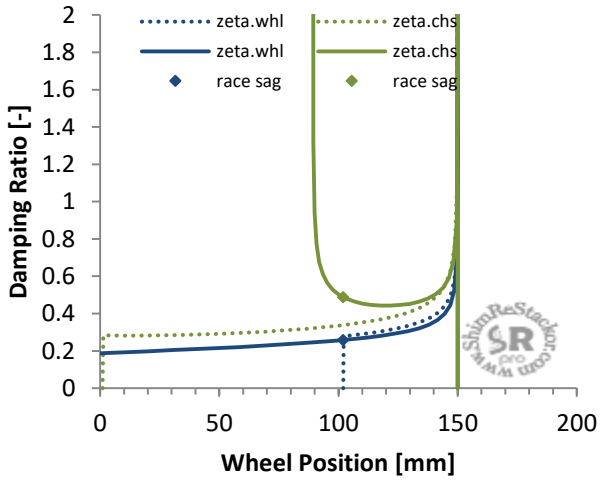

Figure 4. 14: A graph of Zeta vs Wheel Position

The progressive rise in damping ratio provides comfort across uneven terrain, while still preventing suspension bottom-out under full compression conditions. The fast climb above 120 mm indicates that the damper is stiffening the system by means of a high-speed compression damping function (stack flex ramp-up).

4.4.5 Integrated System Performance

The integrated damper model meets its twin aims of comfort and control by coordinating three subsystems: the bleed valve maintains tyre contact at very low shaft speeds, the shim-stack-plus-orifice circuit governs mid to high-speed damping, and the gas chamber stores energy for rebound while preventing cavitation. Together these features let the unit switch

smoothly between flow paths and damping modes, giving consistent, adaptable performance on both even and uneven roads under varying loads.

4.4.6 Validation of Simulation and Optimal Results

The simulation results of the redesigned suspension system were validated through both internal consistency with theoretical models and external benchmarking against industry practices. Internally, the spring deflection and damping behaviour matched expected analytical equations including Hooke's Law ($x = mg/k$) and the natural frequency formula $f_n = (1/2\pi)\sqrt{(k/m)}$. From these, the computed spring rate and damping coefficient, documented in Tables 4.3 and 4.7, produced a damping ratio of approximately 0.3, which falls within the optimal range for comfort and motion control in passenger vehicles (Mechanics & Industry, 2019).

Externally, the simulated coil spring stiffness (25-35kN/m) matched benchmark values such as the 35N/mm front spring rate of the Toyota GR Yaris, a vehicle with comparable dimensions and weight to the study's design reference (Toyota, 2023). Similarly, the modelled damper coefficient (300-400N·s/m) aligns with values used in validated quarter-car suspension models (Mechanics & Industry, 2019). The rebound-to-compression damping ratio used (~2:1) is also within the standard design range for light vehicle suspension systems.

The simulation applied a 180mm deep pothole as the input profile, which exceeds the Toyota Wish's ground clearance of 150mm and represents a realistic extreme based on local road conditions. This reflects industry norms, such as Ford's proving ground in Belgium which employs artificial potholes of 180-200 mm for durability testing at speeds up to 70km/h (Ford Motor Company, 2016), and Fiat Chrysler Automobiles' use of similar impact

simulations (FCA, 2016). These parameters ensure that full damper stroke, fluid throttling, and spring compression were captured under peak stress.

The rebound chamber pressure during simulation reached up to 3.75MPa, consistent with values documented for monotube high-pressure dampers under comparable dynamic conditions. Solver convergence was achieved through steady time steps and consistent energy behaviour across iterations, with no observed instabilities or nonphysical results.

In summary, the optimal results reported in the study are supported by both analytical theory and external industry standards. The modelled system behaves within physically realistic boundaries and is suitable for transition toward prototype fabrication and field validation.

4.5 Objective Four: To Assess the technical requirements for manufacture of the designed shock-absorber system within Uganda.

This section examined the technical and economic feasibility of Coil Spring and damper manufacturing in Uganda. Discussing the vital manufacturing processes involved while evaluating equipment capabilities and the potential for local manufacture and assemble. The following sections outline each stage of the process, the principles of DFMA, and cost modelling across different production scales.

4.5.1 Cold Winding Manufacturability of Ø14.4mm Cr-V Spring Wire

Cold coiling was selected for the redesigned spring because it matches the 14mm class wire diameters yet eliminates the furnace intensive hot-winding route. A survey of equipment available Globally confirmed that five-axis CNC coilers such as the WNJ TK-5200 can feed, bend and oil-quench CR-V wire up to 16mm. At the required 14.4mm diameter the forming torque is roughly 220Nm (see equation (4.12)) well inside the machine's >1,000Nm spindle rating, so the hardware clearance is more than four to one even before the usual 20% derating for continuous operation is applied.

$$\tau_f = \frac{\pi E d^3}{C} \tag{4.12}$$

$$= \frac{\pi * 207Gpa * 0.0144^3}{8.86} \approx 220Nm$$

Where: τ_f is forming torque per coil (Nm), E is the Young's Modulus of Cr-V steel (207GPa), d denotes 14.4mm and C represents Spring Index

Cold winding confers three production advantages that were reflected in the DFMA scorecard. First, it preserves surface hardness and carbon concentration because no scale forms during a heat up stage; this directly improves high cycle fatigue life, a critical metric for an MPV operating on Uganda's potholed roads. Second, it collapses the conversion route into a single cell in which coiling, in-line oil quenching, and conveyorized tempering run-in sequence; the furnace, roller hearth and descaling stations needed for hot winding are avoided altogether, trimming energy consumption. Third, real-time CNC feed back control holds pitch scatter within ±0.07mm, comfortably meeting ISO 7906-5 tolerances without manual re-work.

Local sourcing and downstream processes are also feasible. Roofings Group and Steel & Tube already import and draw wire rods, so raw material can be specified to ASTM A231 without foreign exchange on smaller billets. Because the TK-5200's quench bath, temper furnace and servo controls are integrated, a single four-operator cell can produce 700-750 finished springs per hour (31.5-49m/min), that can fully satisfy a domestic replacement market demand and neighbors. Most importantly, this route complies with Uganda's BUBU localisation policy, raw material, processing and quality assurance can all be executed locally, thereby delivering a fatigue resistant, cost-competitive coil spring that supports both the engineering and industrial goals of the project.

4.5.2 Oil Quenching and Heat Treatment

Immediately after cold coiling the wire is still in the austenitic condition, so a controlled quench-temper cycle is required to develop the tempered-martensite microstructure that gives Cr-V springs their high fatigue strength. Industrial practice calls for immersion in a mildly agitated oil bath held at ≈ 60 °C; this temperature provides a high enough cooling rate to cross the martensite-start line yet avoids the thermal shock and distortion often seen with cold oils. Metallographic data for Cr-V alloys place the martensite start **(**M_s**)** and finish **(**M_f**)** at roughly 325°C and 200ºC, respectively, meaning the quench must extract heat through that range in less than two seconds to prevent the formation of upper bainite. Programmable baths shipped with the TK-5200 coiler meet this requirement and allow the bath temperature and agitation to be logged for each batch, satisfying ISO 9001 traceability. The extent of transformation is governed by the Koistinen–Marburger relation as shown in Equation (4.12),

$$f_m = 1 - exp[-\alpha(M_s - T)], \alpha \approx 0.011 \qquad (4.13),$$

which predicts >98% martensite when the wire exits the bath at 50°C. A full martensitic matrix is desirable, but in this untempered state hardness sits at 56-57HRC and residual stresses approach 310MPa, levels that would embrittle the spring in service.

After the 60°C oil-quench, fatigue life is maximised with a duplex temper: one hour at 450°C drops hardness to the target 49–51 HRC and residual stress to roughly 150MPa, then a 20-minute soak at 180 °C relaxes stresses to ≈ 120MPa, removes more than 80% retained austenite and stabilises coil geometry. International data show this two-step regimen improves endurance by 30–40 % over a single temper thanks to a uniform tempered-martensite structure (Becker, 1967),(Zhang et al., 2018).

Although Uganda lacks dedicated spring shops, the process can still be adopted. Compact batch or conveyor tempering furnaces operating in the 400-500°C band are commercially

available and require only ±2°C controllers and inert-gas purge for Cr-V work. Hardness, dilatometry and microstructural checks can be carried out at Kyambogo University, Makerere University, UNBS or UIRI. Thus, the quench-tempering cycle integrates readily with the proposed cold-winding cell and can be qualified to ASTM A231 using existing national laboratory resources.

4.5.3 Post-Forming Processes for Enhanced Spring Performance

Post-forming processes such as shot peening, end grinding, pre-setting, and powder coating present a technically feasible path to improving the designed spring durability and service life. Shot peening introduces beneficial compressive residual stresses that delay fatigue crack initiation and extending service life. Fatigue testing demonstrated a 38% increase in fatigue life for peened samples, consistent with the 30–50%, with best results achieved using double wheelabrators and sequencing the process after scragging to retain the stress layer (Scuracchio et al., 2013). Pre-setting which involves applying a compressive load 5% above the spring's maximum working load is carried out to induce controlled plastic deformation, resulting in a significant reduction in height loss from 5.2mm to 1.1mm after 100,000 load cycles (Smalley, 2025). Finally, the application of powder coating enhances corrosion resistance, with coated samples surviving up to 240-hour neutral salt spray testing with less than 2% red rust, and this outperforms epoxy-coated alternatives (Roberto, Alessandro, & Robertino, 2014). While such processes are not yet employed locally, their adaptations is achievable within Uganda's growing manufacturing capabilities leveraging on the fact that technical expertise and labour is present and are beneficial for ensuring long-term spring performance.

4.5.4 Coil Spring DFMA Considerations

The design has been meticulously designed to incorporate DFMA principles; Local manufacturers can already hit the tolerances as in ISO 7906-5:2004 that matter for quality

springs: the TK-5200 coiler holds ±0.05mm wire-feed accuracy and keeps coil-to-coil pitch scatter within 0.07mm, both comfortably tighter than the 0.02–0.04 mm end-flatness window and the 0.10 mm pitch variation. (WNJ, 2025). In service, the spring-and-damper module can be removed with ordinary coil-spring tools and just two spanners, so a mechanic can complete the job in minutes and keep vehicle downtime low. On the factory floor, all heat-treating, peening and coating steps can fit in a U-shaped cell of about 100m² that operators can run at roughly 700-750 finished springs per hour. Quick-change guides let the TK-5200 switch wire sizes in under 10 minutes, and because cold winding eliminates a gas-fired pre-heat furnace it saves energy per spring.

The design also cuts part count to a single spring and relies almost entirely on Ugandan supply chains. Domestic mills such as Roofings and Steel & Tube can deliver chromium-vanadium wire, while fuel companies like Vivo Energy and Total Energies supply quench oils blended to the required flash points. Hardness, dilatometry and metallography checks are available at UNBS, Makerere University and the Uganda Industrial Research Institute, meaning every step of validation, from raw steel to finished part, can be completed inside the country.

4.6.5 Cost Model and Economy of Scale Volume Effect

The costing model starts with a single 14.4mm Cr-V spring weighing 3.1kg. Cr-V wire is quoted at USD 1.5 per kg by Nantong Jinrui Metal Products Co., Ltd (Focus Technology Co., 2025). A 3.1kg spring therefore carries USD4.65 direct material. Including 10% process scrap (shear tails, setup coils) raises material cost to USD5.12. Setting the machine at 35m/min wire feed, this meant Energy usage for the cold line is 0.197kWh per spring for both coiling and quenching taking into account the Total Power rating of machine as 145KWh and assuming 85% machine efficiency. Other process assumed to cost 0.25kWh

for double temper, shot peen and powder cure. At the industrial tariff of UGX 452.1 per kWh the energy bill is UGX202 per spring.

Labour covers two operators paid UGX1,500,000 monthly each. The WNJ-TK5200 can produce 735 springs per hour at a wire feed of 35m/min. Working two shifts of 8 hours per day. If employees worked 24 days per month, this implies a direct labour cost per hour of UGX7,813, translating into a direct labour cost per spring of UGX11. Thus, the cost per spring can be estimated.

Consumables include 0.15 kg of SAE-angular steel shot and 0.10kg of TGIC polyester powder per spring, along with cutting wheels, with a combined cost of UGX1,850 per unit. Capital charges are based on a UGX 550 million investment in twin-wheel peening equipment, powder coating booths, and dedicated fixturing.

Depreciation is applied using a 15 % annual straight-line method, consistent with asset devaluation rates found in non-OECD countries (Yisheng, 2006). To capture indirect costs not individually metered, such as maintenance, QA, rent, and utilities, a 20 % factory overhead is added to the direct production costs. The exchange rate used throughout is UGX 3,800 to USD 1.00.

The cost model evaluates three monthly production scenarios: 500, 8000, and 282,000 springs, the latter represented full-capacity output across two shifts and whose results are presented in Table 4.12

Table 4.12: Three-monthly production scenarios of Coil Spring to Predict Minimum Feasible Production levels

	Cost of One Spring (UGX)		
Production Scenarios	**500 Springs/month**	**8,000 Springs/month**	**282,000 Springs/month**
Material (Inclusive. 10 % scrap)	19,440	19,440	19,440
Energy	202	202	202
Labour	6,000	375	11
Consumables	1,850	1,850	1,850
Depreciation	13,750	859	24
Direct Cost	**41,242**	**22,726**	**21,527**
Factory Overhead (20 %)	8,248	4,545	4,305
Unit Cost (UGX)	**49,490**	**27,272**	**25,832**
Unit Cost (USD)	**13.02**	**7.18**	**6.8**

NB: Actual commercial production volumes and costs may vary slightly to accommodate demand and maintenance scheduling.

4.5.6 Economies of Scale Discussion

The cost model clearly demonstrated the impact of economies of scale on unit production cost across different monthly outputs. At a low production level of 500 springs monthly, the unit cost stands at UGX 49,490 (USD 13.02), which is significantly higher than at larger volumes. This is primarily due to the high burden of labour and capital depreciation spread over fewer units. Labour alone contributes UGX6,000 per spring, while depreciation reaches UGX13,750, accounting for over 40% of total direct cost. The overhead component further compounds this cost.

In contrast, at 8,000 springs per month, the unit cost drops markedly to UGX 27,272 (USD 7.18). This reduction is driven by improved dilution of fixed costs across a broader output base. Labour input reduces to UGX375 per spring, while depreciation falls to UGX859 per spring. The material, energy, and consumables, which remain constant per unit, now

dominate the cost structure, showing the flattening of the variable cost curve. At this level, unit economics become competitive with imported alternatives, particularly those priced between USD8-9 per unit F.O.B cost, validating the viability of local production.

At full capacity (282,000 springs/month), representing maximum output across two shifts, the unit cost further converges to UGX25,832 (USD6.80). Here, labour and depreciation costs become negligible, each contributing only UGX11 and UGX24 per spring, respectively. This production volume approaches the theoretical cost floor defined by material and core processing costs. Fixed costs are fully diluted, and the overhead burden per unit is minimized. As a result, over 75% of the unit cost now originates from raw material and energy, indicating that further cost reductions would need to focus on supply chain efficiency or raw material localization.

Overall, the model underscores the critical role of scale in achieving cost competitiveness. The sharp cost decline from 500 to 8,000 units illustrates the importance of exceeding breakeven throughput levels. Beyond this point, the cost advantage plateaus, and the unit cost becomes relatively inelastic to volume increases. Therefore, strategic planning should prioritize securing minimum monthly volumes above 8,000 springs to consistently out compete import prices and maximize capital productivity.

4.5.7 Damper Manufacturing Assessment

Uganda's aftermarket currently depends on imported dampers pricing between UGX150,000 and UGX250,000 a piece for light weight passenger vehicles. By outsourcing the machining intensive cylinder and end-cap to a qualified Kampala vendor and reorganising the remaining value adding steps into a balanced, high-throughput flow line, a domestic plant can realise a unit cost of roughly UGX 50,000. The next sections present the prospected production layout, the design for manufacture and Assembly considerations, the cost-build model, the resulting economics and the strategic implications of localising this component.

4.5.8 Local Manufacturability of Cylinder and End Cap

Local workshops can machine the damper's three structural pieces, the cylinder tube, welded bracket and threaded end-cap, well within the required limits: bores hold ±0.03mm, face flatness stays inside ±0.05mm and the EN8 end-cap is threaded to a 6g/6H metric fit. Using standard TIG welding with 2.4mm ER70S-6 filler, these parts can be produced and assembled at scale from steel sourced at domestic mills, making the housing fully manufacturable in Uganda.

4.5.9 Justification of Damper Imported Parts

The piston rod and shim stack impose dimensional and surface-finish requirements, Ra< 0.2μm, HRC ≥ 60, and ±10μm concentricity on 0.1-0.3mm shims, that can only be met with centre-less grinding, hard-chrome plating, laser cutting and flat-lapping cells (Boker's Inc, 2025). Uganda currently lacks this equipment and, given the limited domestic volume for passenger car dampers, investing in such plant would create a long payback, under utilised asset. Sourcing rods, shims and seal kits from established Asian suppliers (China, India or Taiwan etc.) therefore avoids sunk capital while still allowing local assemblers to customise valve stacks on a just-in-time basis. The hybrid strategy preserves quality because the most tolerance-critical parts are produced in facilities already certified to ISO/TS 16949 and channels local investment into mid tolerance machining where Ugandan workshops and expertise can be competitive.

4.5.10 Damper Manufacturing Process and Plant Layout

Plant layout to be set up as flow line with three operators across two parallel work cells running two eight-hour shifts per day considered in this study. Finished cylinders and threaded end-caps arrive pre-gauged; Operator 1 performs a rapid dimensional verification, lubricates the rod seals and pre-loads the circlip. Operators 2A and 2B work at mirrored benches, each completing a full shim-stack build, inserting a hardened chrome-plated

piston rod ($Ra < 0.2\mu m$, HRC60) and torquing both piston nut and end-cap within a three-minute cycle using preset torque wrenches. Operator 3 then pressurises the assembled damper to 0.8MPa using reclaimed nitrogen, performs a helium-sniff leak test and immerses the housing in a zinc-phosphate bath that replaces a traditional powder-coat oven, cutting cure time and energy. When these stations are balanced to a 1.5minute test, the system outputs 40 dampers per hour, equivalent to approximately 24,000 units per month at twenty-four working days. Different flow lines can be set up to cover high peak order seasons.

4.5.11 Damper DFMA considerations

Local machine shops at UIRI, Kyambogo and similar facilities already hold the accuracy needed for the damper's steel parts, bore tolerances are maintained within ± 0.03 mm, thread-pitch and alignment error stay below 0.05 mm, and the tube's cylindricity is kept under 0.07 mm along a 350 mm length. These figures ensure the piston moves freely and that the oil-and-nitrogen charge remains sealed during high-pressure operation, eliminating the need for imported high-precision equipment.

Assembly is deliberately fast and tool light. All major internals drop in from the top of the tube and self locate, so a technician needs only a circlip-plier, a 12mm open-box spanner and an adjustable torque wrench to complete the job. With this layout, one unit can be built or stripped and rebuilt in about 5 minutes on the bench, and roadside servicing (seal or shim changes) can be finished in under 15 minutes. The design contains just five primary components and relies on a single M18×1.5 thread family, trimming inventory and virtually eliminating orientation errors because washers, carriers and retaining rings are radially symmetric.

Production infrastructure is equally lean. The damper can be clamped in standard V-blocks, so no dedicated fixtures are required for threading, seal preload or leak-testing, and it shares

powder-cure ovens, press-fit jigs and nitrogen rigs already installed for coil-spring work. Because the housing accepts multiple shim-stack and seal options, manufacturers can offer on-road, sport or off-road variants without re-machining the shell, and vertical filling/charging prevents trapped air while speeding nitrogen charging. Together, these numbers and features cut capital spend, shorten change-over times and give Uganda's workshops a rugged, rebuildable product that fits the region's maintenance style.

4.5.12 Damper Cost Model

All cost elements are calculated on a per damper basis and this was done to enable comparative basis with imported dampers. The cylinder and end-cap are secured under a blanket order at UGX15,000 per set, reflecting vendor-owned tooling and SAE 1020 material. Hardened piston rods are imported at UGX4000 each, while bulk seal kits and floating pistons cost UGX10,000 per unit at a 1000MOQ. A shim-stack valving kit priced at UGX8,000. Energy consumption averages 0.2 kWh per damper, costed at the medium-industrial tariff of UGX452.1 per kWh. Consumables include angular steel shot for peening and zinc-phosphate chemistry, totalling UGX600. Labour is allocated at UGX150 per unit by dividing a composite wage bill of 4.5 million shillings across the monthly volume. Depreciation is derived from a fifteen-percent annual rate on UGX550 million of fixtures and dip-tank assets, yielding UGX400 per damper. Factory overhead is lean-allocated at eight percent of direct cost, while a fifteen-percent contingency safeguards against raw-material or exchange-rate volatility since most parts apart from cylinder and end cap are imported.

Table 4.13 contains the costing the breakdown that result into the projected unit damper cost.

Table 4. 13: Costing of Unit Damper

Element	**Cost Per Damper**
Outsourced cylinder & end-cap	15,000
Hardened piston rod	4,000
Seal kit & floating piston	10,000
Shim-stack valving kit	8,000
Energy	90
Consumables	600
Labour	150
QA + N_2 leak test	1,000
Depreciation	400
Subtotal	**39,240**
Factory overhead (8 %)	3,139
Base unit cost	**42,379**
Contingency (15 %)	6,357
Projected unit cost	**48,735**

Overhead=0.08×Subtotal, Projected Cost= (Subtotal plus Overhead) ×1.15

4.5.13 Discussion of Damper Costing Results

The projected unit cost of about UGX 50,000($13.16) is within the range of F.O.B price of imported dampers at a range of $9-$15, when taxes, Insurance and Freight are included at Delivery Duty Paid, the cost is more likely to double. This gives the locally made damper a cost advantage on top of it customized feature performances even after applying a fifteen-percent contingency. A material heavy structure persists, hardware accounts for nearly three quarters of spend, so additional savings will depend on localising piston-rod plating or seal manufacture. Unlike for coil springs, with damper throughput remains the critical variable, halving monthly volume to twelve thousand units would lift labour, depreciation and overhead by only about three thousand shillings per unit, leaving a generous cushion versus import prices. Incremental capital for the zinc-phosphate dip system,

nitrogen-gas booster and shim-stamping press may not necessarily cause a big change in costing. Quality benchmarks are retained; the zinc-phosphate finish satisfies corrosion-life requirements and the shim-stack maintains the rebound-to-compression ratio specified in the design.

4.5.14 Integrated Plant Layout for the Spring-Damper System

Figure 4.15 presents the proposed Plant floor arrangement that unifies coil-spring and monotube-damper production under one roof while respecting the lean, high-throughput principles established in the preceding cost and DFMA analyses. Raw materials enter a central receiving zone, are verified, and then flow into two parallel value streams. On the left, chromium-vanadium wire follows a five-step route; uncoiling, CNC coiling, in-line oil quench and double temper, shot peening, and pre-setting/end-grinding, before converging at the shared powder-coating booth. This cell may occupy roughly 450m² and, with key workers, the production expectations can be achievable.

Figure 4.15: Schematic Proposed Integrated Damper-Spring Plant Layout

The right-hand stream handles damper housings. Damper Cylinders and End caps are checked prior to gas filling and leak testing. A dedicated station then mates the imported piston rod, shim stack, floating piston and seal kit, after which units proceed through the same powder-coating booth used by the springs.

Positioning Quality Control between the two streams allows Quality Control staff to sample both products without travel waste, while the shared coating oven and curing line maximise equipment utilisation and compress capital payback. The bidirectional arrows highlight feedback loops for real-time defect containment: any dimensional out of spec immediately routes the part back to CNC adjustment or re-grind, preventing downstream scrap thus adhering Total Quality Management principles. Overall, the layout translates the study's DFMA findings, low part count, self-locating features and minimal fixture needs, into a compact, scalable plant that supports mixed lot production for both springs and dampers with minimal labour and energy overhead.

4.6. Comparative Assessment between the Original shock absorber and the redesigned shock absorber.

The purpose of this comparison was to evaluate how the redesigned shock absorber system improves upon the original Toyota Wish OEM shock in meeting the study's objectives. Key design parameters, material choices, spring/damper characteristics, and simulation outcomes are compared side-by-side to highlight specific improvements. This assessment as shown in table 4.14 ties back to the objectives by showing whether the redesign addresses the original system's shortcomings while remaining within acceptable industry benchmarks.

Table 4.14: Comparative Assessment between the Original shock absorber and the redesigned shock absorber

Aspect	Original Toyota Wish Suspension	Redesigned Spring–Damper System	Comment
Spring rate, k	Estimated 25-28 kN/m (typical front-corner rates for compact MPVs; Hrovat, 1997; Li et al., 2018).	33.7kN/m in main working region; rises toward ≈51kN/m at bump-stop engagement (progressive behaviour).	New rate remains within the 25-40kN/m band reported for comparable vehicles but provides higher support for elevated loads and a 180mm pothole event without excessive sag.
Maximum working shear stress & fatigue safety	Typical designs target $\tau \approx 550–650$MPa with FoS ≈1.2 on yield for standard highway duty (Konieczny et al., 2016).	Peak shear ≈405 MPa with FoS ≈ 1.57 against allowable shear; buckling safe (L_f = 0.342 m ≪ 0.671 m critical).	Redesigned spring operates well below the usual high-cycle fatigue limits for Cr-V alloys, increasing life under Ugandan rough-road loads.
Damping coefficient & ratio (body mode)	OEM twin-tube units typically give $\zeta \approx 0.2–0.25$ for comfort on paved roads (Li et al., 2018). Compression < rebound but tuned for smoother profiles.	Monotube damper sized for $\zeta \approx 0.30–0.35$ in body mode, with rebound damping ≈1.5–2× compression and digressive F–v curve (≈3.1–4.0kN peak forces over test velocities).	Increased ζ and stronger rebound are consistent with rough-road recommendations, improving decay of oscillations after pothole impact while retaining comfort at low speeds.
Internal pressure behaviour	OEM data not public; typical peak working pressures ~2–3MPa for light vehicles (Li et al., 2018).	CFD shows compression chamber rising from 0.8MPa gas pre-charge to ≈2.7 MPa under full compression; rebound side ≈3.4 MPa peak. No cavitation or unstable pressure zones observed.	Pressures fall within published ranges for gas-charged monotube dampers, confirming that valve sizing and piston area are realistic and structurally safe.
Dynamic response to 180 mm pothole	Field experience on Ugandan roads shows frequent bottom-out, oil leakage and rod bending, indicating insufficient travel and damping for deep defects.	Quarter-car simulation: wheel vertical velocity peaks ≈2.5 m/s after impact and decays to ~0 m/s within 0.4–0.5 s; bottom-out is avoided and tyre contact is maintained.	The redesigned system meets recommended criteria of rapid decay and limited overshoot for rough roads (Hrovat, 1997), reducing risk of loss of grip and component damage on unpaved potholed roads
Ride comfort & handling	Tuned primarily for highway comfort; on severe potholes, high body acceleration	Higher main-rate spring plus stronger, digressive damping reduce residual oscillations and body	Simulated body acceleration levels and decay trends are in line with comfort bands reported in quarter-car

	and secondary oscillations are commonly reported by users.	motion while still allowing small deflections to pass through bleed/low-speed circuits.	studies for $\zeta \approx 0.3$ (Li et al., 2018).
Configuration & robustness	OEM twin-tube, smaller piston, limited gas volume; more prone to aeration and fade under repeated high-stroke events.	45.3 mm-piston gas-charged monotube with shim-stack valving; better heat dissipation and resistance to aeration/fade under repeated pothole hits.	Monotube architecture and shim-stack control are widely recommended for high-duty or off-road applications (Zhifei et al., 2021).
Manufacturability & unit cost (springs)	Fully imported. Typical aftermarket spring cost ≈USD 15–20 (UGX ≈57,000–76,000) at retail in Uganda.	Cold-wound Cr-V coils: modelled unit cost ≈UGX 27,272 at 8,000 springs/month and ≈UGX 25,832 at 282,000 springs/month.	At ≥8,000 units/month, local spring cost undercuts imported pieces while meeting ASTM A231 and ISO 7906-5 tolerances, supporting BUBU policy.
Manufacturability & unit cost (dampers)	Imported aftermarket dampers typically UGX 150,000–250,000 per unit retail.	Hybrid model: local manufacture of cylinder and end-cap with imported rod, shims and seals; projected base unit cost ≈UGX 48,735.	Even after allowing for overheads and contingencies, local assembly remains below landed retail prices, especially once taxes and margins on imports are considered.

CHAPTER FIVE: CONCLUSION AND RECOMMENDATIONS

5.1 Conclusion

This project successfully re-designed a telescopic shock absorber system for a Passenger light car, to improve performance on uneven roads. A developed 6-active turn Coil Spring of wire diameter 14.4mm and free length 342mm made of Chromium-vanadium steel proved that its high spring rate of 33.7 $\times 10^3$N/m is capable of handling and tolerating more weight while maintaining sufficient ride height and stability. Simultaneously, a damper of 150mm stroke, peak force of 3.12KN (Rebound) and 1.58KN(Compression) was developed with a tuned valve configuration system and damping coefficient of 0.35 sufficient to stabilize sudden impacts. The simulations of the duo confirm that under highly demanding conditions the new shock absorber system meets performance criteria for load capacity, structural integrity and in addition, compression chamber pressure rise from an initial 0.8 MPa gas pre-charge to approximately 2.5 MPa at full compression stroke, and reaches over 3.75 MPa during rebound validates its high damping efficiency. Furthermore, Quarter-car dynamic simulation findings demonstrate enhanced ride dynamics as a result of vibrations distributions maintaining tyre contact and vehicle stability on uneven ground. Feasibility studies on local Manufacturability of the new shock absorber system indicate that producing a minimum monthly volume of 8,000 springs would consistently out compete import prices and maximize capital productivity.

5.2 Recommendation

First, experimental validation is absolutely important, a prototype of the re-engineered shock absorber has to be built and tested under several conditions to support the simulation findings. Real-world road tests on uneven terrain will validate the performance and dependability of controlled studies including dynamometer assessments for damping force and fatigue rigs for spring longevity.

Verifying the shock absorber's efficacy across several driving circumstances and identifying any practical issues (like seal degradation or fluid aeration) that simulations may not sufficiently expose depend on this empirical testing. The simulation models can be improved using later real-world validation data, hence improving accuracy in next designs.

Thermal control is now quite important, the damper may overheat over prolonged, heavy use. Therefore, including cooling systems, such heat sinks or cooling fins on the shock body, will help heat dissipation and prevent performance degradation due by overheating.

The Government of Uganda should increase funding and make strategic decisions which among others is not taxing precision machinery that are vital in machining to acceptable manufacturing tolerances. Overall, it is recommended to progress this reengineered system from the digital and prototype stages to full implementation for broad technical applications. Following these guidelines, thorough testing, thermal, weight and material optimisation will enable the shock absorber redesign to be practically realised, so improving ride comfort and durability for light vehicles and supporting safer, more resilient suspension systems in the automotive industry.

REFERENCES

Amati, N., Andrea, F., & Tonoli, A. (2011). Design of electromagnetic shock absorbers for automotive suspensions. Vehicle System Dynamics, 1913-1928.

Anthony, B., & Thomas, M. (2015). The Last Frontier: Prospects and Policies for the Automotive. Johannesburg: TIPS Annual Forum.

Arrivealive. (2012, September 14). Gabriel South Africa celebrates 50 years as a local manufacturer of shock absorbers. Retrieved from Arrivealive: https://www.arrivealive.mobi/news.aspx?s=3&i=8572&name=gabriel-south-africa-celebrates-50-years-as-a-local-manufacturer-of-shock-absorbers#

Ashwini, B. A. (2021, February 19). Shock absorber design and analysis for off road race car. Materials Today: Proceedings, 1-2.

Assaad Al, S., Khaleel, H. H., & Khashan, M. K. (2018). Design and analysis of coil spring in vehicles using finite elements method. International Journal of Mechanical and Production, 615-624.

Azuma, T. (2024, February 17). How Long Do Shock Absorbers Last? Retrieved from CarFromJapan: https://carfromjapan.com/article/car-maintenance/how-long-do-shock-absorbers-last/

Bae, J.-S., Hwang, J.-H., Roh, J.-H., & Yi, M.-S. (2015, 09 24). Development of an electromagnetic shock absorber. International Journal of Applied Electromagnetics and Mechanics, 157-167. doi:10.3233/JAE-150033

Baiyang, S., Wei, D., & Jian, Y. (2023). Performance enhancement of vehicle suspension system with geometrically nonlinear inerters. Archive of Applied Mechanics, 94, 1. doi:10.1007/s00419-023-02502-4

Benn, E., Alan, G., & Vijaya, R. (2008). The Cost of Doing Business in Africa: Evidence from Enterprise Survey Data. World Development, 1531-1546.

Bin, Y., Wang, Z., Guoye, W., Jie, Z., J. Z., & Zhou1, L. (2019). Investigation of the suspension design and ride comfort of an electric mini off-road vehicle. Advances in Mechanical Engineering, 1-10.

Bogie, A. (2014, February 12). Shock absorber defects 'third most common' technical cause of road accidents – Bilstein. Retrieved from Tyre Press: https://www.tyrepress.com/2014/02/bilstein-shock-absorber-defects-third-most-common-technical-cause-of-road-accidents/

Boker's Inc. (2025, May 01). Custom Shim Stacks for Diverse Industry Applications. Retrieved from Boker's Inc, Spring and Washer Specialist: https://www.bokers.com/washers/custom-washers/non-standard-flat-washers/shims/custom-shims/shim-stacks/#:~:text=Boker%E2%80%99s%20valve%20shim%20stacks%20feature,ranging%20from%20simple%20to%20complex

Bose, C., Rajasimman, V., & Prabu, R. G. (2020). Design and Manufacturing of Leaf and Coil Suspension. International journal of research in engineering, science and management, 3. doi: https://doi.org/10.47607/ijresm.2020.291

Choon-Tae, L., & Byung-Young, M. (2004). Simulation and experimental validation of vehicle dynamic characteristics for displacement-sensitive shock absorber using

fluid-flow modeling. Proceeding of Mechanical Systems and (pp. 373–388). Korea : Mechanical Systems and Signal Processing.

Clifton, S., Sampath, S. S., & M. Chithirai, P. S. (2017, June). Investigation on Structural Analysis of Composite Springs – A Review. Amity Journal of Engineering and Technology, 2(1), 1-9.

D.Mohankumar, Sabarish, R., & PremJeyaKumar, D. M. (2018). VARIABLE DAMPING FORCE SHOCK ABSORBER. International Journal of Pure and Applied Mathematics, 118(18), 945-955.

Daniel, B., & Grzegorz, N. (2021). MODELLING THE SHOCK ABSORBER PISTON VALVE USING 2-WAY FLUID-STRUCTURE INTERACTION. TRANSPORT PROBLEMS, 16(4), 46-57. doi:10.21307/tp-2021-059

Darko, P., Goran, V., & Bozic c, Z. (2019, May). Coil spring failure and fatigue analysis. Engineering Failure Analysis, 99, 310-318. doi:https://doi.org/10.1016/j.engfailanal.2019.02.017

Dixon, J. C. (2007). The Shock Absorber Handbook. Great Britain: John Wiley and Sons, Ltd.

Farah, Z. R., & Fadly, J. D. (2019, March). The effect of hydraulic damper characteristics on the ride and handling of ground vehicle. International Journal of Recent Technology and Engineering (IJRTE), 7(6S), 113-114. Retrieved April 23, 2024, from https://www.ijrte.org/wp-content/uploads/papers/v7i6s/F02240376S19.pdf

Focus Technology Co., L. (2025, May 11). Nantong Jinrui Metal Products Co., Ltd. Retrieved from ntjrxu.en.made-in-china: https://ntjrxu.en.made-in-china.com/

George E. Dieter, L. C. (2013). ENGINEERING DESIGN (5th ed.). (M. Lange, Ed.) New York, United States: McGraw-Hill. doi:ISBN 978-0-07-339814-3

Gonera, J. (2020). Influence of the Size and Distribution of Load on the Damping Coefficient of Shock Absorbers in Passenger Vehicles. Advances in Science and Technology Research Journal, 185-195.

I M, R., & Pozdeev, A. V. (2019). Method for determining the shock absorber effectiveness in . IOP Conference Series: Materials (p. 2). Russia: IOP Conference Series.

Issifu, I., Jacob Kwaku, N., Baba, Z., & Abdul-Hamid, M. (2023, January). Analysis of the Material Properties of Vehicle Suspension Coil Spring. World Journal of Engineering and Technology 11(04):, 11(4), 827-858.

Jain, S. C., Pushpendra, K. S., & Dhara, V. (2014). MCPHERSON SUSPENSION SYSTEM -A REVIEW. International Journal for Technological Research in Engineering, 2347-4718.

Jihao, D. (2020). Performance analysis of independent suspension coil spring. Journal of Physics Conference Series, 012052.

Jue, W. (2023). Characteristics, application fields, and future development and challenges of shock absorbers. Highlights in Science, Engineering and Technology, 75, 203-208. doi:10.54097/fhjb9342

Kaganzi, P. D. (2021, January 14). Between a Premio and Wish, which is better for Uber operations? Retrieved from Daily Monitor: https://www.monitor.co.ug/uganda/business/auto/between-a-premio-and-wish-which-is-better-for-uber-operations--3257740

Kirunda, B. E. (2017, 06 16). Body weight and Physical Activities of Adults in Uganda. Norway: University of Bergen.

Kuew, W. C., & Yong, Y. R. (2013). Electric vehicle energy harvesting system regenerative shock absorber for electric vehicle. 2013 IEEE Conference on Sustainable Utilization and Development in Engineering and Technology (CSUDET) (pp. 7-10). Selangor, Malaysia: IEEE. doi:10.1109/CSUDET.2013.6670989

Lalitkumar, J., Shankar, S., & Sawant, S. M. (2016). Mathematical modelling and experimental validation of mono-tube shock absorber. World Journal of Engineering , 294-299.

Lukas, S., & Johannes, W. (2022, April). Fluid–structure interaction and dynamic stability of shock absorber check valves. Journal of Fluids and Structures, 110(2), 2-20. doi:10.1016/j.jfluidstructs.2022.103536

Lundberg, J. (2021). Design and evaluation of a regenerative shock absorber. Luleå, Sweden: Luleå University of Technology.

Manga, H., Elumagandla, S., & Nalla, S. (2018, August). Design and Analysis of Shock Absorber. International Journal of Innovative Science and Research Technology, 3(8), 420. Retrieved 2024

Mario, H., Wilhelm, D., Anton, G., & Johann, L. (2013). Integrated Computer-Aided Design in Automotive Development. Berlin: Springer. doi:10.1007/978-3-642-11940-8

Matovu, M. (2024, April 25). reports-call-for-policy-overhaul-to-address-underutilised-capacity-in-manufacturing-sector. Retrieved from Nile Post:

https://nilepost.co.ug/news/197147/reports-call-for-policy-overhaul-to-addressa-underutilised-capacity-in-manufacturing-sector

Milliken, W. F., & Milliken, D. L. (1994). Race Car Vehicle Dynamics R-146. In W. F. Milliken, Race Car Vehicle Dynamics R-146 (p. 918). USA: SAE International.

Mwenda, A. (2023, February 18). The Kampala roads disaster. The Independent , p. 1.

Namagembe, S. (2024). concern-as-skills-mismatch-worsens-uganda-s-job-crisis. Retrieved from Daily Monitor: https://www.monitor.co.ug/uganda/news/national/concern-as-skills-mismatch-worsens-uganda-s-job-crisis-5023954#story

Ndagano, A. (2022, October 09). UG@60: The Journey of Ugandas' Road Network. Retrieved from The New Vsion: https://www.newvision.co.ug/category/Independence/ug60-the-journey-of-ugandas-road-network-NV_144734

Nicholas, S. G., & Adesanmi, A. (2021). Effect of Mesh Density on Finite Element Analysis Simulation of a Support Bracket. FUOYE Journal of Engineering and Technology, 34-37.

Nikolay, P. (2017). Influence of shock absorber temperature on vehicle ride comfort and road holding . BulTrans-2017 – 9th International Scientific Conference on Aeronautics, Automotive and Railway Engineering and Technologies (p. 6). Bulgaria: EDP Sciences. doi:10.1051/matecconf/201713302006

Osama, E., Sallam, M., Almazy, K., & Maryama, O. (2017). Effect of Heat Treatments on the Mechanical Properties of DIN 50Cr3 Spring Steel. Journal of Engineering Science and Military Technologies 17(17):1-15, 1-5.

Pacejka, H. B. (2006). Tyre and Vehicle Dynamics (Vol. 2). Amsterdam, Netherlands: Elsevier.

Pavlenko, A. (2024, 11 21). Posted inSuspension Construction. Retrieved from New Kids Car: https://www.newkidscar.com/suspension-constructio/macpherson-strut-suspension/

Pavlov, N. (2017). Influence of shock absorber temperature on vehicle ride. MATEC Web of Conferences (p. 1). Sofia, Bulgaria: Matec Conferences. doi:DOI: 10.1051/matecconf/201713302006

Pinjarla, P., & Lakshmana, K. (2018, May 11). DESIGN AND ANALYSIS OF A SHOCK ABSORBER. International Journal of Research in Engineering and Technology, 576-579.

Piotr, C., Damian, S., & Pawel, S. (2010, January). Static validation of a model of a disc valve system used in shock absorbers. International Journal of Vehicle Design, 53(4), 2010. doi:10.1504/IJVD.2010.034104

Prasad, K., & Ajaykumar, U. (2021). INFLUENCE OF SPRING STIFFNESS IN AUTOMOTIVE SUSPENSION SYSTEM PERFORMANCE – AN OVERVIEW. International Research Journal of Engineering and Technology, 1514-1517.

Prashant, M., & Aitavade, E. N. (2014). Modification of Mono-Tube Shock Absorber. International Journal for Scientific Research & Development, 348-351.

Raijade, S. B., & Seshagiri Rao, G. (2015). Study of Dynamic Characteristics of Helical Spring of Variable Wire. International Journal of Current Engineering and Technology, 1926-1933.

Roberto, C., Alessandro, M., & Robertino, C. (2014). IMPROVING CORROSION RESISTANCE OF Powder Coating Systems for ACE Systems. Atlanta : 2014 American Coatings Conference.

Saad Bin, A. K., M A, C., T A, C., N, S., M, E., & Nagarajah, R. (2025). Study and Comparison on Linear Electromagnetic Shock Absorbers among other Available Intelligent Vibration Dampers. International Journal of Science and Research, 2319-7064.

Siddharth, Dipender, Y., & Surabhi, L. (2021). Design development and analysis of cylindrical spring with variable pitch for two wheelers. Materials Today; Proceedings (pp. 3105-3111). Delhi, India: www.elsevier.com/locate/matpr.

Simon, K. k., & Festo, A. (2020). Performance Effects of Shock Absorber and Spiral Springs Against Vertical Vehicle Expenses Weighing the Road Structure. INTEK Jurnal Penelitian, 79-84.

Smalley. (2025, 5 11). Spring Design Performance. Retrieved from Smalley, The Engineers' Choice: https://www.smalley.com/spring-design/performance

Spiteri, S. (2019). Shock Absorber Applications. European Journal of Engineering and Technology, 37-41.

Talbott, M., & Starkey, J. (2002, 01 13). An experimentally validated physical model of a high. SAE Technical Paper, 5-12.

Tang, G. L. (2014, 04 01). SAE Mobilus. Retrieved from Society of Automobile Engineers: https://www.sae.org/publications/technical-papers/content/2014-01-0051/

Teerapharp, A., Sittikorn, L., Szathys, S., & Masaaki, O. (2014). Physical Characteristics of Twin-Tube Shock Absorber. SAE International Journal of Passenger Cars - Mechanical Systems-V123-6, 375-381.

Tevema. (2022). Understanding DIN 2095 Tolerances. Retrieved from Tevema Technical Springs: https://www.tevema.com/mastering-din-2095-tolerances-our-guide-to-spring-precision/

Tradewheel. (2025). Strip Steel for Shock Absorber Shims. Retrieved from Tradewheel: https://www.tradewheel.com/p/strip-steel-for-shock-absorber-shims-1184993/

Urszula, F., & Jan, Ł. (2012). Modeling and analysis of a twin-tube hydraulic shock absorber. Journal of theoretical and applied mechanics, 627-638.

Urszula, F., & Jan, Ł. (2012). Modeling and analysis of a twin-tube hydraulic shock absorber. Journal of theoretical and applied mechanics, 627-638.

Urszula, F., & Jan, L. (2020). A comparative analysis of mono-tube shock absorbers with different valve systems. 3rd National Conference On Current And Emerging Process Technologies – Concept 2020, (p. 020010).

Vidhyathar, S. (2019, March 06). Design Evaluation of a Two-Wheeler Suspension. International, 5(3), 2.

Wang, J. (2023). Characteristics, application fields, and future development and. Highlights in Science, Engineering and Technology, 75, 2-3.

Więckowski, D., Dąbrowski, K., & Ślaski, G. (2018). Adjustable shock absorber characteristics testing and modelling. IOP Conf. Series: Materials Science and Engineering 421 , 22039. doi:10.1088/1757-899X/421/2/022039

WNJ. (2025, May 11). TK-5200 5AXES CNC SPRING COILING MACHINE. Retrieved from wnjspringmachine: https://www.wnjspringmachine.com/product/products-tk-5200-6-type.html?utm_

Xiayi. (2015). Shock Absorber Parts. Retrieved from Shockabsorberparts: https://www.shockabsorberparts.com/supplier-286474-shock-absorber-piston-rod

Yamaha. (2013, January 29). KYB and Yamaha Motor to Establish a Joint Venture. Retrieved from Yamaha Motor Co., Ltd: https://global.yamaha-motor.com/news/2013/0129/joint-venture.html#

Yangyang, Y., Junhong, Z., Dan, W., Xiangde, M., & Ma, S. (2022). Effect of piston texture at inclination and eccentricity work conditions on damping characteristics of a hydraulic shock absorber. Tianjin University. Tianjin, China: Nature Portofolio. doi:10.1038/s41598-022-13721-0

Yisheng, B. (2006, August 23). Fixed capital stock depreciation in developing countries: Some evidence from firm level data. The Journal of Development Studies, 881-991. doi:doi.org/10.1080/00220380600742183

Young, W., & R.G., B. (2002). Roark's Formulas for Stress and Strain. McGraw-Hill, 234-455.

Yousif, B., Thaer, S., Sadok, S., Mohammed, H., & Jamil, R. (2021). Numerical study on the damping characteristics of a shock absorber valve utilizing different velocities through cfd analysis. 8th eccomas Thematic Conference on Computational Methods in Structural Dynamics and Earthquake Engineering (pp. 4355-4356). Athens, Greece: Eccomas Proceedia. doi:10.7712/120121.8791.18767

Zdzisław, H., Piotr, R., & Roman, G. (2021). The infuence of temperature on the damping characteristic of hydraulic shock Absorbers. Eksploatacja i Niezawodność – Maintenance and Reliability, 23(2), 346-351. doi:http://doi.org/10.17531/ein.2021.2.14.

Zhang, H. Y., Cheng, Z. G., & Han, B. H. (2021). Overview of suspension system dynamics analysis. Journal of Physics: Conference, 2-3. doi:10.1088/1742-6596/1777/1/012025

Zhifei, W., Guangzhao, X., Hongwei, Y., & Mingjie, L. (2021). Analysis of Damping Characteristics of a HydraulicShock Absorbe. Shock and Vibration, 2-10. doi:10.1155/2021/8883024

Zhiqiang, L., Chengjie, J., & Jie, W. (2023, August). Research on new shock absorber with variable piston volume for automotive. Journal of Advanced Mechanical Design Systems and Manufacturing , 15(5), 1-15. doi:10.1299/jamdsm.2023jamdsm0055

APPENDICES

Appendix A: Vehicle Specifications

A-1. Toyota Wish ZNE10R Specifications

Item \ Area				Singapore
Body Type				Station Wagon
Vehicle Grade				X
Model Code				ZNE10R-HPPNK
Major Dimensions & Vehicle Weights	Overall	Length	mm (in.)	4560 (179.5)
		Width	mm (in.)	1695 (66.7)
		Height	mm (in.)	1590 (62.6)
	Wheel Base		mm (in.)	2750 (108.3)
	Tread	Front	mm (in.)	1480 (58.3)
		Rear	mm (in.)	1465 (57.7)
	Room	Length	mm (in.)	2670 (105.1)
		Width	mm (in.)	1460 (57.5)
		Height	mm (in.)	1310 (51.8)
	Overhang	Front	mm (in.)	880 (34.6)
		Rear	mm (in.)	930 (36.6)
	Min. Running Ground Clearance		mm (in.)	155 (6.1)
	Angle of Approach		degrees	15.3°
	Angle of Departure		degrees	18.7°
	Curb Weight	Front	kg (lb)	760 (1675)
		Rear	kg (lb)	540 (1190)
		Total	kg (lb)	1300 (2866)
	Gross Vehicle Weight	Front	kg (lb)	870 (1918)
		Rear	kg (lb)	815 (1797)
		Total	kg (lb)	1685 (3715)
	Fuel Tank Capacity	ℓ	L (Imp. gal)	60 (13.2)
	Luggage Capacity (VDA)		m^3 (cu.ft.)	0.176 (6.22)
	Max. Speed		km/h	180
	Max. Cruising Speed		km/h	—
	Acceleration	0 to 100 km/h	sec.	—

DIMENSIONS

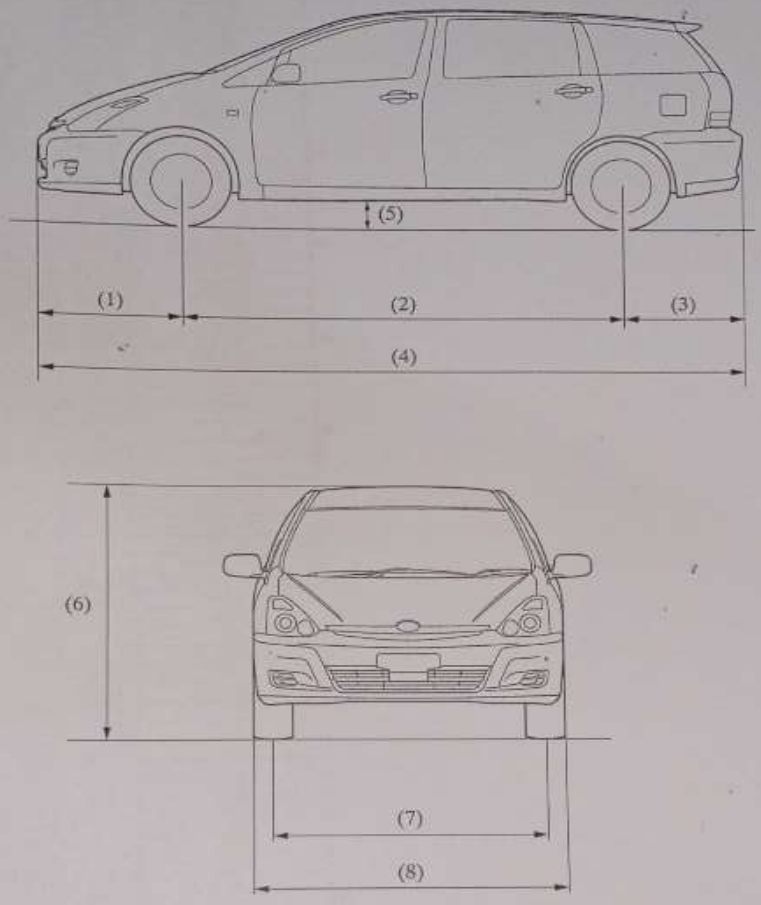

(1)	Front Overhang		mm (in.)	880 (34.6)
(2)	Wheel Base		mm (in.)	2750 (108.3)
(3)	Rear Overhang		mm (in.)	930 (36.6)
(4)	Overall Length		mm (in.)	4560 (179.5)
(5)	Minimum Running Ground Clearance		mm (in.)	155 (6.1)
(6)	Overall Height		mm (in.)	1590 (62.6)
(7)	Tread	Front	mm (in.)	1480 (58.3)
		Rear	mm (in.)	1465 (57.7)
(8)	Overall Width		mm (in.)	1695 (66.7)

A-2. Front Rear Weight Distribution at 1750Kg

Curb-Weight Axle Loads

$$\text{Front Axle: } 0.58 \times 1300 = 754\text{Kg}$$

$$\text{Rear axle: } 0.42 \times 1300 = 546\text{Kg}$$

Passenger Loads

$$\text{Total passenger mass: } 7 \times 65 = 455\text{kg}$$

Total Gross Mass

$$\text{Gross Weight } = 1300 + 455 = 1755 \text{ kg} (\approx 1750 \text{ kg target})$$

$$\text{Front: } 754 + 130 = 884\text{Kg}$$

$$\text{Rear: } 546 + 325 = 871\text{kg}$$

Reduction rate of front-axle percentage

$$\text{r} = \frac{\Delta\%}{\Delta\text{W}} = \frac{52\% - 58\%}{1686 - 1300} \approx -0.0155\%/\text{kg}$$

Front-axle percentage at 1750 kg

$$\Delta\text{W}_2 = 1750 - 1300 = 450\text{Kg}$$

$$\Delta\%_2 = \text{r}\Delta\text{W}_2 = (-0.0155\%/\text{kg}) \times 450\text{kg} = -6.975\%$$

$$\text{Front}\%_{1750} = 58\% + \Delta\%_2 \approx 58\% - 6.975\% = 51.025\%$$

$$\text{Rear}\%_{1750} = 100 - 51.025 = 48.975\%$$

Total front-axle sprung mass

$$\text{m}_{\text{front,sprung}} = 1750kg \times 0.85 \times 0.51025$$

Sprung mass per front wheel

$$= \frac{1750kg \times 0.85 \times 0.51025}{2} = 379.31kg$$

Unsprung Mass per Front Wheel

$$= \frac{1750kg \times 0.15 \times 0.51025}{2} = 66.98\text{kg}$$

Appendix B: Closed-Form (Algebraic) Derivation of the Spring-Deflection Gain

The goal is an explicit frequency-response function

$\mathrm{G(j\omega)} = x_r(\mathrm{j\omega})/z_r(\mathrm{j\omega})$ that links road input z_r to relative spring compression $x_r = x_u - x_s$.

All steps use classical Laplace/transfer-function techniques

B-1. Quarter-car equations in the Laplace domain

$$m_\mathrm{s}\mathrm{s}^2\mathrm{X_s(s)} + \mathrm{cs[X_s - X_u]} + \mathrm{k_s[X_s - X_u]} = 0$$

$$m_\mathrm{u}\mathrm{s}^2\mathrm{X_u(s)} + \mathrm{cs[X_u - X_s]} + \mathrm{k_s[X_u - X_s]} + \mathrm{k_t[X_u - z_r(s)]} = 0$$

B-2. Transfer function for spring deflection

Subtracting the two rows of (B-1) and collecting terms to obtain

$$G(s) = \frac{X_r(s)}{z_r(s)} = \frac{k_t(k_s + cs)}{(k_s + cs - m_s s^2)(k_t + k_s + cs - m_u s^2) - (k_s + cs)}$$

(This matches the literature form often derived with Mason's gain rule or Cramer's rule.)

B-3. Partition into real/imaginary parts at $\mathbf{s = j\omega}$

Define

$$k_s + cs \equiv A_3 +, k_s + cs - m_s s^2 \equiv A_1 + jB_1, k_t + k_s + cs - m_u s^2 \equiv A_2 + jB_2$$

Then the numerator and denominator magnitudes are

$$\lceil N \rceil = k_t\sqrt{A_3^2 + B_3^2}, \lceil D \rceil = k_t\sqrt{A_D^2 + B_D^2}$$

with

$$\mathrm{A_D} = \mathrm{A_1A_2} - \mathrm{B_1B_2} - (\mathrm{A_3^2} + \mathrm{B_3^2})$$

$$\mathrm{B_D} = \mathrm{A_1B_2} + \mathrm{A_2B_1} - 2A_3B_3$$

B-4. Gain magnitude

$$\lceil G(\omega) \rceil = \frac{\lceil N \rceil}{\lceil D \rceil} = \frac{k_t \sqrt{\mathrm{A}_3^2 + \mathrm{B}_3^2}}{\sqrt{A_D^2 + B_D^2}}$$

Substituting the design constants (m_s,m_u,k_s,k_t,c) and the dominant pothole frequency ω_r from Equation (3.3) gives

$$\lceil G(\omega) \rceil = 0.42$$

B-5. Peak spring compression from a single harmonic

For the half-sine pothole, the first-harmonic amplitude is

$$\mathrm{A}_1 = \frac{2\mathrm{d}}{\pi}$$

Peak Spring Deflection

$$\mathrm{X}_{\mathrm{amp}} = \lceil G(\omega) \rceil \mathrm{A}_1$$

B-6. Design Allowance and Final Stroke

Applying a 20 % design margin to cover higher harmonics and tolerance stack-ups,

$$\Delta x_{max} = 1.2 X_{amp} = 1.2 \lceil G(\omega) \rceil \mathrm{A}_1 = 0.0574 m (\approx 57 mm)$$

This 57 mm is the minimum compression travel that the coil spring, damper and bump-stop assembly must provide to clear the worst-case 0.18 m pothole without coil clash or bottom-out.

Appendix C: Shim Stack Valve -Numerical Derivations

This appendix reproduces every substitution that yields the values quoted in the Discussion of Results Section 4.3.7. Equation numbers refer to the methodology in Section 3.6.5.

Parameter	**Value**
Outer seat radius, r_o	0.018 m
Clamp radius, r_c	0.01345 m
Piston area, A	$1.616\times10^{2}\text{m}^2$
Oil density, ρ	850 kg m^{-3}
Discharge coefficient, C_d	0.65
Young's modulus, E	210 GPa
Poisson ratio, v	0.30
Proof strength, σ_y	420MPa
Stress factor, K_t	1.5
Bleed fraction at HS, ϕ	0.15

C-1. Bleed Hole Areas

Comfort-flow requirement (rebound),

$$\boldsymbol{Q_{LS} = v_{LS}A_e = 0.05(1.616 \times 10^{-3}) = 8.08 \times 10^{-5}\, m^3/s}$$

Pressure drop for 0.30 kN comfort force

$$\Delta P_{\{LS,\text{re}\}} = \frac{F_{\text{LS}}}{A_e} = \frac{0.3 \times 10^3}{1.616 \times 10^{-3}} = 0.186\, MPa$$

Total bleed area

$$A_{h,\text{re}} = \frac{Q_{LS}}{C_d\sqrt{2\Delta P_{LS,\text{re}}/\rho}} = 5.9\text{mm}^2$$

Two Ø2mm drillings supply,

$A_h = 4(\frac{\pi 2^2}{4}) = 6.3\text{mm}^2$ (+7 % overshoot, accepted).

The compression side repeats the same steps with $F_{LS,CO}$=0.15kN, giving 8.1mm²; three Ø2mm holes yield 9.4mm² (+16 %).

C-2. Plate Flexural Rigidities

Rigidity of a solid plate,

$$D_i = \frac{E t_i^3}{12(1 - v^2)}$$

Thickness t_i(mm)	**D_i (Nm)**	**$1/D_i$ ($N^{-1}m^{-1}$)**
0.35	0.83	1.204
0.30	0.52	1.928
0.25	0.30	3.333
0.15	0.065	15.385
Sum	—	21.85

Drilled outer leaf retains 0.987 ligament efficiency →$D_{i,eff}$=0.83×0.987=0.82Nm; the change is inside rounding error.

C- 3. Edge-Gap Prediction

Geometry factor

$$\frac{(r_o^4 - r_c^4)}{64} = \frac{0.018^4 - 0.01345^4}{64} = 1.13 \times 10^{-9} m^4$$

High-speed pressure (rebound)

$$\Delta P_{\{\mathrm{HS,re}\}} = \frac{F_{\mathrm{LS}}}{A_e} = \frac{3.10 \times 10^3}{1.616 \times 10^{-3}} = 1.92 MPa$$

Edge gap,

$$\mathcal{Y}(\Delta P) = \frac{\Delta P(r_o^4 - r_c^4)}{64} \sum_{i=1}^{4} \frac{1}{D_{i,eff}} = 1.92\mathrm{MPa}(1.13 \times 10^{-9}) \ 21.85$$

$$= 0.42\mathrm{mm}$$

The compression stack (thickness set 0.35/0.30/0.25/0.10 mm, $\sum 1/D_i$=19.24) gives y_{co}=0.20 mm.

C-4. Combined Flow at Impact Velocity

Per port flow

$$Q_P = v_{HS}A_e = 0.30(1.616 \times 10^{-3}) = 4.85 \times 10^{-4}\ m^3/s$$

$$Q_V = 0.85Q_P = 4.12 \times 10^{-4}\ m^3/s \text{ (bleed 15\% of Total)}$$

$$Q_{LS} = C_d A_h \sqrt{\frac{2\Delta P_{HS,re}}{\rho}} = 1.12 \times 10^{-4} m^3/s$$

Edge gap becomes

$$Q_{edge} = C_d(2\pi r_o \mathcal{Y}(\Delta P))\sqrt{\frac{2\Delta P_{HS,re}}{\rho}} = 3.70 \times 10^{-4} m^3/s$$

Total High-speed Flow

$$Q_{HS} = Q_{bleed} + Q_{edge} = 4.82 \times 10^{-4} m^{-4}/s$$

Within +1% of $v_{HS}A_e$

5. Peak Stresses

With t_{min}=0.15mm(rebound)

$$\sigma_{max} \approx \frac{3\Delta P_{HS} r_O^2}{2t_{min}^2}\ K_t = \frac{3(1.92 \times 10^6)(0.018^2)}{2(1.5 \times 10^{-4})^2}(1.5) = 310MPa$$

Compression Stack (t_{min}=0.10mm, $\Delta P_{HS,co}$=0.98MPa) gives 295MPa, Both stresses lie below $0.75\sigma_y$=315MPa

C-6. Summary

Quantity	Rebound	Compression
Net bleed area A_h	6.3mm²	9.4mm²
Edge gap y @ΔP_{HS}	0.42mm	0.20mm
Bleed flow @HS	1.12×10^{-4}m³/s	1.42×10^{-4} m³/s
Edge flow @HS	3.70×10^{-4}m³/s	2.70×10^{-4}m³/s
Total flow @HS	4.82×10^{-4}m³/s	4.12×10^{-4}m³/s
Peak pressure drop	1.93MPa	0.98MPa
Peak force	3.12kN	1.58kN
Peak stress	310MPa	295MPa
Safety margin vs σ_γ	26%	30%

All calculated quantities correspond exactly to the values cited in the main discussion, demonstrating internal consistency of the analytical chain.

Appendix D: Material Properties and Tables

D-1. Motorex Shock Absorber Oil 2.5W

Product Properties	
Colour	Red
Density at 20°C	0.881 g/cm^3 (ASTM D4052)
Viscosity at 40°C	14.5 mm^2/s (DIN 51562-1)
Viscosity at 100°C	4.5 mm^2/s (DIN 51562-1)
Viscosity Index	>250 (DIN ISO 2909)
Pour Point	<-40 °C (ASTM D5950)
Flash Point (C.O.C.)	120°C (DIN EN ISO 2592)

D-3. AISI 6150 Chromium Vanadium Alloy Steel properties

Chemical Composition

Element	Content (%)
Iron, Fe	97.095 - 97.72
Chromium, Cr	0.800 - 1.10
Manganese, Mn	0.7 - 0.9
Carbon, C	0.480 - 0.530
Silicon, Si	0.150 - 0.3
Vanadium, V	≥ 0.150
Sulfur, S	≤ 0.04
Phosphorous, P	≤ 0.0350

Physical properties

Properties	Metric	Imperial
Density	7.85 g/cm^3	0.284 lb/in^3

Mechanical Properties

Properties	Metric	Imperial
Tensile strength, ultimate	670 MPa	97200 psi
Tensile strength, yield	415 MPa	60200 psi
Izod impact	27 J	19.9 ft-lb
Modulus of elasticity	190-210 GPa	27557-30458 ksi
Shear modulus (typical for steel)	80 GPa	11600 ksi
Bulk modulus (typical for steel)	140 GPa	20300 ksi
Poissons ratio (calculated)	0.27 – 0.30	0.27-0.30
Elongation at break (in 50 mm)	23%	23%
Hardness, Brinell	197	197

Source: Azo Materials (https://www.azom.com/article.aspx?ArticleID=6744)

D-4. AISI1018 carbon steel

Property	*Value*
Ultimate tensile strength	350 MPa
Yield strength	276 MPa
Elongation	17%
Rockwell hardness	B60
Bulk modulus	140 GPa
Poisson's ratio	0.33
Shear modulus	26 GPa
Machinability	50%

(Nagaraj, 2015)

Appendix E: Damper Solid Works Drawings

E-1: Shims

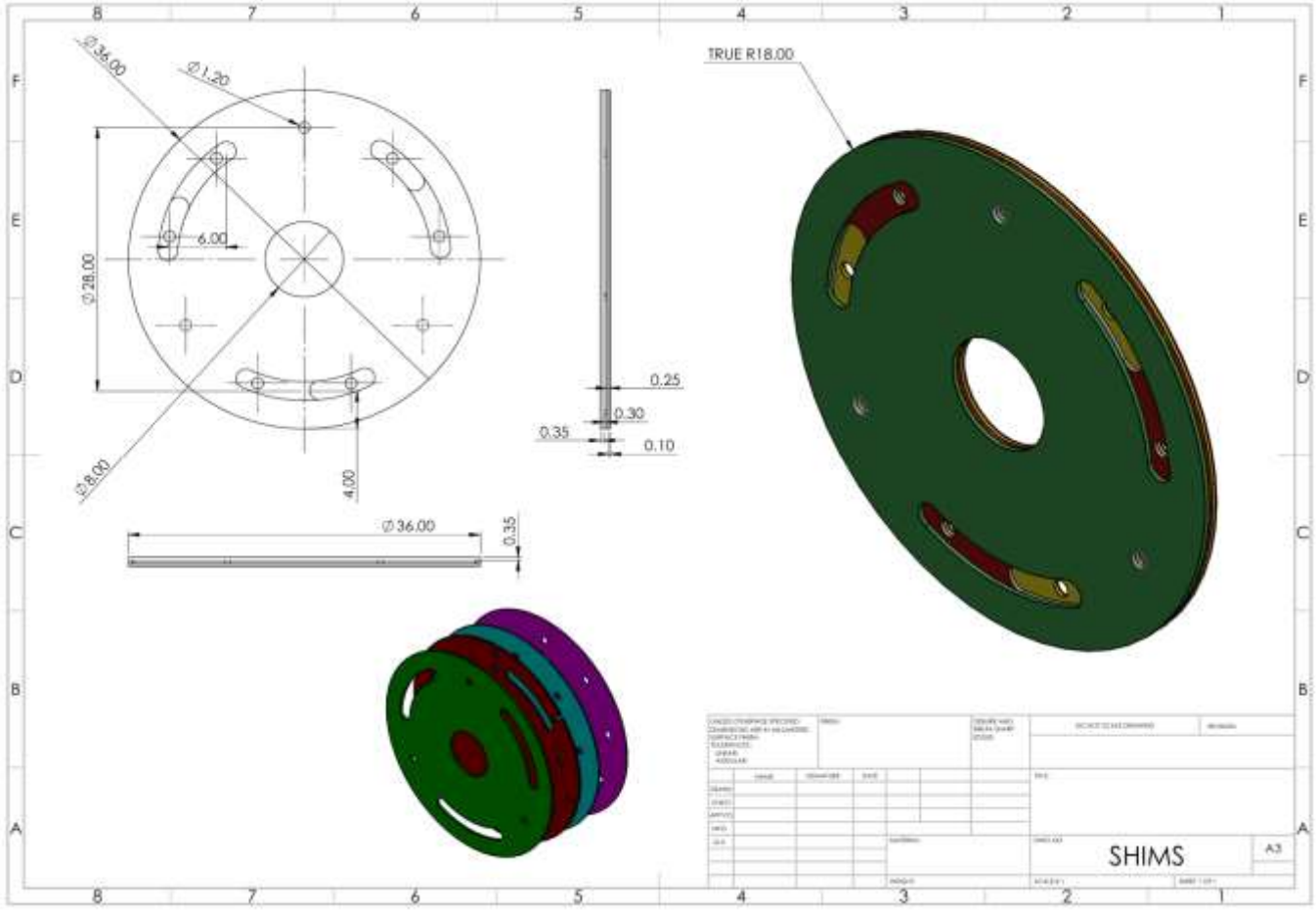

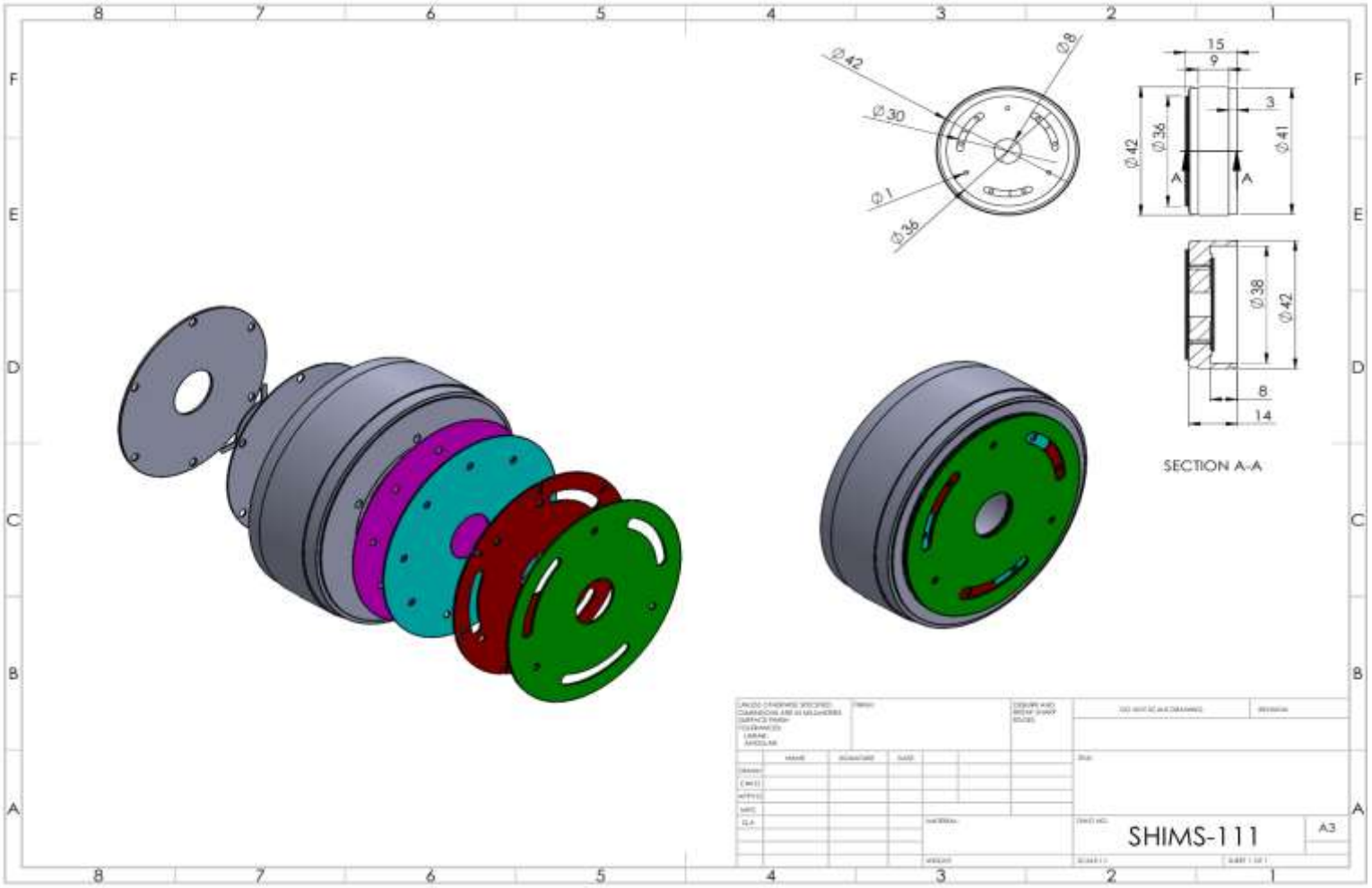

E-2: Shims and Pistons Assembly

Appendix F: Solid works Plot Data

Total Pressure [Pa]		Total Pressure [Pa]		Force (X) [N]	
Iterations [ ]	REBOUND SHIMS	Iterations [ ]	COMPRESSION SHIMS	Iterations [ ]	MOVING PISTON
	Yes		Yes		Yes
	0		0		0
	8718554.595		7012619.827		3825.760343
	0		0		0
	3456653.681		2593681.366		-2503.721073
	3157202.299		2441547.176		-5534.852001
	12065058.23		9553253.552		-1617.359537
1	12065058.23	1	9553253.552	1	-5534.852001
2	7571493.265	2	5952425.707	2	-4131.701405
3	8080868.22	3	6370628.429	3	-3885.507803
4	4224817.578	4	3395818.349	4	-2158.200883
5	3676843.004	5	2923279.614	5	-1787.64112
6	3480230.601	6	2788316.211	6	-1673.657632
7	3664206.171	7	2919178.247	7	-1761.266505
8	3646634.528	8	2920839.309	8	-1755.212094
9	3661322.809	9	2918399.792	9	-1762.284576
10	3617631.897	10	2900404.984	10	-1746.210955
11	3660738.076	11	2916672.784	11	-1760.320295
12	3577360.147	12	2868177.587	12	-1740.062334
13	3648771.216	13	2904895.341	13	-1750.301959
14	3493589.426	14	2802028.422	14	-1704.895426
15	3603297.519	15	2867880.617	15	-1727.255984
16	3453805.518	16	2770268.327	16	-1686.920444
17	3549340.841	17	2824739.915	17	-1698.562216
18	3351649.084	18	2691318.507	18	-1653.090343
19	3550685.615	19	2820148.835	19	-1676.884029
20	3267147.272	20	2628639.426	20	-1634.241894

21	3540157.263	21	2809684.319	21	-1665.212914
22	3222370.449	22	2593532.757	22	-1626.245681
23	3541751.04	23	2805599.202	23	-1649.581447
24	3186302.491	24	2564603.898	24	-1619.635192
25	3509639.677	25	2782234.858	25	-1642.732698
26	3208716.568	26	2574533.207	26	-1617.359537
27	3440058.73	27	2729138.952	27	-1627.415097
28	3224895.776	28	2580807.988	28	-1620.675217
29	3388956.471	29	2690410.756	29	-1628.258677
30	3212983.421	30	2567418.361	30	-1628.972802
31	3366216.308	31	2670663.201	31	-1636.799041
32	3157202.299	32	2521391.417	32	-1640.340757
33	3398674.483	33	2689824.298	33	-1655.425123
34	3187368.007	34	2537901.965	34	-1659.104626
35	3418687.443	35	2698349.978	35	-1679.529049
36	3192233.355	36	2534584.818	36	-1685.45057
37	3394322.206	37	2673962.291	37	-1712.197688
38	3207181.717	38	2535533.665	38	-1725.137535
39	3375206.077	39	2650371.331	39	-1755.137782
40	3231550.204	40	2541287.068	40	-1773.998569
41	3360174.255	41	2627571.704	41	-1807.60017
42	3247046.919	42	2538434.491	42	-1832.424818
43	3363534.882	43	2614388.138	43	-1869.82924
44	3248794.85	44	2522422.829	44	-1899.757378
45	3369780.767	45	2601278.729	45	-1939.733468
46	3254846.256	46	2507050.361	46	-1975.180154
47	3370445.385	47	2581735.077	47	-2018.505536
48	3263354.175	48	2491548.473	48	-2057.267158
49	3373334.458	49	2561389.227	49	-2102.56814
50	3272849.002	50	2477439.747	50	-2138.367446
51	3379594.449	51	2546012.61	51	-2181.771578
52	3285254.047	52	2463751.23	52	-2224.351412

53	3385966.685	53	2528361.905	53	-2265.569298
54	3300017.922	54	2452994.894	54	-2304.788884
55	3397334.9	55	2515450.798	55	-2344.212921
56	3316109.676	56	2445511.124	56	-2382.317163
57	3409706.718	57	2507295.965	57	-2419.889252
58	3331621.379	58	2441547.176	58	-2455.924874
59	3427984.16	59	2507525.47	59	-2488.814332
60	3350059.642	60	2443875.958	60	-2519.302166
61	3444725.944	61	2510594.112	61	-2547.350071
62	3370875.503	62	2454046.631	62	-2571.847086
63	3464906.526	63	2528707.499	63	-2595.893408
64	3396312.814	64	2479004.25	64	-2616.373045
65	3484090.335	65	2546111.797	65	-2636.014152
66	3419552.254	66	2494690.146	66	-2650.196251
67	3504994.522	67	2551516.94	67	-2666.959572
68	3440754.917	68	2498783.804	68	-2677.58151
69	3522422.305	69	2555850.22	69	-2690.747271
70	3458114.436	70	2507074.737	70	-2698.543496
71	3537178.807	71	2564964.73	71	-2707.910662
72	3472439.116	72	2517340.354	72	-2714.838001
73	3548760.959	73	2575636.91	73	-2721.763026
74	3485771.828	74	2535365.741	74	-2725.638207
75	3559055.826	75	2596125.822	75	-2733.304119
76	3495316.898	76	2554727.613	76	-2737.886908
77	3565531.049	77	2613531.772	77	-2744.137585
78	3503625.655	78	2572329.14	78	-2743.624256
79	3569030.83	79	2627254.97	79	-2749.212671
80	3506170.876	80	2588599.742	80	-2749.826668
81	3575467.506	81	2649908.565	81	-2756.459529
82	3522105.701	82	2615256.108	82	-2756.016937
83	3569974.289	83	2659839.279	83	-2762.737194
84	3519472.728	84	2628027.72	84	-2762.334942

85	3575013.071	85	2678206.892	85	-2767.153556
86	3526357.268	86	2646233.424	86	-2766.957692
87	3571763.174	87	2689382.943	87	-2772.235425
88	3519173.414	88	2653708.1	88	-2771.016302
89	3570324.06	89	2701176.438	89	-2775.831423
90	3527285.325	90	2672311.4	90	-2776.308028
91	3559757.108	91	2706404.55	91	-2779.607198
92	3518122.782	92	2680801.398	92	-2778.892299
93	3556775.947	93	2718225.399	93	-2782.486428
94	3524424.256	94	2700684.912	94	-2781.2458
95	3545845.525	95	2727478.413	95	-2786.592873
96	3518685.885	96	2711845.915	96	-2784.683871
97	3541413.332	97	2740670.352	97	-2788.641732
98	3518447.434	98	2726890.801	98	-2787.68717
99	3530591.525	99	2748008.205	99	-2791.781513
100	3510457.769	100	2738702.869	100	-2789.051443

Temperature (Fluid) [K]

Physical time [s]	FLUID TEMPERATURES
	Yes
	0
	0.01021
	0
	293.1696
	293.1592
	293.1799
4.19387E-07	293.1798
4.38904E-07	293.1799
4.59407E-07	293.1793
4.80793E-07	293.1793
5.03352E-07	293.1791

Velocity [m/s]

Physical time [s]	CYCLINDER FLUID VELOCITIES
	Yes
	0
	0.152287
	0
	1.497817
	1.345531
	1.678107
4.19387E-07	1.345531
4.38904E-07	1.354742
4.59407E-07	1.36488
4.80793E-07	1.35992
5.03352E-07	1.360152

5.40026E-07	293.1787	5.40026E-07	1.364215
5.8072E-07	293.1783	5.8072E-07	1.371502
6.2508E-07	293.1778	6.2508E-07	1.378676
6.72721E-07	293.1773	6.72721E-07	1.390304
7.23452E-07	293.1767	7.23452E-07	1.394446
7.9736E-07	293.1759	7.9736E-07	1.408853
8.84384E-07	293.1749	8.84384E-07	1.416232
9.74971E-07	293.1739	9.74971E-07	1.430164
1.06237E-06	293.173	1.06237E-06	1.435739
1.14852E-06	293.1721	1.14852E-06	1.453033
1.23269E-06	293.1712	1.23269E-06	1.458238
1.31628E-06	293.1704	1.31628E-06	1.474022
1.39837E-06	293.1696	1.39837E-06	1.478666
1.48129E-06	293.169	1.48129E-06	1.494079
1.56947E-06	293.1682	1.56947E-06	1.501606
1.75649E-06	293.1667	1.75649E-06	1.53515
1.89059E-06	293.1656	1.89059E-06	1.545136
2.07008E-06	293.1642	2.07008E-06	1.574469
2.18513E-06	293.1633	2.18513E-06	1.581878
2.49889E-06	293.1612	2.49889E-06	1.639857
2.80819E-06	293.1592	2.80819E-06	1.678107